

Study and exploration on inorganic nanomaterials as additive in lubricant application

by

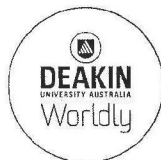
Deepika

M.Sc.

Submitted in fulfillment of the requirements for the degree of
Doctor of Philosophy

Deakin University

August, 2014



**DEAKIN UNIVERSITY
ACCESS TO THESIS - A**

I am the author of the thesis entitled:

**STUDY AND EXPLORATION ON INORGANIC NANOMATERIALS AS ADDITIVE IN
LUBRICANT APPLICATION**

Submitted for the degree of: **Doctor of Philosophy**

This thesis may be made available for consultation, loan and limited copying in
accordance with the Copyright Act 1968.

*'I certify that I am the student named below and that the information provided in the form is
correct'*

Full Name: Deepika

Signed: Signature Redacted by Library

Date: 19th Nov 2014



**DEAKIN UNIVERSITY
CANDIDATE DECLARATION**

I certify the following about the thesis entitled (10 word maximum)

Study and exploration on inorganic nano-
materials as additive in lubricant application.

submitted for the degree of Doctor of Philosophy.

- a. I am the creator of all or part of the whole work(s) (including content and layout) and that where reference is made to the work of others, due acknowledgment is given.
- b. The work(s) are not in any way a violation or infringement of any copyright, trademark, patent, or other rights whatsoever of any person.
- c. That if the work(s) have been commissioned, sponsored or supported by any organisation, I have fulfilled all of the obligations required by such contract or agreement.

I also certify that any material in the thesis which has been accepted for a degree or diploma by any university or institution is identified in the text.

"I certify that I am the student named below and that the information provided in the form is correct"

Full Name: Deepika
(Please Print)

Signed: Signature Redacted by Library

Date: 27th August 2014

Acknowledgements

It is with a great deal of pleasure that I thank those who have contributed in so many ways to the completion of this dissertation. First, with my deep sense of affectionate appreciation and admiration, I want to thank to my supervisors, Dr. Samik Kumar Hait and Professor Ying Ian Chen who continue to put up with their constant encouragement, kind support, invaluable guidance, and for many other reasons.

I would like to thank to Dr. Jyotiranjana Ota, Dr. M. Vijayraj, Dr. Om Prakash and Dr. M.K Vyas for their generous support and invaluable advice during my doctoral course. I also wish to convey my sincere thanks to Dr. Rashmi Bagai and Dr. J. Christopher for their invaluable help and advice on the transmission electron microscopy and thermogravimetric analysis during entire periods of my research. Special thanks have to go to Ms. Nitu Singh for her help in the examination of x-ray diffraction data for coated CaCO₃ nanoparticles.

Department of tribology is thanked extremely for helping me in carrying out tribological studies; grateful acknowledgement is made to all my friends at Indian Oil R&D centre who made my research so intellectually stimulating and enjoyable.

Special thanks are given to Dr. M.B Patel, due to his constant supports in every aspect. My hearties thanks for Dr. S.S.V Ramakumar and Dr. M.I.S Sastry for their support, timely advice and backup during my research.

I particularly want to thank the financial support of Indian oil R&D centre in the form of Indian Oil Golden Jubilee Fellowship to carry out this research work and Deakin University for supporting my research work under Deakin University Doctoral Program.

My special thanks to Dr. Luhua Li for his timely support, help and encouragement during my visit to Australia. And I also thanked my lab mates Thrinath, Tan, Si Qin, Olga, Mahedi Hassan and all for their help, back up and boosting my spirit.

I am also thankful to Prof. Peter Hodgson for giving me the opportunity to come to Australia and work.

Last, but not least my gratitude goes to the ones that stood by me even though I have at times been absent in both mind and body, Mom, Dad, Manmeet, Sarita, my sisters and my loving brother. You brought me through a time where I have been everything from enthusiastic, challenged, stressed and depressed of my work. Sometimes I have even felt lonely during this time, but as the Tibetan' saying goes: *"Don't be afraid to encounter loneliness. It is a rare opportunity to make friends with oneself."*

"All research is useless, unless it is allied with internal research" ...Gandhi

I would like to dedicate this thesis to **my Mother and Father.**

DEEPIKA

List of publications

1. Results presented in Chapter 3 have been published in the article:
 - Deepika, S.K Hait, J. Christopher, Y.Chen, P. Hodgson, D.K Tuli, “Preparation & evaluation of hydrophobically modified core shell calcium carbonate structure by different capping agents”, **Powder Technology**, 235 (2013) 581.
2. Results presented in Chapter 4 have been published in the article:
 - Deepika, S.K Hait, Y.Chen, “Optimization of milling parameters on the synthesis of stearic acid coated CaCO_3 nanoparticles”, **Journal of coating technology and research**, 11 (2014) 273.
3. Results presented in Chapter 5 have been accepted in the article:
 - Deepika, S.K Hait, Y.Chen, “Study on the influence of Li-Grease EP & AW performance by exfoliated MoS_2 nanosheet additive”, **Advanced Science letters**.
4. Results presented in Chapter 6 have been submitted to Scientific Reports as a conference proceeding in the article:
 - Deepika, Lu Hua Li, Alexey M. Glushenkov, Samik. K. Hait, Peter Hodgson and Ying Chen, “High-Efficient Production of Boron Nitride Nanosheets via an Optimized Ball Milling Process for Lubrication in Oil”.

Conferences

1. Poster at 2nd DIRI Symposium “Frontiers in Science”, November 2011, Delhi, India.
2. Poster at “Advances in Functional Nanomaterials” November 2012, UNSW, Sydney, Australia.
3. Attended Institute for Frontier Materials (IFM) conference, November 2012 conducted by Deakin University, Waurn Ponds, Australia.
4. Oral “5th Asian Conference on Colloid and Interface Science “ACCIS November 2013, Darjeeling, India.
5. Oral and poster presentation “National conference on Nanotechnology and renewable energy” April 2014, JMI University, New Delhi, India.

Abbreviations

AW	Anti-wear
AFM	Atomic force microscopy
BN	Boron nitride
BNNSs	Boron nitride nanosheets
Ca-OA	Calcium oleate
CTAB	Cetyltrimethyl ammonium bromide
CC	Commercial colloidal
CoF	Coefficient of friction
CVD	Chemical vapor deposition
[C12mim]Br	1-dodecyl-3-methylimidazolium bromide
DA	Dodecanoic acid
DDAB	Didodecyl dimethyl ammonium bromide
DSC	Differential scanning calorimeter
DLS	Dynamic laser scattering
EP	Extreme pressure
FAS-17	Heptadecafluorodecyl-trimethoxysilane
FTIR	Fourier transformation infrared
HRTEM	High resolution transmission electron microscope
HFCVD	Hot filament-chemical vapour deposition
IF	Inorganic fullerenes
k_{eff}	Effective thermal conductivities
LP	Liquid paraffin
MSA	Methanesulfonic acid
ML	Minimum quantity lubrication
MS	Microspheres
NH	Nano-hollow
NPCC	Nano precipitated calcium carbonate
Na-OA	Sodium oleate
Na-SA	Sodium stearate
NMP	N-Methyl pyrrolidone

NFs	Nanofluids
OA	Oleic acid
ODP	Octadecyl hydrogen phosphate
PCC	Precipitated calcium carbonate
PGP	Polyethylene glycol phosphate
PAO	Poly alpha olefin
SA	Stearic acid
SO	Sodium oleate
SBR	Styrene-butadiene rubber
SEM	Scanning electron microscope
SAXS	Small angle x-ray scattering
TOA	Trioctylamine
TOP	Trioctylphosphine
TBN	Total base number
TGA	Thermo gravimetric analysis
WSD	Wear scar diameter
XRD	X-ray diffraction
XPS	X-ray photoelectron spectroscopy
ZDDP	Zinc dialkyl dithiophosphate

Abstract

This thesis work incorporates various facets of inorganic nanoparticles that have the potential to be utilized in the oil and petroleum industries. It includes their synthesis, characterization and utilization in lubricating oils and greases.

Chapter 1 includes an abbreviated and general background of inorganic nanoparticles, including calcium carbonate, molybdenum disulphide, hexagonal-boron nitride and their application in oil industries.

Chapter 2 lists experimental techniques that involve synthesis and characterization throughout the PhD work. Synthesis of nano or near nanoparticles was carried out using planetary ball mill, while the characterization of the obtained products was conducted using analytical tools including particle size analyzer, x-ray diffraction, transmission electron microscopy, scanning electron microscopy, thermo gravimetric analysis, small angle x-ray scattering, contact angle measurement, raman, BET and tribological tools (Falex four ball wear test machine, Seta-Shell 4 ball lubricant tester and Optimol SRV).

Chapter 3 describes the preparation procedure and evaluation of a hydrophobically modified core-shell calcium carbonate structure by different capping agents. The structure and surface morphology of the particles were characterized by transmission electron microscopy. The shell thickness was calculated from the results of transmission electron microscopy and thermo gravimetric analysis. The maximum coating thickness was found for octadodecanyl succinic anhydride.

Chapter 4 presents the core shell calcium carbonate structure modified by stearic acid. Contact angle measurement technique was used to analyze the hydrophobic character of synthesized particles. The shell thickness was determined using small angle x-ray scattering. The maximum thickness of shell was found to be 4.7nm, which corresponds to the molecular length of stearic acid.

Chapter 5 describes the production of surface modified molybdenum disulphide nanosheets using lecithin (a source of phosphorus (exfoliating / stabilizing agent)) along with antiwear additives and their tribological behaviour in terms of wear scar diameter; weld load and coefficient of friction was evaluated. Scanning electron microscopy and electron diffraction spectra analyses of the wear track were performed, along with raman spectroscopy. The results

showed the characteristic peaks of molybdenum disulphide over the surface of steel ball after four-ball test.

Chapter 6 involves the production of hexagonal-boron nitride nanosheets via low energy ball milling treatment for tribological application. Transmission electron microscopy analysis indicates that sheets obtained were highly ordered and crystalline in nature. Tribology of hexagonal-boron nitride nanosheets blended with base oil was also explored and found to give substantial improvement in lubrication.

Major conclusions and future work are summarized in **Chapter 7**.

TABLE OF CONTENTS

Acknowledgements	3
List of publications	5
Abbreviations	6
Abstract	8
List of figures	13
List of tables	17
1. Introduction	18
1.1. Brief overview	18
1.1.1. Nanotechnology and nanomaterials	18
1.1.1.1. Classification of nanoparticles	19
1.1.1.2. Importance of inorganic nanoparticles	19
1.2. Thesis objective	19
1.3. Review of related literature	20
1.3.1. Calcium carbonate	20
1.3.1.1. Significance of surface modifications	21
1.3.1.2. Core shell nanoparticles	22
1.3.1.3. Synthesis of hydrophobic CaCO ₃ nanoparticles	23
1.3.1.3.1. Methodology	23
1.3.1.3.1.1. Solution route	23
1.3.1.3.1.2. Carbonation route	25
1.3.1.3.1.2.1. Oleic acid based coatings	25
1.3.1.3.1.2.2. Stearic acid based coatings	25
1.3.1.3.1.2.3. Terpineol based coating	28
1.3.1.3.1.2.4. Dodecanoic acid and octadecyl hydrogen phosphate based coatings.	29
1.3.1.3.1.3. Milling	32
1.3.1.4. Tribological applications of CaCO ₃	35
1.3.2. Molybdenum disulfide	37
1.3.2.1. Tribological applications of MoS ₂	41

1.3.3.	Boron nitride	44
1.3.3.1.	Synthesis of h-BN	46
1.3.3.2.	Applications of h-BN	53
1.3.3.3.	Tribological applications of h-BN	53
2.	Experimental method and characterization techniques	57
2.1.	Experimental method	57
2.1.1.	Ball milling	57
2.2.	Characterization techniques	59
2.2.1.	Particle size analysis	59
2.2.2.	X-ray diffraction	60
2.2.3.	Electron microscopy	61
2.2.3.1.	Transmission electron microscopy	62
2.2.3.2.	Scanning electron microscope	63
2.2.4.	Thermo gravimetric analysis	65
2.2.5.	Small angle x-ray scattering	66
2.2.6.	Contact angle measurement	67
2.2.7.	Raman spectroscopy	68
2.2.8.	Surface area determination by BET method	69
2.2.9.	Tribological evaluation	70
3.	Wet milling of calcium carbonate with different capping agents to produce hydrophobic core shell nanostructure	73
3.1.	Introduction	73
3.2.	Experimental work	74
3.3.	Effect of milling on CaCO ₃ with different dispersants	76
3.4.	Coating thickness and surface density	81
3.5.	Coating effect and surface area	85
3.6.	Conclusions	86
4.	Ball milling of selected dispersant (stearic acid) for optimization of milling parameters	88
4.1.	Introduction	88
4.2.	Experimental work	90
4.3.	Effect of milling parameters	91
4.4.	Morphology of particles	97

4.5.	Analysis of modified surface	100
4.6.	Conclusions	101
5.	Tribological behaviour of surface modified exfoliated MoS₂ nanosheets	103
5.1.	Introduction	103
5.2.	Experimental work	104
5.3.	Grease preparation	106
5.4.	Characterization and tribological testing of prepared samples	107
5.5.	Conclusions	118
6.	High-efficient production of boron nitride nanosheets via an optimized ball milling process and their tribological studies	120
6.1.	Introduction	120
6.2.	Experimental work	120
6.3.	Effect of milling on h-BNNS production	121
6.4.	Tribology studies	125
6.5.	Conclusions	127
7.	Conclusions and future work	128
8.	References	131

List of figures

Figure 1.1	Schematic illustration for interaction between the organic substrate and CaCO_3 in aqueous medium.	21
Figure 1.2	Core shell nanoparticles.	22
Figure 1.3	Sketch 1 showing the map of different morphology of CaCO_3 crystals prepared in different micelle with different concentration: flower-shaped CaCO_3 crystals formed in the presence of (a) 12.5, (b) 15.0, (c) 25.0 mmol/L DTAB (dodecyltrimethylammonium bromide) and string-shaped CaCO_3 crystals, formed in the presence of (d) 60.0 mmol/L [C12mim] Br. Sketch 2 map of the growth procedure of calcium carbonate crystals with different morphology prepared by different concentration of DDAB: irregular globosity-shaped and irregular globosity-shaped crystals formed in the presence of (a) 7.5, (b) 10.0 mmol/L DDAB.	24
Figure 1.4	The experimental set-up for preparing CaCO_3 nanoparticles.	27
Figure 1.5	TEM images of (a) uncoated NPCC, (b) NPCC coated in aqueous, (c) NPCC coated with dry ball milling and (d) NPCC coated with ultrasonication.	28
Figure 1.6	Core shell structure of ns-PPC.	30
Figure 1.7	Schematic picture of an over based sulphonate detergent particle.	36
Figure 1.8	(a) SEM image of the as-synthesized MoS_2 nanotubes and (b) HRTEM of the as-synthesized MoS_2 nanotubes.	40
Figure 1.9	Possible tribochemical mechanism of IF- MoS_2 nanoparticles on steel surfaces.	42
Figure 1.10	X-ray photoelectron spectroscopy spectra of typical elements on the worn surfaces lubricated with (a) 0.50% CC- MoS_2 /oil and (b) 0.50% MS- MoS_2 /oil at 200 N.	43
Figure 1.11	Stribeck curves of steel balls lubricated by liquid paraffin and MoS_2 particles in point-contact friction.	44
Figure 1.12	SEM images of the BNNSs grown at different RH_2/RBF_3 (sccm): (a) 10/5, (b) 25/5, (c) 40/5, (d) 10/3, (e) 60/3, (f) 160/3, (g) 30/2, (h) 40/2 and (i) 100/2.	50
Figure 1.13	Schematic illustration of the protonation of BNNS in MSA solution (top),	51

and dispersion of BNNS in MSA in a sealed bottle (left) and exposed to air (right) two weeks after preparation.

Figure 2.1	Movements of working parts and balls in a planetary mill.	58
Figure 2.2	Schematic of contact angle measurement.	67
Figure 2.3	Spectrum of photon transition from elemental ground level to virtual states.	68
Figure 2.4	Photograph of (a) The Falex four ball wear test machine and (b) Seta-Shell 4 ball lubricant tester.	71
Figure 2.5	Photograph of Optimol SRV.	72
Figure 3.1	Detailed molecular structures of the dispersants used.	74
Figure 3.2	XRD patterns of CaCO_3 particles after milling in different capping agents (a) uncoated CaCO_3 , (b) OACHex, (c) SACHex, (d) PACHex, (e) SCCmet, (f) OLCmet, (g) ODCmet, (h) TPCmet and (i) DDCxyl.	76
Figure 3.3	Low-angle XRD patterns for (a) OACHex, (b) SACHex.	77
Figure 3.4	(i) Showing the thermal decomposition pattern for the (a) uncoated CaCO_3 and (b) stearic acid; (ii) showing the decomposition pattern for coated CaCO_3 with different capping agents (a) OACHex, (b) SACHex, (c) PACHex; (iii) (a) SCCmet, (b) OLCmet; (iv) (a) ODCmet, (b) TPCmet, (c) DDCxyl.	78
Figure 3.5	The TEM images of CaCO_3 particles : (a) uncoated CaCO_3 , (b) OACHex, (c) SACHex, (d) PACHex, (e) SCCmet, (f) OLCmet, (g) ODCmet, (h) TPCmet and (i) DDCxyl.	81
Figure 3.6	Representation of cubic core-shell CaCO_3 nanoparticle.	82
Figure 3.7	Showing the histogram plots for (a) OACHex, (b) SACHex, (c) PACHex, (d) SCCmet, (e) OLCmet, (f) ODCmet, (g) TPCmet, (h) DDCxyl.	83
Figure 3.8	Showing the TEM images (a) OACHex, (b) OACHex after 10 sec of beam exposure and (c) OACHex after 30 sec of beam exposure.	85
Figure 4.1	XRD pattern for (a) unmilled sample, (b) SC112hex, (c) SC114hex, (d) SC116hex, (e) pure calcium stearate and (f) SA.	92
Figure 4.2	XRD pattern showing the effect of different doses of SA w.r.t CaCO_3 for SA modified CaCO_3 (a) SC116hex and (b) SC216hex.	93
Figure 4.3	XRD pattern showing the effect of different ball ratio for SA modified CaCO_3 (a) SC216hex, (b) SC226hex and (c) SC246hex.	94

Figure 4.4	Raman pattern. (Note spectrum intensity of CaCO_3 was reduced to one eighth to match with the intensity of other spectra).	95
Figure 4.5	TGA curves of (a) unmodified CaCO_3 , (b) SA and (c) SA modified CaCO_3 (SC116hex) from room temperature to 900°C at heating rate of 10 deg/min in air medium.	96
Figure 4.6	TEM image of uncoated CaCO_3 particles.	98
Figure 4.7	TEM images of SA coated CaCO_3 particles (a) SC112hex, (b) SC114hex, (c) SC116hex, (d) SC216hex, (e) SC226hex and (f) SC246hex.	99
Figure 4.8	Contact angle measurement of CaCO_3 in (a) absence of organic additive and (b) presence of SA.	100
Figure 4.9	Small and wide angle x-ray scattering (Imaging Plate); red curve SC226hex and blue curve SC246hex.	101
Figure 5.1	TEM images of MoS_2 dispersions containing exfoliated sheets prepared through milling (a) 12LZM, (b) 21LZM, (c) 12LVM, (d) 21LVM and (e) SAED pattern matching with the hexagonal structure of MoS_2 .	107
Figure 5.2	XRD plots of (a) 2H- MoS_2 , (b) Molybdenum oxide, (c) 12LZM, (d) 21LZM, (e) 12LVM and (f) 21LVM.	108
Figure 5.3	Raman spectra of (a) standard MoS_2 , prepared dispersions (b) 12LZM, (c) 21LZM (d) 12LVM and (e) 21LVM.	108
Figure 5.4	Volumetric distribution for various dispersions.	109
Figure 5.5	EP data for the various samples blended with Lithium grease.	110
Figure 5.6	Wear data for the various samples blended with Lithium grease.	111
Figure 5.7	Wear and weld load trend of the grease samples that with varying concentration of ZDDP.	112
Figure 5.8	Wear and weld load trend of the grease samples that with varying concentration of MBDDC.	113
Figure 5.9	Coefficient of friction for Sample (Li grease + 12LZM) at different loads at constant temperature.	114
Figure 5.10	SEM images of the wear scar surface on the stationary steel balls tested with (a1) base Lithium grease, (b1) Li grease+12LZM and (c1) Li grease+21LZM. Figure 8(a2, b2, c2) displays the corresponding EDS pattern taken from the	115

respective wear surfaces.

Figure 5.11	Raman spectra of standard molybdenum compounds and worn surfaces in balls after four balls test.	117
Figure 6.1	SEM images of (a) starting h-BN particles, (b, c) partially exfoliated h-BN particles after 2h milling, (d) more exfoliated particles after 5h milling, (e) completely exfoliated particles after 10h milling and (f) normalized XRD spectra of the initial h-BN particles and the sheets ball milled for different periods of time without centrifugation.	121
Figure 6.2	SEM images for sample ball milled with different ball / powder ratio (a) 20:1, (b) 50:1 and (c) normalized XRD spectra of the initial h-BN particles and the sheets ball milled with different ball / powder ratio without centrifugation.	122
Figure 6.3:	SEM images for sample ball milled with different milling speed (a) 600 rpm, (b) normalized XRD spectra of the initial h-BN particles and the sheets ball milled with different milling speed without centrifugation.	123
Figure 6.4	SEM images of sample ball milled with different ball sizes (a) 0.6-0.8 mm (b) 0.1-0.2 mm, (c) higher magnification of selected area (indicated as box) from image “a” and (d) normalized XRD spectra of the initial h-BN particles and the sheets ball milled with different ball sizes without centrifugation.	124
Figure 6.5	(a) TEM Images of BN sheets, (b) the corresponding SAED pattern, (c) and (d) high-magnification TEM images, (e) and (f) TEM images of a monolayer and a bilayer BNNS and (g) EELS spectra of the BNNS.	125
Figure 6.6	Coefficient of friction for Sample (base oil, base oil-BN nanosheets) at fixed load and constant temperature.	126
Figure 6.7	SEM images of worn-surfaces of the stationary balls tested for sample (a) neat base oil and (b) base oil with h-BN nanosheets.	126

List of tables

Table 3.1	Details of the milling process parameters.	75
Table 3.2	Description of samples.	75
Table 3.3	Crystallite sizes of CaCO_3 milled with different capping agents.	77
Table 3.4	Weight loss during the temperature range of 250°C - 450°C corresponding to decomposition of calcium salt of capping agent for different capping agents.	79
Table 3.5	Shell thickness and surface density calculated using above calculations with the help of TEM and TGA results.	84
Table 3.6	Surface area for various milled samples compared with thickness of coating.	86
Table 4.1	Sieve sizes used for separating the balls from sample.	90
Table 4.2	Description of samples.	91
Table 4.3	Crystallite size (\AA) and particle size (nm) for sample ball milled for different time intervals.	92
Table 4.4	Crystallite size (\AA) and particle size (nm) for samples ball milled with different sample doses.	94
Table 4.5	Crystallite size (\AA) and particle size (nm) for samples ball milled for with different ball ratios.	95
Table 5.1	Sieve sizes used for separating the balls from sample.	105
Table 5.2	Milling parameters.	105
Table 5.3	Samples description.	105
Table 5.4	Effective concentration of MoS_2 and dispersants present in grease sample.	106
Table 5.5	Particle size for various ball milled samples.	109
Table 5.6	EDS analysis for different sample after four-ball test.	116

1. Introduction

1.1 Brief overview

1.1.1 Nanotechnology and nanoparticles

The exciting prospect of nanotechnology has potential use in almost every domain of life. Synthesis and processing of nanomaterials and exploring their possible applications are essential aspects of nanotechnology. Research and development in the field of nanotechnology helps in understanding, developing and creating improved, as well as revised forms of materials, devices and systems for future applications. Every field from medicine and electronics to apparels and manufacturing prosper from the advances in nanotechnology, which is multi-faceted in its application. This field of revolutionary technology has attracted strong attention from the researchers across the world.

Nanotechnology maneuvers breakthrough in fields such as- energy, agriculture, catalysts, healthcare and medicines. For instance, the realization of cost effective energy harvest via solar and fuel cells with better efficiency is a current challenge. It can be used to tackle environmental problems and may be used to develop efficient drug delivery processes. Genetic improvement enhances agricultural productivity and can help to make crops resistant to heat and water logging. Nanotechnology has many future applications and possibilities that will become known with further development.

Nanomaterials with desired size, morphology and chemical composition are required in order to study their physical properties and application. In general, particles of less than 100 nm (10^{-9} m) are defined as a nanoparticle, which as a small object behaves as a whole unit in terms of its physical properties. At nanoscale dimensions, the materials are more effective than their larger sized counterparts for two reasons: first, their small size yields a very high surface area to volume ratio; second, when materials are fabricated on the nanoscale, they achieve intriguing surface properties due to their active surface atoms that are not found within their large-sized

counterparts. Nanomaterials including carbon nanotubes, metal nanowires, semiconductor quantum dots and other inorganic nanoparticles (such as gold, silver, copper) are produced through various methods and are being tested for their potential applications.

1.1.1.1. Classification of nanoparticles

Nanoparticles can be classified into two classes:

1. Organic nanoparticles
2. Inorganic nanoparticles

Carbon nanostructures such as fullerenes, nanotubes, graphene are organic nanoparticles, while inorganic nanoparticles may include noble metal nanoparticles (like gold and silver), metal oxide nanostructure, magnetic nanoparticles, and semiconducting nanoparticles (like titanium dioxide and zinc oxide).

1.1.1.2. Importance of inorganic nanoparticles

There is growing interest on inorganic nanoparticles, which show superior material properties with processing and functional flexibility. Inorganic nanomaterials have been widely used in various fields; in medicine field due to their versatile biocompatibility (for instance, titanium based dental implants, hydroxyapatite based artificial bones) and their possibility to get functionalize helps in targeted drug delivery and controlled release of drugs. Glass and paint industries exploit the fascinating properties of inorganic nanoparticles.

In oil companies too inorganic nanoparticles are being added into lubricant formulations to enhance the extreme pressure (EP), anti-wear (AW) and anti-friction properties, thereby improving the efficiency and service life of machinery [1].

1.2. Thesis objective

A growing number of industries are now seeking to commercialize emerging technologies related to nanostructures. The fundamental problem, however, lies in the scaling-up of materials successfully grown and tested in the laboratory, so that they can be produced in bulk and also tested at the scaled up level. The hope of efficient commercialization can be realized on the success of scaling up of individual nanomaterials. It follows that the increasing interest in nanomaterials requires a major step towards the development of more efficient methods for their

synthesis and growth. Rapid development of new cost efficient synthesis techniques for large quantities of nanomaterials is therefore crucial for success.

In this thesis, the application of planetary ball milling for the efficient production of nanomaterials is systematically studied. Three inorganic materials: calcium carbonate (CaCO_3), molybdenum disulphide (MoS_2) and hexagonal-boron nitride (h-BN) are chosen as model systems. CaCO_3 is well known for its detergency and basicity boosting applications. MoS_2 is a widely used material in the field of lubrication specifically in grease having load bearing tendency and antifriction property, while h-BN is used as an AW/load bearing additive.

The main focus is to synthesize the surface capped CaCO_3 nanoparticles, exfoliated MoS_2 nanosheets with suitable exfoliating and stabilizing agent and also synthesizing hexagonal-boron nitride nanosheets (h-BNNSs) by exfoliation via ball milling. Synthesized nanosheets were systematically characterized and their tribological properties are evaluated along with their dispersion stability.

1.3. Review of related literature

1.3.1. Calcium carbonate

CaCO_3 is one of the cheapest commercially available inorganic materials having calcite as the most common form existing in nature, whereas aragonite and vaterite are in metastable forms and convert readily under ambient conditions to calcite form. It has wide applications in oil, paint, plastics industries and agriculture sector. Its applications are determined by parameters like morphology, structure, size, and chemical purity and it is critical to control the shape and size of the particle for the technical applications. Despite its wide applications, CaCO_3 has some disadvantages for instance; being hydrophilic it is not compatible with hydrophobic systems like oil and polymer melts. Hence, to improve these shortcomings, surface modification methods have been used.

1.3.1.1. Significance of surface modifications

The high surface area to volume aspect tremendously increases the surface energy of the nanomaterials, which tend to form agglomerates leading to difficulties in processing the

nanomaterials. Surface modification of nanomaterials will greatly reduce the surface energy and resist particle agglomeration thereby enabling the processing of nanomaterials as per the requirements. Therefore, many studies have been performed on the surface modification of nanoparticles [2–9].

CaCO_3 nanoparticles are hydrophilic in nature and tend to form agglomerates and in particular ultrafine particles of precipitated calcium carbonate (PCC), size $<0.20\mu\text{m}$, are having greater chances for agglomeration. The surface modification is essential to disperse the hydrophilic CaCO_3 in oil medium for over basing application [10]. The surfactants or dispersants are usually amphoteric in nature, containing long hydrocarbon chain (non-polar tail) and a reactive functional groups (polar head), such as a fatty acid (stearic acid (SA), oleic acid (OA)) can be used as a capping agent to impart the surface hydrophobicity on CaCO_3 as given in Figure 1.1 [11, 7].

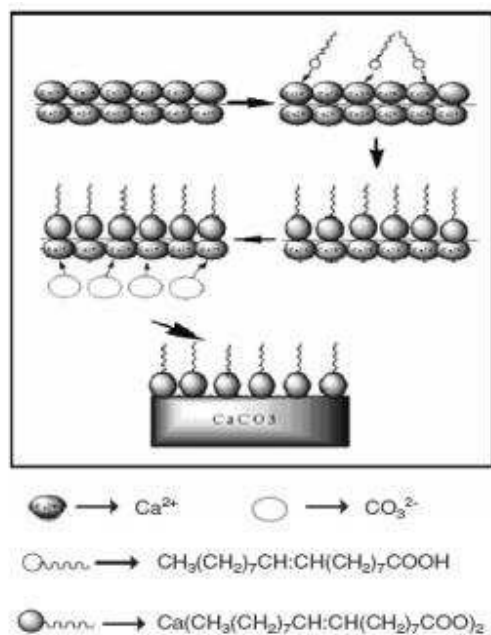


Figure 1.1: Schematic illustration for interaction between the organic substrate and CaCO_3 in aqueous medium [7].

These large molecules containing reactive functional group form covalent bond a with the CaCO_3 surface, leading to organic-inorganic hybrid structures containing CaCO_3 core and long

hydrocarbon chains embedded CaCO_3 shell, and hence the dispersion of total system will be facilitated in the oil medium.

1.3.1.2. Core shell nanoparticles

Nanomaterials possess unique sizes and shapes depending on their physical, chemical, optical and electronic properties, which sometimes cannot be used directly for further applications in the field of medicines, biology and various industries such as polymers or oil. Hence, certain modifications have to be carried out make them compatible, stable and to have material with controlled composition and size. The material should show neither aggregation nor fusion. The synthesis of these materials should satisfy the required application in different fields.

Coating the nanomaterial surface with secondary substances to create a core shell nanostructure is the easiest way to make nanomaterials compatible for various applications in different fields. Core shell nanoparticles are stable nanostructured materials that contain nanoscale cores (two or more) and shell structures, as shown in Figure 1.2. The nanomaterials coated by a secondary substance help in attaining stability over the wider range of experimental parameters like pH, ionic strength, temperature and solvent. It is due to this that engineered core shell nanoparticles have drawn attention and created interest worldwide.

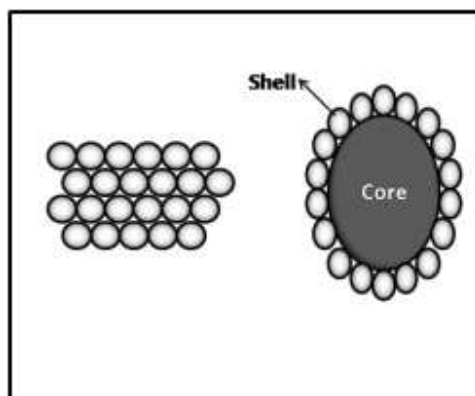


Figure 1.2: Core shell nanoparticles [12].

Core shell nanostructures can be realized with nanoparticles, nanorods and nanowires by using different synthesis routes such as- wet-chemical synthesis, electro deposition, ball milling and chemical vapor deposition (CVD). Synthesizing nanomaterials with core shell structures of different compositions helps in improving their biocompatibility, surface hydrophilicity or

hydrophobicity, as well as their binding with biological molecules. These kinds of nanomaterials allow the introduction of secondary functional groups or multifunctional sites into the materials to engineer them for suitable applications [12].

1.3.1.3. Synthesis of hydrophobic CaCO₃ nanoparticles

1.3.1.3.1. Methodology

The synthesis of CaCO₃ is reported using two basic routes; solution route and carbonation route. The solution route is carried out using double decomposition reaction under aqueous conditions, in which stoichiometric amounts of calcium salts particularly calcium chloride (CaCl₂) and sodium or ammonium carbonates are taken. The carbonation method as the name of the route apprehends, involves purging CO₂ gas into the aqueous slurry of calcium hydroxide (Ca (OH)₂) or freshly formed calcium oxide (CaO) in mediums of different polarity. The process mimics the crystallization of CaCO₃ within living systems and hence is often termed as bio-mimetic synthesis or bio-mineralization of CaCO₃. Amongst the above-mentioned routes the carbonation method is an industrially beneficial one, in terms of environmental preservation and effective use of mineral resources, although the control over shape and surface modification are limited in this method.

1.3.1.3.1.1. Solution route

The solution route is one of the simplest routes and generally involves precipitation of CaCO₃ from water soluble calcium salts under mild conditions. Hydrophobic vaterite CaCO₃ nanoparticles (spike like structures) were synthesized by using chemical co-precipitation method in the presence of OA, which acted as a crystal growth modifier. In the absence of OA both rhombohedral calcite and irregular vaterite particles were formed. It was speculated that OA can prevent phase transformation of vaterite to calcite under precipitation conditions. High concentration of OA (OA: Ca²⁺) in the reaction medium yielded pure vaterite CaCO₃, whereas a mixture of calcite and aragonite was formed with molar compositions of OA:Ca²⁺ < 0.25. The degree of hydrophobicity increases with increasing OA to Ca²⁺ molar ratio as evident from the increasing active ratio from the floating test measurements [13]. Transforming a naturally hydrophilic material to hydrophobic and then finally to super-hydrophobic material has been

brought out [14]. The double decomposition of sodium carbonate (NaCO_3) and CaCl_2 in the presence of OA and heptadecafluorodecyl-trimethoxysilane (FAS-17), respectively, in methanol and ethanol solution yielded hydrophobic to super hydrophobic CaCO_3 . The contact angle measured were 95° (hydrophobic) and 152° (super-hydrophobic), respectively for OA and FAS-17 stabilized CaCO_3 powder [14].

The use of several cationic surfactants offers a new vision for controlling the structure and morphology of calcite crystallization. The cationic surfactants induce the formation the CaCO_3 crystal at ambient temperature. Alteration in CaCO_3 crystal morphologies (laminated cube to sphericity to string shape) was observed with increased concentrations of didodecyldimethyl ammonium bromide (DDAB) and 1-dodecyl-3-methylimidazolium bromide ($[\text{C}_{12}\text{mim}]\text{Br}$). The crystalline forms of obtained CaCO_3 were found to be calcite despite different dose concentration as shown in Figure 1.3 [15]. However, changing DDAB concentration leads to change in both the morphology along with crystalline form, suggesting that the hydrophobic alkyl chains of cationic surfactants helps in regulating the growth of CaCO_3 crystal.

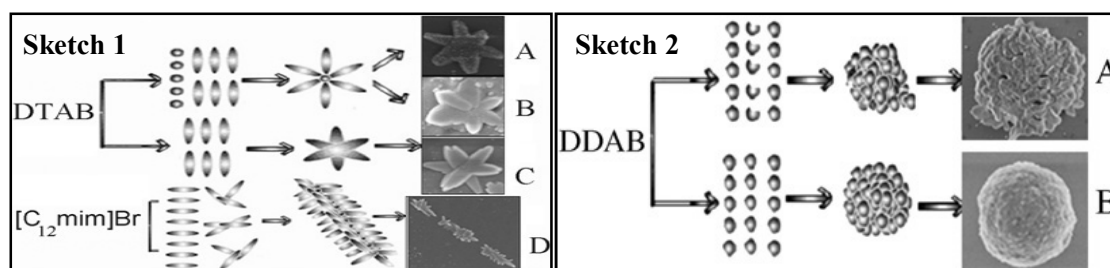


Figure 1.3: Sketch 1: map of different morphology of CaCO_3 crystals prepared in different micelle with different concentration: flower-shaped CaCO_3 crystals formed in the presence of (a) 12.5, (b) 15.0, (c) 25.0 mmol/L DTAB (dodecyltrimethylammonium bromide) and string- shaped CaCO_3 crystals formed in the presence of (d) 60.0mmol/L $[\text{C}_{12}\text{mim}]\text{Br}$. Sketch 2: map of the growth procedure of calcium carbonate crystals with different morphology prepared by different concentration of DDAB: inerratic globosity-shaped and inerratic globosity-shaped crystals formed in the presence of (a) 7.5, (b) 10.0 mmol/L DDAB [15].

The solution route was found to yield better hydrophobic product consuming lesser amount of SA ($\leq 2\%$), compared to dry coating that led to a bilayer coated product [16]. Thus, high hydrophobic CaCO_3 can be attained using suitable low concentration of SA by solution route. However, the right concentration of coating agent must be optimized. A super-hydrophobic

surface with a contact angle as high as 152.8° has been found to be very useful in the area of making self cleaning materials. The surface modification of spin coated nano and micro CaCO_3 film was realized by self-assembled SA coating [17]. The coverage of micro CaCO_3 by nano-sized counterparts played a major role in increasing the surface sliding angle and, in turn, super hydrophobicity with self-cleaning properties.

1.3.1.3.1.2. Carbonation route

In contrast to the solution route, many reports have been found on the carbonation method for the synthesis of surface modified CaCO_3 nanoparticles [7, 18-33].

1.3.1.3.1.2.1. Oleic acid based coatings

Hydrophobic CaCO_3 through OA coating was prepared *in situ* through carbonation of $\text{Ca}(\text{OH})_2$ slurry, which was formed from CaO in an aqueous medium. Ellipse-like hydrophobic CaCO_3 particles were formed and the hydrophobicity was measured through contact angle and floating test. It was concluded that high weight ratio of OA to CaCO_3 promotes the active ratio of CaCO_3 particles in the floating test [7]. Thus, the active ratio of 100% and contact angle of 108.7° was achieved under an optimal dose of OA in the reaction medium.

The high concentration of OA has been found to increase the active ratio, however, only 1.5 to 2.5 Wt% was needed to coat the CaCO_3 particles. The shell comprised of OA and Ca^{2+} deposited on primary CaCO_3 nanoparticles leading to further controlled particle growth to aggregates. The nanoparticle aggregation as reported with high concentration of OA was due to the reunion of nanoparticles, which was facilitated by the interaction of the double bond present in OA [18].

1.3.1.3.1.2.2. Stearic acid based coatings

Like OA, SA is used often to synthesize hydrophobic CaCO_3 . The post treatment method is the most widely employed for the synthesis of SA modified CaCO_3 . However, the *in situ* carbonization method has been found to be economic and environmentally benign and hence quite a few reports were found on the preparation of SA coated CaCO_3 [4]. In a typical carbonation route, SA and NaOH were used as organic substrate and growth medium in aqueous

conditions, respectively, to produce hydrophobic CaCO_3 from $\text{Ca}(\text{OH})_2$ slurry under CO_2 purging at temperature between 20°C and 90°C . Uniform spindle like CaCO_3 nanoparticles with a diameter about 10nm were obtained. SA was found to bring not only hydrophobicity but also induce the growth and morphology of CaCO_3 . TEM studies revealed that the absence of SA yields cubic CaCO_3 whereas a spindle like morphology was obtained in the presence of SA. The active ratio of hydrophobic CaCO_3 depends upon the synthesis conditions like temperature and SA to NaOH molar ratio. An optimal temperature of 60°C and SA: NaOH ratio around 1.0 was found to give an active ratio as high as 99% from the floating test.

The room temperature synthesis of hydrophobic CaCO_3 *via* carbonation route was reported using SA in the presence of polyethylene glycol phosphate (PGP) and NaOH. To study the effect of SA, NaOH and PGP on CaCO_3 surface hydrophobicity, samples were prepared with different experimental parameters such as different ratios of CaCO_3 and PGP and varying ratios of NaOH and SA. The active ratio has been changed by changing the weight ratio of SA to CaCO_3 and PGP. Similarly, the degree of hydrophobicity changes by varying the molar ratio of NaOH to SA. The cooperative interactions between SA and PGP facilitated a chemical coating of the former on CaCO_3 as has been confirmed through Fourier transformation infrared (FTIR) studies. The dissolved PGP in the reaction medium forms micelles that play an important role in increasing the solubility of SA and through electrostatic interaction with Ca^{2+} SA got adsorbed on CaCO_3 . The density of SA (number of SA molecules per nanoparticles) was also calculated by considering the shape of CaCO_3 as cubic and cylindrical [19]. The agglomeration of nano precipitated calcium carbonate (NPCC) was reduced to a larger extent using SA as a surface modifier. NPCC was agitated and mixed with SA in a homogenizer followed by filtration and drying to give SA coated and uncoated NPCC. Scanning electron microscopy (SEM) was used to study the effect of SA on the deagglomeration of NPCC. The mean diameter of agglomerates indicates that SA coating reduced the degree of agglomeration in comparison to uncoated NPCC, 3 wt% of SA was found to be optimum to reduce the excess agglomeration of NPCC at 80°C [20].

In situ surface modification using sodium stearate (Na-SA) by multiple-orifice dispersion microreactor was reported for the first time by Le Du *et al.* [21]. For this study, a multiple-

orifice dispersion microreactor was designed to generate gas-liquid microdispersion system, as shown in Figure 1.4.

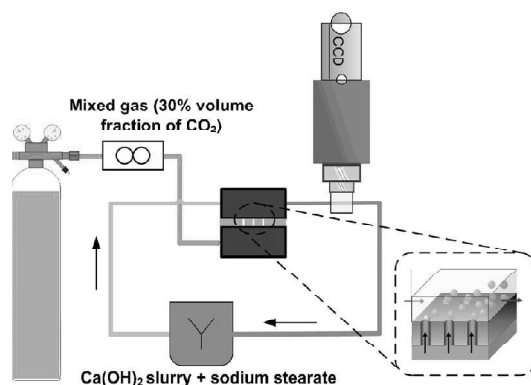


Figure 1.4: The experimental setup for preparing CaCO_3 nanoparticles [21].

Operation parameters like two-phase flow rate and the surfactant influencing the nanoparticles growth were ascertained. The mechanism involving efficient mass transfer that affects the preparation process and the adsorption of Na-SA and calcium ion on solid particles during the *in situ* surface modification process was studied. Obtained particles were highly hydrophobic with a contact angle of 117° and it was demonstrated that temperature control was of great importance as the particle size decreased significantly with the temperature [21].

The use of silane coupling agents was reported to hydrophobic surface of CaCO_3 nanoparticles by grafting. Presence of stretching vibration of methylene and methyl groups in IR spectra suggests that grafting of silane coupling agent over the surface of CaCO_3 was productive. However, the surface modification did not affect the crystallinity of CaCO_3 , whereas with increasing amount of silane coupling agent the diffraction peaks of modified CaCO_3 nanoparticles shifted by small value (increased 2θ). Chemical bonds formed between silane coupling agents and CaCO_3 , leading to steric hindrance which cause reduction in surface energy for better dispersion. Modified nanoparticles showed improved dispersion and interfacial compatibility (studied using rheological measurement) with styrene-butadiene rubber (SBR) [22].

The ultrasonication technique was found to be suitable to coat NPCC with SA. NPCC was ultrasonicated at various amplitudes in ethanol medium containing SA at different temperatures. Other coating methods like dry milling, aqueous coating and direct coating were also employed. It was found that uniform coating with retention of cubical shape was observed during ultrasonication, while dry or aqueous modification shows non-uniformed coating and shape, as shown in Figure 1.5.

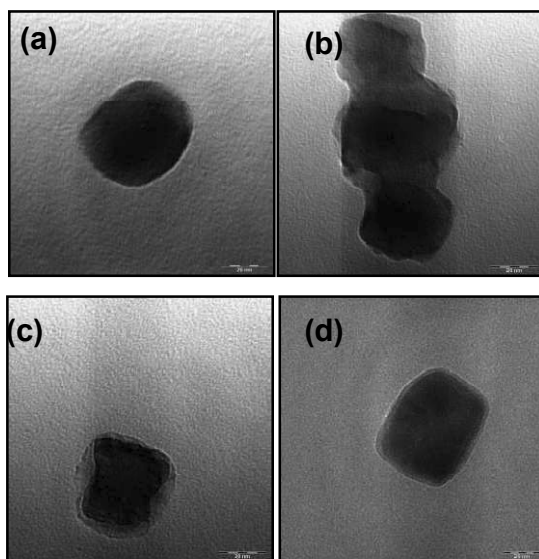


Figure 1.5: TEM images of (a) uncoated NPCC, (b) NPCC coated in aqueous, (c) NPCC coated with dry ball milling and (d) NPCC coated with ultrasonication [23].

Thermogravimetric (TGA) studies revealed the presence of monolayer, local bilayer and free acid from different coating processes. The direct coating leads to deagglomerated NPCC and shows no free acid or local bilayer as excessive SA dissolved in ethanol. The free acid along with local bilayer was observed in aqueous medium NPCC coating because of rapid precipitation of SA in water. In the case of dry milling, there was the formation of a fused layer of SA on the surface of NPCC as a result of high impact forces by milling. In contrast, during ultrasonic coating, a local bilayer was detected forming multilayer adsorption over NPCC without fusion of coating layers [23]. Although coating with SA by both ultrasonication and dry milling showed drawbacks for the coating process, the agglomeration of nano CaCO_3 was controlled.

1.3.1.3.1.2.3. Terpineol based coating

In contrast to commonly used OA and SA, there was a report that examined the applicability of a rare capping agent. The influence of terpineol (2-(4-Methyl-1-cyclohex-3-enyl) propan-2-ol) was studied as a surface modifier on the size and morphology of CaCO_3 particles, *via* carbonation route [24]. Various parameters like CO_2 flow rate, stirring speed and terpineol dose were studied. It was found that fine bubbles of CO_2 were produced by fine gas jet nozzle, which is found to be better for good dispersion and mass transfer of CO_2 . Similarly, increasing the stirring speed improves CO_2 mass transfer into $\text{Ca}(\text{OH})_2$ slurry that hastened the formation of fine spherical particles. The optimized dose of 0.1-1.0 vol % terpineol was observed to be effective for the preparation of fine CaCO_3 particles; however, higher terpineol dosage decreased CO_2 mass transfer that reduced the rate of carbonation and thus the formation of larger CaCO_3 particles became inevitable.

1.3.1.3.1.2.4. Dodecanoic acid and octadecyl hydrogen phosphate based coatings

Dodecanoic acid (DA) is another capping agent widely used for the surface modification of CaCO_3 . Cubic hydrophobic CaCO_3 was prepared through carbonation of $\text{Ca}(\text{OH})_2$ in the presence of DA at 20°C . Synthesis parameters like temperature or the weight ratio of DA to $\text{Ca}(\text{OH})_2$ influence the growth of CaCO_3 , morphology and hydrophobicity. IR studies indicate that the calcium salt of DA formed over CaCO_3 acts as hydrophobic shell. The surface hydrophobicity increases with increasing weight percent of DA and reaches saturation at a contact angle value of about 120° . The surface of CaCO_3 was completely covered with certain concentration of DA (3.98 wt% or more) and thus further increase in hydrophobicity was not observed with increasing the concentration of DA[25]. The concentration of DA and the temperature of the medium controlled the obtained particle morphology. Cubic structures transformed into spindle-like particles were obtained with high dosage of DA at temperature above 60°C . Nevertheless, as found from the higher contact angle, increasingly the surface of CaCO_3 nanoparticles became hydrophobic due to larger surface coverage with high dosage of DA.

Another reported literature claimed the production of rod and ellipse-like particles via carbonation method using mixture of $\text{Ca}(\text{OH})_2$ and DA by bubbling a gas mixture (CO_2/N_2). Variation in the hydrophobic character by changing temperature (influencing the interaction of

DA and CaCO_3) and concentration of DA (effect on active ratio of CaCO_3 particles) was studied. Under optimized conditions (40 °C and the molar ratio of DA to Ca^{2+} was 4:1000) particles obtained show 100 % active ratio [26].

The influence of process pH and time of adding capping agent on the coating process was also studied [27]. The addition of octadecyl hydrogen phosphate (ODP) during the digestion stage yielded smaller particles by inhibiting/controlling the CaCO_3 crystal growth; whereas at process pH = 7 the surface coating was observed to be maximum to give hydrophobic CaCO_3 . It was shown that organic substrate (ODP) induces the nucleation and growth process of CaCO_3 where hydrophobic spindle like CaCO_3 particles were prepared [28]. It was observed that concentration of ODP had great influence on the active ratio as well as on the morphology of CaCO_3 particles. The low concentration of ODP had no or negligible influence on the nucleation and growth of particles that lead to cubic particle morphology. The mean particle length of hydrophobic CaCO_3 was quite sensitive to the variation of concentration of ODP; an increased particle length suggests that different concentration of ODP results in dissimilarity in particle length. Hence, it was shown that nucleation and growth were induced by organic substrate (ODP). Core shell surface modified hydrophobic CaCO_3 nanoparticles were fabricated using Na-SA as surface modifier, as shown in Figure 1.6 [29].

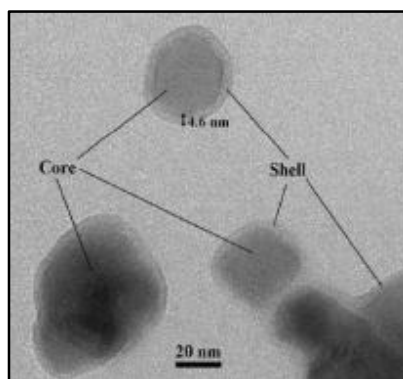


Figure 1.6: Core shell structure of nanosized-PPC [29].

The role of phase interfaces (solid–liquid, gas–liquid, gas–solid) was of particular importance, because mass transfer, as well as heterogeneous nucleation or epitaxial growth, can occur at interfaces. An empirical approach was made using experimental design techniques to determine the effects of process parameters such as conductivity, temperature, CO_2 flow rate, stirring rate and mass concentration of $\text{Ca}(\text{OH})_2$ suspension on the specific surface area of PCC. The impact

of these experimental parameters on the nucleation, surface modification and the particle size aspects were studied and correlated through an empirical model.

Unlike Na-SA, sodium oleate (Na-OA) comprises of double bond, which enabled Na-OA to copolymerize and thus CaCO_3 would be encapsulated by polymers. The influence of addition time and dosage of Na-OA were studied [30]. It was found that addition of Na-OA at three different stages of synthesis has different effect on the active ratio of the product. The addition of Na-OA during the digestion time achieved a better result (fine calcite CaCO_3 particles) than that at initial stage or at medium pH=7. Similarly, different dosage of Na-OA was added during digestion time in order to optimize dosage and it was realized that contact angle increased from 53.9° (Na-OA 1 wt %) to 123.8° (Na-OA 2 wt %) and beyond that only a saturation in contact angle was observed. TG-DTA study on the comparison of traces from Na-OA, calcium oleate (Ca-OA) and coated CaCO_3 showed the presence of a small amount of Ca-OA and no traces of Na-OA in the sample. Further, it was noticed that the amount of Ca-OA increased with the increasing the Na-OA dosage. Hence, it was concluded that the sample hydrophobicity was due to the deposition of Ca-OA formed during the reaction on the surface of the CaCO_3 particles.

The synthesis of active hydrophobic CaCO_3 nanoparticles by an environmentally benign route was reported using linseed oil as a surface modifier [31]. The addition of saponified linseed oil to the $\text{Ca}(\text{OH})_2$ slurry followed by CO_2 purging under constant stirring at pH =7 yielded fine calcite CaCO_3 . The results revealed that the smaller particles obtained low process temperature ca. 20°C . The active ratio of product increases with increasing weight ratio of linseed oil to CaCO_3 nanoparticles. IR and TG-DTA results confirmed the coating of linseed oil over the CaCO_3 surface. The IR spectrum of linseed oil coated CaCO_3 shows absorption peak characteristics of linseed oil in cm^{-1} at 2922 (H-C-H asymmetric), 2876 (symmetric) and 3024 (C=C-H asymmetric stretching), which were not observed from uncoated CaCO_3 .

The binding ability of the surfactants over the specific crystal face of CaCO_3 affects the crystal growth and morphology of CaCO_3 . The morphology of the obtained CaCO_3 in CO_2 pressurized autoclave was clearly different from those CaCO_3 nanoparticles synthesized in the absence of surfactants under similar conditions. The non-ionic surfactant Tween 80 preferably interacts

with the neutral plane ($\{1\ 0\ 4\}$) of CaCO_3 . Thus, the reaction between hydrated CO_3^{2-} and Ca^{2+} ions on the $\{1\ 0\ 4\}$ plane was inhibited and the growth speed of this face was slow resulting in the final formation of the plate like morphology. On the other hand, anionic surfactant Na-SA can be adsorbed onto the positively charged faces such as $\{0\ 0\ 1\}$, $\{1\ 0\ 1\}$, $\{1\ 1\ 0\}$ inhibiting the growth of these faces leading to the formation of cubic particles with rough surfaces. In contrast, cationic surfactant, CTAB does not have a considerable effect on the morphology of the obtained nanoparticles. It may be due to the electrostatic repulsion between the positively charged head group and the Ca^{2+} ion, which makes the adsorption of CTAB difficult onto the CaCO_3 faces [32].

The effect of different surface modifiers on crystal morphology and structure of CaCO_3 were studied [33]. They reported *in situ* synthesis of hydrophobic cubic and spindle like configuration of CaCO_3 by bobbling (gas-liquid-solid) method. Electron microscopy images revealed OA gave small cubic crystals while Na-SA and ODP produces spindle like particles. X-ray diffraction (XRD) characterization revealed that product obtained was calcite in nature despite of addition of different modifiers which gave dissimilar morphologies and sizes. The effect of a modifier dose was investigated and it was concluded that an optimum modifier dose (2%) was required to attain maximum hydrophobicity. This modified CaCO_3 has been used as a filler to improve the mechanical properties of polymers such as PVC. The properties like rupture intensity pull intensity and fuse temperature of PVC improved due to its compatibility and affinity with the modified CaCO_3 nanoparticles [33].

1.3.1.3.1.3. Milling

Ball milling is defined as a process in which the mechanical breakdown of solids into smaller particles occurs without any change in their state of aggregation [34]. Particles of certain shape and sizes (including nanosize) can be produced using ball mill, which will increase the surface area and defects will be induced into the solid structure. Along with the increase in surface area there will be increased proportions of high active surfaces due to the induced defects. This is also known as the mechano-chemical method and it is widely used for the synthesis of nanoparticles and nanocomposites. However, size reduction through this route is dependent on dispersant molecules and is time-consuming.

The literature shows that surface modification of CaCO_3 was very effective via milling approach. In wet-milling approach *in situ* modification of newly created surfaces of the small molecules using surfactant molecules is done to generate hydrophobicity. This small molecule surface modification continues until creation of new surface is exhausted due to the limitation of the milling parameters, process conditions, or until the surface potential energy is neutralized with the organic dispersant molecule. However, dry-milling reduction in the particles size is difficult as newly generated surface have high energy that leads to particle agglomeration and also the chances of contamination during milling through mill (vial and balls) are greater.

Unlike in solution and carbonation routes, where certain conditions (reaction time, temperature, gas flow, pH) exist that crucially affect the crystal growth and morphology of CaCO_3 ; in the ball milling process no such problems arise, except for milling parameters (milling speed/time, modifier dosage, ball to mineral ratio, milling media). However, these parameters can be controlled in an industrial scale with ease to give better tailored hydrophobic materials. The desirable phase and morphology of the solids (for instance calcite and cubic CaCO_3) can be selected for milling with a suitable surface modifier.

Chemically synthesized CaCO_3 through the precipitation method was ball milled and the phase transition was studied with respect to milling time in toluene medium. The sample prepared in wet medium is primarily vaterite with a small amount of calcite with increased milling time, the formation of calcite phase increased with a small amount of vaterite to aragonite transformation occurred. About 25% of calcite formed after 19 hours of milling. The crystallite size of vaterite hardly changed as it remained over 30nm whereas the calcite crystal reduced to one third of its original size [35].

A mechano-chemical route was reported on the synthesis of nano calcite CaCO_3 in a NaCl matrix through solid state displacement reaction between CaCl_2 and Na_2CO_3 caused by milling followed by heat treatment at 350°C . TG-DTA results revealed that after 4 h milling the reaction was incomplete as evident from an exothermic peak at 295°C that was attributed to CaCO_3 formation through the steady state displacement reaction between CaCl_2 and Na_2CO_3 . Further, the milled product was heat treated in air at 350°C and later washed to obtain single phase CaCO_3 . The particle size of CaCO_3 was dependent on the volume fraction of CaCO_3 formed in the salt matrix; 20% volume fraction of CaCO_3 resulted in 142 nm whereas 10% led to 77 nm particle size [36].

Another mechano-chemical route accounted for the surface modification of CaCO_3 using Na-SA as modifying agent in a wet stirred mill. The effect of milling conditions on the modification of CaCO_3 was studied; the influence of Na-SA dosage on CaCO_3 particle size shows remarkable improvement in particle size (d_{50}) reduction from 16.33 (before milling) to 1.33 μm (after milling) respectively, the active ratio improved from 35 to 98%. Milling not only reduced the particle size but also increased the specific surface of the sample. It was found that modification effect was highest when the particle size was 1.33 μm , which is the optimum size to use the sample as fillers for rubber products.

The intensity of crushing mechanical force resulted from changing the parameters like milling time, rotary speed and the mass ratio between grinding media and mineral feeding effects final phase and morphology. The range of the mechanical crushing force must be suitable to generate ultra-fine grinding and the best-modified product. If the crushing intensity is too weak or there is no grinding action, the modification effect would be poor because of ineffective activation of the sample surface. If the intensity was too high, the modification effect would again be poor as the finer particles need more modifying agent. The optimized condition was found to be a mass ratio of five between grinding media and mineral (CaCO_3 powder), with 1000 rpm rotor speed. The difference in Ca $2p_{3/2}$ energy level obtained from XPS at 346.75 (before) and 346.30 eV (after modification) confirmed Na-SA adsorption on the surface of CaCO_3 [37].

The mechano-chemical energy associated with the milling process triggers the polymerization of styrene monomers and facilitates the polymer grafting onto the surface of CaCO_3 particles, resulting in a potential filler material. About 30-40% styrene was found to be sufficient for best surface grafting as higher amount of polymer lead to particle adherence [38]. Na-OA was also used as surface modifier in the milling process to make hydrophobic CaCO_3 with a higher active ratio in a floating test [39]. A mechano-chemical method was introduced, in which CaCO_3 and SA was milled in the presence of n-decane in a horizontal stirred ball mill [40]. Various characterization techniques were used to evaluate the starting and modified CaCO_3 . The doses of SA were optimized in order to obtain monolayer coverage/ coating over the CaCO_3 surface. It was found that 1% SA modified CaCO_3 shows the maximum active ratio however, increased SA content leads to a decrease in the active ratio due to multilayer physical adsorption through tail-to-tail arrangement of non-polar groups. Characterization techniques like TG-DTA were able to

differentiate between chemisorbed, intercalated (local bilayer), and free acid molecules, which may be present on the surface of calcite fillers. Similarly, the surface of CaCO_3 after modification becomes smooth and uniform due to strong mechano-chemical effects [40].

1.3.1.4. Tribological applications of CaCO_3

Lubricants function as friction and wear reducers between the moving asperities. Many performance-enhancing additives are added to improve the properties of lubricants depending upon the requirements. Due to the emergence of nanotechnology, the newly developed products available have the potential to outperform the traditional lubricant additives. These traditional lube additives contain heavy metal (Mo, Zn)-based sulphur or phosphorus additives as performance enhancers, which provide effective wear and friction protection on engine parts through the formation of glassy polyphosphate AW film. However, the formation and deposition of sulfur and phosphorus species on the automotive three-way catalytic converter lead to catalyst poisoning, a well-known problem. Acid sulfur and phosphorous lead to engine parts corrosion and wear during prolong usage. Therefore, green additives have received more attention recently and hydrophobic CaCO_3 nanomaterials are one of the potential candidates in lube technology [1]. Generally, fatty acid salts of CaCO_3 has excellent cleaning (detergency) and dispersion properties that can guarantee the effects of cleaning fuel combustor parts, piston ring, cylinder and reduce carbon and lacquer deposition. It also primarily enables the lubricating oil to maintain necessary total base number (TBN) to neutralize the vitriol resulted from using high-sulfur fuel [41].

Overbasing is one of the most important applications of CaCO_3 in lubricants. An increasing range of additives are added into lubricating oils to enhance the chemical stability, wear and friction reducing properties. The so-called overbased additives (detergents), are colloidal nanoparticles of CaCO_3 (or $\text{Ca}(\text{OH})_2$) stabilized by a surfactant layer. The term overbased refers to the fact that the quantity of base incorporated in the particle cores is greater than that needed to neutralize the acid surfactant. The neutralizing strength of an overbased detergent is measured by its TBN. The nano detergents essentially consist of an inorganic core (15–40 mass %) stabilized by oil-soluble surfactants (20–45 mass %) incorporated into lubricating base oil, as depicted schematically in Figure 1.7.

Various by-products are formed, including inorganic and organic acids, due to the oxidation of sulphurous and nitrogenous impurities during fuel combustion. The oxidative degradation of the lubricant leads to the formation of organo-acids. If allowed to build up, these acids would cause severe corrosion to machinery parts, especially under engine start-up conditions. These nanoparticles are relatively insensitive to temperature, which explains their effectiveness at high temperatures as slow-release acid neutralizers.

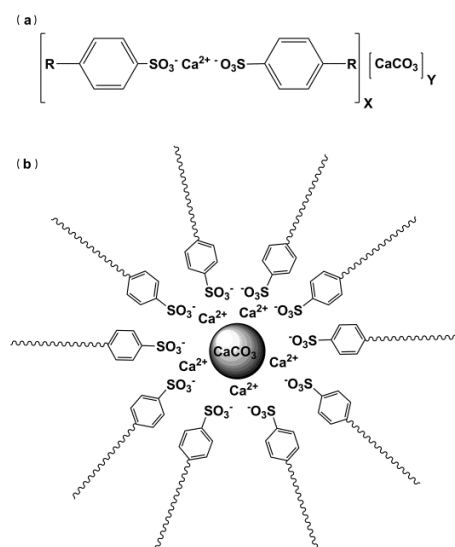


Figure 1.7: Schematics of (a) overbased sulfonate and (b) its micellar form[42].

The principal functions performed by detergents in engine oil formulations are: (1) acid neutralization, (2) high temperature detergency, (3) oxidation inhibition and (4) rust prevention. These functions promote engine cleanliness, fuel efficiency and extended trouble-free operation. The surfactants most commonly used are phenates, sulphonates, salicylates or phosphonates, which act as surfactants to stabilize the CaCO_3 particles [42].

Surface modification using various surfactants effectively reduces particle agglomeration and thereby the efficiency of processing CaCO_3 nanoparticles for various applications has improved greatly. Surface modified CaCO_3 is useful to make overbased lubricants with desired TBN as per the requirements. It also enhances the load bearing capacity, wear and friction reducing properties of lubes. Long chain hydrocarbon tail embedded on the surface of these nanoparticles also acts as dispersant to stabilize carbon soot and lacquers. This brief survey clearly indicates

the potential applicability of surface modified CaCO_3 nanoparticles in the field of modern lubricants.

1.3.2. Molybdenum disulfide

MoS_2 is the most common solid lubricant with a slippery or greasy touch. This blue-grey or black solid is a layered hexagonal lattice material [43], in which Mo (IV) occupies trigonal prismatic coordination sphere surrounded by six sulphide ligands, where, each sulphur centre is pyramidal connected to three Mo centers. Hence, layered structure was formed by interconnected trigonal prisms [44]. MoS_2 , being second only to graphite in some cases, exhibits superior lubricity amongst antifriction additives. However, it is almost insoluble in all solvents, including lubricants, and, therefore, its application is limited to grease in fine form [45]. It possesses good load bearing capability and can be used in high vacuum application due to its low volatile nature.

The good lubricity of MoS_2 is due to its lamellar structure that can orient parallel to the direction of motion. The MoS_2 particle size affects its properties and usage, for instance, larger particles are abrasive, by imparting excessive wear give better performance on rough surfaces, while small and fine particles are best for smooth surfaces at low speed [46].

Unlike graphite, MoS_2 do not depend on the presence of adsorbed vapors to act as lubricant. Therefore, it can be used satisfactorily in high vacuum and temperature applications. It can still be used for short periods up to 450°C despite MoS_2 begins to oxidize at 350°C in air. The oxidation produces molybdic oxide (MoO_3), which itself is a fair lubricant at higher temperature but wears rapidly. Apart from oxidation, it is stable to most chemicals, but can be attacked by strong oxidizing acids and alkalis. Overall, MoS_2 is a versatile and useful material where oils or greases cannot be used or do not have sufficient load carrying capacity [43]. However, due to its insolubility in organic media, the tribological applications of MoS_2 are limited and it is easily oxidized in air to molybdenum oxides, which have a negative influence on the AW and friction reduction properties of the lubricating oil.

There are different methods to synthesize surface capped MoS_2 nanoparticles/nanosheets. Few papers have reported that the synthesis method not only influences the stability but also the cost effectiveness. Most of the reports covered chemical methods to synthesize MoS_2 with different

dispersants by both top-down and bottom-up methods. We briefly discuss here some bottom-up methods along with a top-down approach (milling method) to prepare MoS₂ nanoparticles.

Duphil et al. [47] has reported that spherical crystalline nanosized MoS₂ with curved basal planes were obtained after annealing the amorphous precursor incurred from Mo(CO)₆ under reflux conditions. However, the by-product CO is highly toxic [47]. Surface-capped MoS₃ nanoparticles were prepared using reversed micro-emulsion route with several surface capping agents such as dithiocarbamate (DTC), amines, carboxylic group, alkoxy thiophosphinate and succinimide based dispersants have been used. The synthesized nanoparticle radius was found to be below the 3nm range as determined using small angle x-ray scattering (SAXS). Excellent tribological properties were demonstrated by hydrocarbon soluble nanoparticles with good control of sulphur and/or phosphorus quantity in lubricant [48].

Since the discovery of inorganic fullerene (IF) like nanoparticles, many reports were found on the synthesis of IF-MoS₂, which exhibit superior lubricity than the 2H-MoS₂ (hexagonal form of MoS₂). The reported method yields a cost effective method that involves the reaction of ammonium molybdate with sulfur in presence of hydrogen at different annealing temperature yielding nanoparticles in the range of 10-20nm having hollow cage structure along with nanowires and nanotubes. This hollow cage structure possesses high elasticity by allowing the particles to roll rather than slide between the mating parts in appropriate loading regime [49].

Several physical and chemical methods were used to prepare IF-MoS₂, such as gas-phase or solid-gas reactions [50, 51], electron beam irradiation activation [52], arc discharge [53] and thermal decomposition [54]. The growth mechanism of IF-MoS₂ was also studied to understand the formation of fullerene like structure from respective metal oxide precursor. The product purity achieved by the process was good and a narrow particle size distribution was obtained in some cases. However, the tribological application of IF-MoS₂ in lubricant formulation is likely limited, due to the smaller quantity of material prepared using these approaches, which are seldom cost effective with respect to application [55-57].

A novel method which can be scaled up at industrial level is the formation of high quality two dimensional (2D) nanosheets of MoS₂ and WS₂ using oleylamine to avoid agglomeration, oxidation and inherit the functionalization property that helps in introducing new properties to

hybrid organic-inorganic nanocomposite. The low temperature (360°C) synthesis involves the production of stable nanosheets at two different time intervals (30, 90 min) in which a single source precursor (containing both metal and sulphur) decomposes in oleylamine. Various characterizations were performed to check the effect of reaction time on reaction products. It was observed that a single layer was obtained after 30 min of reaction followed by assembly of few layers through van der Waals interactions after 90 min of reaction time. IR spectra were acquired to investigate whether surface of nanosheets was capped [58].

Mixed-solvothermal approach was used for synthesizing different morphologies of MoS₂ nanosheets with different solvents. Solvent effect on growth and morphology of the final product was also studied. It was found that MoS₂ obtained with water/ethanol/N-Methyl pyrrolidone (NMP) solvents demonstrate the layered structure with interlayer spacing of (002) plane of 0.62 nm corresponding to 2H-MoS₂. However, MoS₂ with water/ethanol/ethylene glycol solvents displays fullerene like structures.

The formation of different morphologies is due to the absorbing effect of two mixed-solvents over the MoS₂ surface, for instance, ethylene glycol over the surface of MoS₂ prevents regular crystallization and hence reduced layer stacking [59].

Large flake sizes of exfoliated MoS₂ were prepared to give high concentration dispersion under optimized conditions using NMP as solvent. Using this method, the flakes of length ~2 μm-4 μm (maximum size) can be produced. This report confirms that controlled centrifugation helps in isolating MoS₂ flakes with various dimensions [60].

The mechano-chemical synthesis of MoS₂ nanoparticles from MoS₃ via high energy ball milling was reported on the effect of milling time and speed [61]. The MoS₃ precursor was ball milled for 24 h, followed by washing with carbon disulfide, HCl, alcohol and deionized water yielded MoS₂ as final product. The appearance of (100) and (110) peaks in XRD indicated the presence of MoS₂. It was obscured to claim complete conversion of precursor MoS₃ to MoS₂ because the peaks were broadened due to the milling effect. The complete conversion of MoS₃ to MoS₂ was confirmed with the help of differential scanning calorimeter (DSC) results. The milled product was typical lamellar hexagonal MoS₂ having rich active sites for hydro-desulfurization catalysis. On further annealing the sample to 850°C for 30 minutes, results in converting the short low

stacked MoS₂ layer into long high stacked layers, while retaining the hexagonal structure. Short low stacked layers were found useful for catalytic activity as active centers of HDS reactions were located on the edges of the MoS₂ slabs. It was concluded that there was an increase in local temperature during milling to around 375°C, as the sample obtained after milling was similar to that obtained by thermal decomposition.

A combined ball milling and catalytic route was proposed for the synthesis of multi-walled MoS₂ nanotube; ammonium tetrathiomolybdate [(NH₄)₂MoS₄] was ball milled and then converted to MoS₂ in the presence of C₄H₄S and hythane mixture [62]. The catalytic thermal decomposition condition controlled the nanotube growth. Various techniques were used to characterize the multi-walled product. The hexagonal polycrystalline MoS₂ was observed using XRD only after thermal decomposition. Long entangled nanotubes with an average length 3-5 micron were observed over the large area in scanning electron microscopy (SEM) and the diameter was confirmed as 30-50 nm in transmission electron microscopy (TEM) shown in Figure 1.8 [62].

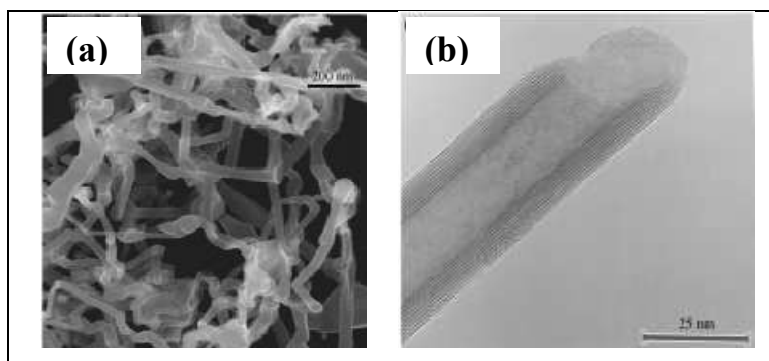


Figure 1.8: (a) SEM image of the as-synthesized MoS₂ nanotubes and (b) HRTEM of the as-synthesized MoS₂ nanotubes [62].

MoS₂ nanoparticles for tribological application were synthesized via ball milling in different media. Milling was performed in steel vials for different time intervals in selected media (air, canola oil and hybrid of air and canola oil, i.e., milling in air followed by canola oil) with twice the ratio of balls with respect to the reactant. Conventionally available MoS₂, dry milled MoS₂ and hybrid milled MoS₂ were chosen for tribological testing. These samples were added to paraffin oil at 1% concentration for evaluating the wear scar diameter (WSD), coefficient of

friction (CoF) and the EP properties [63]. There was substantial improvement in AW and antifriction properties by using this hybrid product. Further, EP was improved for the hybrid sample showing that inorganic nanoparticles intercalated with organic molecular medium can significantly enhance the tribological performance.

A micro-domain reaction method was established for MoS₂ nanosheet synthesis. Method involves the ball milling of MoO₃ and S in order to get homogeneous distribution, close contact and quick reaction to produce MoS₂ thin films, which inhibits the formation of oxide core and hence MoS₂ nanosheets were formed. Ball milling plays an important role by activating and homogeneously distributing the reactants leading to fast reaction and limiting particle size in micro-domains. For the tribological study, samples were prepared by adding the synthesized nanosheets to base oil along with 1 wt% of surfactant (Span-80) followed by sonication. AW performance was tested and it was found that 1.5% of nanosheets gave the smallest wear scar (0.3mm), smaller than that of base oil (0.72mm). Load bearing capacity (P_B) of lubricating oil was determined to be very less (392 N) in comparison to lubricating oil with 1.5% of MoS₂ nanosheets yields 1048 N [64].

1.3.2.1. Tribological applications of MoS₂

The machining application of MoS₂ in minimum quantity lubrication (MQL) has been discussed by Kalita et al. [65]. A dispersion of MoS₂ added with lecithin was prepared in commercially available base oils; paraffin oil, soyabean oil and commercial MQL metal working fluid in two concentrations by weight (20% and 5%). Their tribological properties were tested from the measurement of grinding forces, grinding ratio (G-ratio), CoF and wear track analysis. It was found that MoS₂ nanoparticles offer unique advantages in MQL when they present the possibility of navigating in the grinding zone and delivering reduction of grinding forces and most distinctively increase the life of expensive grinding wheels by increasing G-ratio [65].

Tribological properties of IF-MoS₂ were compared with that of bulk MoS₂ and IF-WS₂ in two types of poly alpha olefin (PAO) synthetic oils. IF-MoS₂ nanoparticles were prepared in a quartz reactor by reacting vapors of MoO₃ with H₂S, which allows full conversion of oxide to sulphide at 840°C for 20h. The obtained particles were about 70 nm in size, crystalline in nature and less agglomerated as compared to IF-WS₂. The friction coefficient, contact pressure and friction

coefficient with cycle number at three contact pressures were measured. It was found that under high pressure and low humidity IF-MoS₂ demonstrate low friction coefficient (0.03) with the smallest wear rate. However, the performance was found to deteriorate due to its inferior chemical stability compared to IF-WS₂ after 2500 cycles [66]. Tribochemistry of such IF like metal dichalcogenides is well known. The tribochemical reaction mechanism is believed to be in two steps, viz., the fullerene structure gradually flowering to exfoliated layers and then the sheets occupying onto asperities of the rubbing surface to give protective film. The analysis of worn surface showed the presence of tribofilm composed of hexagonal MoS₂ incorporated into iron oxide layer, as given in Figure 1.9. [67].

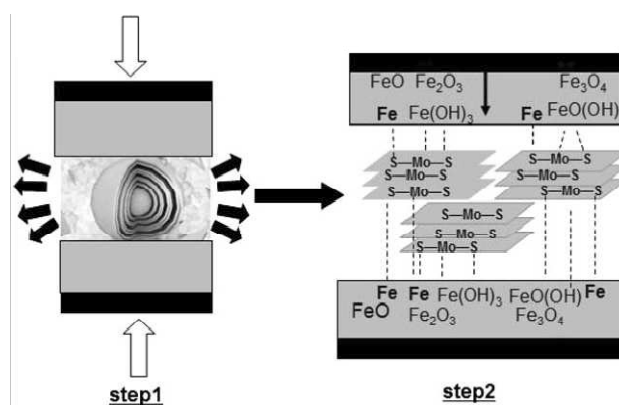


Figure.1.9: Possible tribochemical mechanism of IF-MoS₂ nanoparticles on steel surfaces [67].

Interestingly, Cyanex 302 ((bis(2,4,4-trimethylpentyl) monothiophosphinic acid)) modified MoS₂ microspheres (MS-MoS₂) dispersed in base oil 500SN demonstrate better tribological properties than the commercial colloidal MoS₂ (CC-MoS₂). The friction-reduction and AW properties of the lubricants were examined using an Optimol SRV oscillating friction and wear tester. The EP characteristics of the base oil with or without MoS₂ additives were evaluated using a Seta-Shell four-ball EP tester. The chemical states of some typical elements on the worn surfaces of the flat discs after the wear experiments were examined using x-ray photoelectron spectroscopy (XPS). As shown in Figure 1.10a, signals of Mo, P and S did not appear from the worn surface, indicating that CC-MoS₂ has not undergone tribochemical reaction or deposited as tribolayer between moving parts. In contrast, the system of MS-MoS₂/oil shown in Figure 1.10b, gave signals of P 2p at 133.7eV, attributed to FePO₄, Mo3d characteristic double peak appearing at 228.4 and 232.8eV from Mo⁴⁺ of MoS₂, and S 2p around 162.9eV attributed to S²⁻ of MoS₂.

This result indicates that thin tribo film composed of MoS_2 , FeS , Fe_2O_3 and FePO_4 formed, which acted as solid lubricants during the friction process, giving rise to good friction reduction and AW performances on the surface of the lubricating pair [68].

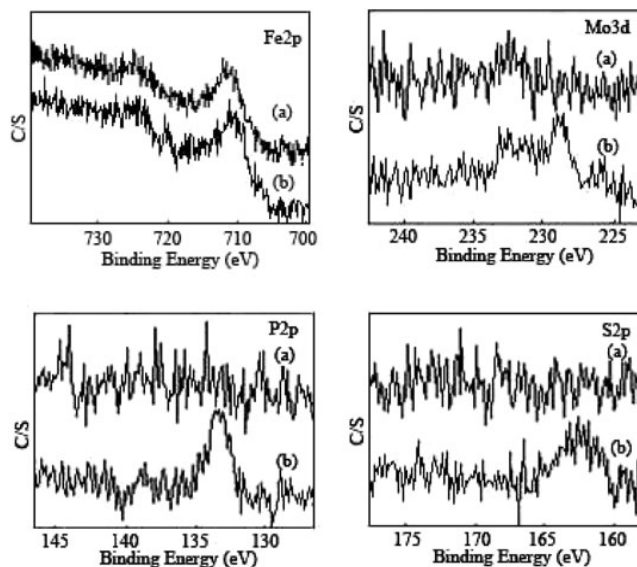


Figure 1.10: XPS spectra of typical elements on the worn surfaces lubricated with (a) 0.50% CC-MoS₂/oil and (b) 0.50% MS-MoS₂/oil at 200 N [68].

Similar chemically adsorbed surface protective film was observed elsewhere while testing tribological properties in LP (liquid paraffin) of Cyanex 301 (di-(2, 4, 4-trimethylpentyl) dithiophosphinic acid)) modified nano-hollow spheres (NH) of MoS_2 . The performance of this solvothermal synthesized NH-MoS₂ was excellent compared to CC-MoS₂ and liquid paraffin. The friction coefficient decreased with increasing the additive (CC-MoS₂ and NH-MoS₂) concentration in liquid paraffin; the friction coefficient from NH-MoS₂ was found to be less than that of CC-MoS₂. The higher wear loss volume observed with low concentration (up to 0.25%) NH-MoS₂ in LP compared to CC-MoS₂ was not clear and the reason has not been described. However, 0.5% of NH-MoS₂ in LP, an optimum concentration, had shown good sliding and rolling effect resulting in the least friction coefficient and wear volume loss under all applied loads [69].

The effect of lubricating condition as well as additive morphology (MoS_2 nano-balls, nano-slices and bulk MoS_2) was compared one to one to derive the comparison in tribological properties between micro and nano MoS_2 . It was found that nanosized MoS_2 function as better lubricating

additive in LP compared to micro-MoS₂. This was due to the small size of nanosheets (5-10 nm) that easily fill the asperities present on the interface of the friction pair.

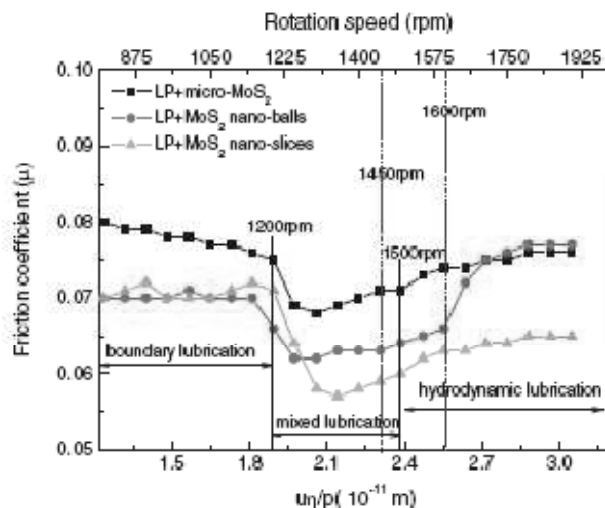


Figure 1.11: Stribeck curves of steel balls lubricated by liquid paraffin and MoS₂ particles in point-contact friction [70].

The Stribeck curves (Figure 1.11) show the different lubrication region with respect to rotation for the three samples. Under boundary conditions, the interface was too small and oil film thickness allows only nano-balls and slices to enter and lubricate the rubbing surface. In the mixed and hydrodynamic lubrication region at higher rpm the oil film thickness increases and more amounts of nano-balls and slices could fill the asperities. However, it was contradictory to the previous reports that nano-balls at mixed and hydrodynamic regions (higher rotation) show more friction. It was proposed that the curved basal surfaces of the nano-balls were highly reactive and, at faster rpm, generates heat and decomposes LP, which leads to increased friction. Thus, nano-slices were found to be more advantageous in high sliding speeds [70].

From the detailed literature it was concluded that most of the reported work focused on synthesis of MoS₂ nanoparticles like: nanotubes, nanospheres. There is lack of literature in the area of production of MoS₂ nanosheets via top-down approach (milling) and their application in tribology. These studies mainly described the preparation of MoS₂ nanoparticles dispersion in oil for tribology testing, without giving any knowledge about the stability of the dispersion.

1.3.3. Boron nitride

BN is synthetically prepared and it is highly resistant to heat, exhibiting graphite like layer structure. Its unique characteristics make it an excellent performance enhancing solid lubricant additive, and a viable alternative to graphite and MoS₂. It possesses superior thermal stability and adherence that presents an opportunity to formulate new solid lubricants with BN for applications where conventional materials perish and fail to deliver the desired performance. It has the ability to lubricate in extreme cold or heat and is well suited to EP applications. It is environmentally benign and inert to most chemicals [71].

There are six polymorphs of BN

1. Hexagonal BN (h-BN).
2. Rhombohedral BN (r-BN)
3. Cubic BN (c-BN)
4. Wurtzite BN (w-BN).
5. Orthorhombic BN.
6. Monoclinic BN.

Amongst them, cubic and hexagonal boron nitride has engineering applications [72].

Cubic Boron Nitride (c-BN)	Hexagonal Boron Nitride (h-BN)
Alternatively bonded boron and nitrogen atoms in a tetrahedral network, exactly like carbon atoms do in diamond. So it is a 3D giant covalent lattice	The three boron and three nitrogen atoms form a hexagonal ring and all the bond lengths are found to be 0.145 nm. It is not an alternate single-double bond system.
The B-N-B or N-B-N bond angle is 109° as found in the 3D C-C network in diamond.	The B-N-B or N-B-N bond angle is 120° a perfect hexagonal network as found in graphite.
Cubic boron nitride (c-BN) is used for cutting tools and abrasive components for shaping/polishing with low carbon ferrous metals. BN based tools behave in a similar way to diamond tools but can be used on iron and low carbon alloys without risk of reaction because c-BN is chemically inert. c-BN does not lose its cutting properties until 1100-1200°C.	Possesses excellent thermal and shock stability and chemical stability; h-BN is often used as parts of high-temperature equipment (a typical melting range is 2700-3000°C). They are stable in air up to ~1000°C.

1.3.3.1. Synthesis of h-BN

It is typically synthesized from boric oxide or boric acid in the presence of urea or urea derivatives and ammonia, at temperatures ranging from 800°C to 2000°C. The mixing of sodium tetrafluoroborate (NaBF_4) and sodium azide (NaN_3) in an autoclave kept at 300°C in a furnace for 20h yielded BN hollow sphere and small amount of nanotubes. Higher percentage of spheres and tubes were produced as high as 450°C. The obtained products demonstrate excellent thermal stability along with chemical inertness. More amounts of NaN_3 and longer reaction time facilitate nanotube formation; however, this was only to a small extent [73].

Large quantities of h-BN, as high as 73.6% yield, were obtained from the reaction between urea, Na_2CO_3 and boric acid in different atmosphere; NH_3 , Ar and N_2 at temperatures between 700 and 1200°C. It was observed that addition of Na_2CO_3 to the precursor leads to increased production of h-BN with increased crystal thickness and particle size only when the atmosphere used was NH_3 [74]. In other atmosphere, such as Ar and N_2 , the amount of h-BN formed was low. The change in d values and three-dimensional ordering was observed with increased temperature and were independent of other factors such as atmosphere and Na_2CO_3 content. Boric acid and Na_2CO_3 formed a sodium borate melt from which h-BN crystallized by the reaction of borate and nitrogen ions in the melt.

Another report was found on the high yield synthesis of stoichiometric BN nanostructure from borazine vapor as a precursor using hot filament-chemical vapor deposition (HFCVD) technique [75]. The precursor without any catalytic reagent undergoes a series of dehydrogenation reactions resulting in the formation of stoichiometric quasi-spherical BN nanoparticles (20 and 50 nm). Elemental mapping revealed the BN stoichiometry and the structure was free from elemental B segregation or N deficiency. Nano fibers of diameter from 80 to 500 nanometers were observed along with quasi-spheres consisting of hexagonal and rhombohedral phases.

The synthesis of a graphene analogue of a few layer of BN was reported for the first time through a bottom-up approach. Reacting a mixture of boric acid and urea with a different molar ratio (i.e. 6, 12, 24, 48 and 72) at 900°C yielded h-BN. The obtained product showed the characteristic reflection of h-BN with d-spacing 3.51Å and it was found that with increasing ratio

of urea the d-spacing of (002) plane also increases, indicating a decrease in the number of layers [76]. The surface area was also found to increase due to less number of layers rather than the bulk area of flakes. Functionalization of the obtained product with Lewis bases (trioctylamine (TOA) and trioctylphosphine (TOP)) in toluene, heptane and benzene was also completed for the possible applications to make polymer composites.

Highly crystalline h-BN was synthesized by heating turbostratic semi-crystalline BN (t-BN) under N_2 atmosphere. The aqueous mixture of H_3BO_3 and $Na_2B_4O_7$ was spray dried and mixed with urea, followed by calcination at $900^\circ C$ for 30 minutes, which yielded t-BN. The product was further subjected to nitriding at different temperatures up to $1550^\circ C$ under N_2 atmosphere. The obtained particles were found to be irregular plate-like shapes having diameter between 0.5-1.5 μm with a thickness in the range of 50-150 nm. It was observed that h-BN was obtained at low nitriding temperature ($1400^\circ C$). In addition high-energy ball milling of t-BN followed by nitriding at $1400^\circ C$ was helpful for phase transformation from t-BN to h-BN with increased grain size [77].

A facile method was introduced for the synthesis of h-BN having different morphologies, such as fibers and flowers. The process involves the formation of an intermediate (by the reaction of potassium borohydride (KBH_4) and NH_4Cl), which on further heating at $1250^\circ C$ for 10h will give h-BN. From TGA and XRD studies it was confirmed that that no h-BN was formed at $1000^\circ C$, even after heating for longer times (up to 36h) revealing that temperature plays a crucial role in h-BN synthesis; h-BN were obtained only at a temperature of $1250^\circ C$ for 10h [78]. The precursor mixture consisting of boric acid, NaN_3 , NH_4Cl and urea was combusted in minutes to give t-BN, which on annealing at $1000^\circ C$ converted to h-BN. XRD, raman and IR characterization revealed that the obtained product was highly crystalline. On heating at $1400^\circ C$ for 6h these large thin-walled structures with an irregular arrangement grows into regular vertically-aligned nano plates [79].

The synthesis of h-BN crystallites carried out by the reaction of $NaBF_4$ and sodium amide ($NaNH_2$) in the presence of LiBr melt at $600^\circ - 700^\circ C$ for 6-24h [80]. The effect of LiBr melt was investigated on the shape and morphology of h-BN crystallization under auto-thermal conditions. The yield of spherical h-BN obtained was 83% to 94% based on initial amount of $NaBF_4$. The spherical morphology changes predominantly to 2D plates when LiBr molten salt was used for

crystallization medium. Also, the influence of temperature was realized by comparing the size and morphology of h-BN obtained in LiBr at different temperatures. At 700°C h-BN crystalline plates were stacked up giving a much thicker crystal having thickness about 200 nm to tens of micrometers, than those obtained at 600°C and 650°C [80].

Nanoflakes of h-BN were synthesized at 600°C by the reaction between H_3BO_3 , Mg and NH_4Cl powders in an autoclave for 10h. The exothermic nature of the reaction as, discerned from the Gibbs energy and enthalpy respectively, -713 and -515 KJ/mol were believed to be the main factor for the BN crystallization, Mg powder have a quasi-catalyst function in the yield of h-BN nanoflakes. The as-synthesized pure flakes had a mean of about 100 nm thickness and 600 nm width. The surface atomic ratio of B to N was 0.98 [81].

Micro and mesoporous BN with a high surface area was synthesized through the sol-gel poly condensation method. The cryogel, formed from freeze drying the mixture of resorcinol, formaldehyde and boric acid, was subjected to pyrolysis and subsequent heat treatment resulted in the formation of BN powder. Boron carbide (B_4C) was formed as an intermediate product, which on increasing the temperature from 1400°C-1500°C converts to BN under N_2 atmosphere. The pre-composite cryogels and the BN powders were porous in nature with high surface areas [82].

Hollow BN nanocages were prepared by nitriding the arc-discharge synthesized amorphous boron nanoparticles at 1073 K for 4h using N_2 and NH_3 . The growth mechanism of BN nanocages involves the reaction of nano boron with N_2 gas to form local BN layer, which along with boron nanoparticles, gives hollow BN nanocages. The obtained hollow nanocages were a highly crystalline mix of both pentagonal (200 nm) and spherical (12-20 nm) nanoparticles [83].

Needle like and hollow spherical morphology of BN was obtained by nitriding magnesium diboride (MgB_2) with NH_4Cl and a mixture of NH_4Cl and NaN_3 . These two routes show a different effect on the morphology of the product; in the presence of NH_4Cl needle like BN particles formed whereas hollow spheres of 80-120nm formed with a mixture of NaN_3 and NH_4Cl (molar ratio of 0.5) and with 1:1 ratio fine size (20nm) hollow spheres produced. This suggests that NaN_3 plays important role in the morphology and particularly on the size of BN hollow spheres. Similarly, temperature and time had some influence for both reaction routes; the

reaction was complete within 4 to 10h runtime at 500°C (550°C) for NH_4Cl and NaN_3 route (NH_4Cl route) [84].

Spongy h-BN was synthesized from the auto thermal reaction of BBr_3 (boron tribromide), NH_4Cl and aluminum powder at 500°C. Silver nanoparticles based composites with BN sponges also prepared following the same procedure, using AgCl at the same temperature. Structure and composition studies of the powders were performed using different characterization techniques such as electron diffraction, IR, XRD, TEM, and XPS. The effect of reaction conditions on the formation of sponges was investigated by varying parameters like reaction temperature and duration and it was discovered that 500°C and 10h auto thermal condition was ideal for the formation of h-BN sponges and Ag-composites [85]. Temperature and reaction time above or below this yield product of different morphologies. Silver nanoparticles loaded BN sponges may have potential use as novel catalysts for new applications.

High-pressure (22MPa) auto thermal synthesis was reported on nanocrystalline BN from KBH_4 and NH_4Cl at 650°C. The obtained BN nanowhisker was found to be a combination of c-BN and h-BN. The surface atomic ratio of B to N was 1.01:1. The influence of reaction temperature, time and amount of reactant NH_4Cl were found substantial on the BN phase purity and morphology. The formation of c-BN was prominent with increased amount of NH_4Cl that leads to increased pressure and reaction temperature higher than 600°C [86]. On the contrary, high pressure was found to be beneficial for h-BN formation at lower temperature. h-BN nanocrystals of high purity with different morphologies such as fiber, sheets and tubes, were synthesized by the reaction of boron and NaN_3 in anhydrous $\text{CH}_3\text{-CN}$ solvent at 380°C. On increasing the temperature above 400°C, sheets like h-BN crystals were obtained along with small amounts of BN nanotubes with disappearance of the fibers [87]. Nevertheless, BN phase transitions were influenced to a greater extent by pressure and temperature at which they are treated under given atmosphere, for example inert or air or H_2O ; very high pressure of 7.7 GPa and 2200°C inert conditions were required to transform amorphous BN to highly crystalline cubic form. Such amorphous BN when converted to h-BN, exhibits significant reactivity under humid conditions and thus can be transformed to c-BN in air at relatively lower pressure (5.5 GPa) and temperature (1500°C) in comparison to the one kept under dry nitrogen atmosphere [88].

Vertically aligned BNNSs were grown on Si substrate from mixture of gases ($\text{BF}_3\text{-N}_2\text{-H}_2$) in catalyst free conditions using microwave plasma chemical vapor (MPCVD). The obtained morphology and growth rate of sheets strongly depends on the chemical properties of gases (H_2 and BF_3), along with their flow rate and flow rate ratio. The procedure involves the introduction of hydrogen that balances the etching effect of the F atom leading to formation of stable HF molecule counting on the $R_{\text{H}_2}/R_{\text{BF}_3}$ (flow rate ratio), resulting in BN solid deposition. The $R_{\text{H}_2}/R_{\text{BF}_3}$ ratio controls the equilibrium between film formation and etching and thus controls the production rate of solid BN from the gas phase. In addition, the branching in sheets and its size is dependent on BF_3 flow rate (R_{BF_3}) while required flow rate (R_{H_2}) of H_2 gas is needed for the nanosheet formation. Increasing R_{H_2} at constant R_{BF_3} produces thick, coarse and more branched granular film.

The effect of different flow rates of H_2 and BF_3 on the morphology of BNNSs are shown in the Figure 1.12. The catalyst free synthesis of 2D-BN nanomaterials with controlled structure gives rise to the potential application of BNNS in UV nanoelectronics and self-cleaning coatings [89].

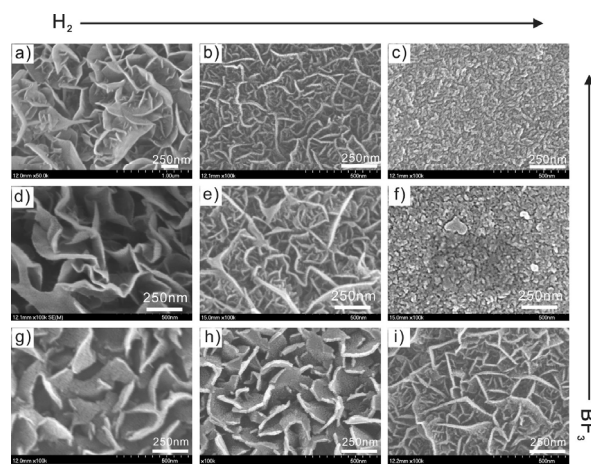


Figure1.12: SEM images of the BNNSs grown at different $R_{\text{H}_2}/R_{\text{BF}_3}$ (sccm): (a) 10/5, (b) 25/5, (c) 40/5, (d) 10/3, (e) 60/3, (f) 160/3, (g) 30/2, (h) 40/2 and (i) 100/2 [89].

The functionalization of h-BN using amine molecules would cause exfoliation of layers into several or multi-layered nanosheets. This method facilitates nanosheets of h-BN to disperse in organic solvents and/or water. Mechanism involves the complex formation between amine and boron (Lewis acid-base interactions), which allows the amine molecules to get attached between the h-BN layers and hence eased the exfoliation of nanosheets from large particles [90]. Lewis-

base interactions were studied using solution phase nuclear magnetic resonance (NMR) spectroscopy and showed a reaction mechanism of complex formation between amino groups and electron deficient boron atom on the surface of h-BNNS. Exfoliation of h-BN particles was performed using methanesulfonic acid [MSA] (protic sulfonic acid), as shown in Figure 1.13.

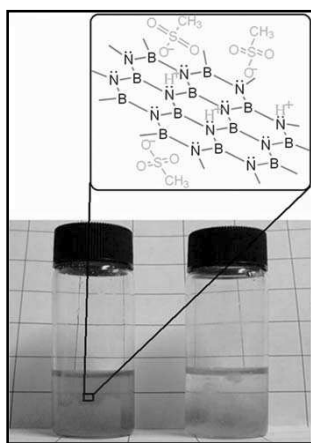


Figure 1.13: Schematic illustration of the protonation of BNNS in MSA solution (top), and dispersion of BNNS in MSA in a sealed bottle (left) and exposed to air (right) two weeks after preparation [91].

The product obtained was orange due to the charge transfer between BNNS and MSA molecules as seen in case of carbon nanotube (CNT) or graphene. Obtained BNNSs could be readily redispersed in many organic solvents (NMP, DMF and dimethyl sulfoxide (DMSO)) by sonication for several minutes, showing the ability of exfoliation state of BNNS and polarity of solvent molecules. These sheets were used for forming BNNSs based composites having poly [2, 2'-(p-oxydiphenylene)-5, 5'-bibenzimidazole](OPBI) as polymer matrix. The composites were prepared using a solution casting technique and the obtained product displays good mechanical and thermal properties [91].

A simple chemical exfoliation method to produce large size BNNSs was proposed by Du *et.al.* [92] using H₂SO₄, KMnO₄ and H₂O₂. A tentative mechanism was proposed comprising of three major steps: mixing of BN powder with H₂SO₄, which will cause the enlargement of layer spacing, followed by the addition of KMnO₄, which reacts with H₂SO₄ to form MnO₂ nanoparticles that intercalate within the layers of BN and commences exfoliation by continual restacking of sheets. H₂O₂ was used to remove MnO₂ nanoparticles with generation of oxygen

gas, which results in outward pushing force inducing the expansion of BNNSs multilayers and accomplishes the full exfoliation of sheets. This cost effective and facile method produces sheets of larger size [92].

Use of molten hydroxide for exfoliating the h-BNNSs at low temperature was demonstrated. The method turned out to be expedient and cost effective, with a single step, and easily transferable to any substrate by redispersing in common solvents. The adsorption of cations over the BN surface leads to self-curling that expands the spacing between layers near the edges and facilitates the insertion of ions. The excess of anion (OH^-) gets adsorbed first and self-curling begins, followed by cationic adsorption on the freshly exposed surface. It was predicted that the curling up sheet peels off from the parent counterpart owing to the reaction of h-BN and hydroxides. The yield obtained using the above method was about 0.19%. Atomic force microscopy (AFM) and high resolution transmission electron microscopy (HRTEM) studies indicated that exfoliated BNNSs largely comprised of aggregated and few layer crumpled sheets (less than 10). Crystalline structure of separated nanosheets was evident by six-fold symmetry of h-BN [93].

Recently, a primary research focus has been to isolate the single and multilayered products and study their unique properties. These 2D sheets are produced by exfoliation of bulk sample (graphite, MoS_2 , h-BN) and possess enhanced physical and chemical properties. Since the preparation of graphene by exfoliation using scotch tape [94, 95] was reported, the method was utilized and proved to be effective for other layered materials [96-98]. The production of BN by mechanical cleavage using scotch tape is traditional and one of the most common methods but the yield obtained is quite low [99]. Methods such as chemical solution exfoliation, chemical vapor deposition (CVD), chemical reaction, segregation method, and ball milling approach are also well known. Literature methods show good yield of more defective BNNSs, unlike the mechanical exfoliation route that yields fewer defects despite the low yield. The Ball milling method can be utilized for the synthesis of BN sheets; the milling parameters can be altered and optimized in order to produce high yield and better quality BNNSs with minimal in-plane defects in the crystal structure [100,101].

Tailored milling conditions produce high quality BNNSs. Milling was carried out in horizontal planetary mills with benzyl benzoate as the milling agent for 15 hours with steel balls. The in-plane crystal structure was retained by selecting appropriate milling conditions, such as planetary mill, which allows a rolling motion that will give shear force on the powder material. The smaller size steel balls help in reducing the damage caused to the in-plane crystal structure and lastly the milling media acts as a lubricant that prevents a welding effect by reducing damage on gently shearing. Other milling agents (water, ethanol and dodecane) tested showed increased Fe content in milled sample, however, the low reactivity of benzyl benzoate with iron and the higher viscosity helps in reducing the impact of the balls and hence only 0.26% of Fe contamination was found after 30 hr of milling with benzyl benzoate. Reduced thickness and little damage to in-plane structure was also achieved using ball milling [102].

Ball milling followed by sonication was found to be effective for high yield production of few layer h-BNNSs. Increased milling time leads to small and thin nanosheets, however, the yield was very low around 0.1 mg mL^{-1} . Multiple recycling leads to an increase in the yield of exfoliated h-BN nanosheets. Recycling involves exfoliation of the sediments obtained from a combination of low energy ball milling and short-term sonication of the starting material that may lead to increased yield up to 5 mg mL^{-1} [103].

1.3.3.2. Applications of h-BN

h-BN has several applications such as:

1. Lubricating oil additives.
2. Solid lubricant for metal forming.
3. Electrical insulator.
4. Thermal coatings for semiconductor, electronics, motor vehicles, and industrial equipments.
5. High temperature fire resistance grease.
6. For polymer based composite as an anti-friction coatings.

1.3.3.3. Tribological applications of h-BN

As mentioned earlier, h-BN is a potential candidate for solid lubricant application. Several morphologies, tubes, fibres, faceted cylinders and nanowhiskers are known from the literature reports; spherical nanoparticles (nanospheres) or nanoflakes will be useful for lubricant applications to produce rolling effect between the rubbing surfaces. The friction behaviour of h-BN nanoplates was compared between room temperature and 800°C under inert and water vapor atmosphere in pure form and mixed with CaB_2O_4 (10 wt%) as additive. The tribological testing revealed that the friction coefficient of both the sample initially increased from about 0.15 to 0.5 from room temperature to 400°C; beyond that at 800°C friction coefficient reduced marginally due to sliding effect as well as boron oxide formation. In the presence of water vapor the friction reduced dramatically to 0.38 at 400°C, which was attributed mainly to a lamella-slip and the solid lubrication effect of H_3BO_3 [104].

The effect of h-BN was demonstrated as an additive in lubricating oil for porous sliding bearings used in car clutches. h-BN powder was mixed with transformer oil and then the CoF of powder matrix was measured at various loads and pressure-velocity (PV) characteristics derived from the transition time to seizure of porous bush composites. It was found that addition of h-BN micro particles (~1-2 μm) reduces the friction two times that of neat oil. On comparing commercial lubricant Mobil DTE-BB, h-BN micro-particle added oil showed superior performance. The micro particle embedded within the porous bearings persists for long time and is released gradually during sliding to occupy the contact surface. The prospective application of BN as AW additive was also established; about 1% BN in lubricating oil found to show reduction in wear scar of rubbing surface comprising steel and cast iron. In particular, boron occupies the cast iron surface and CoF is also amply reduced [105].

A study was conducted to evaluate the effect of the addition of micron sized BN particles in grease and test for fretting sliding and vibrating tests. Same weight percent of h-BN micro particles were taken while conducting the test and it was discovered that the scar depth and width were comparable to commercial lubricant during vibrating fretting, while sliding fretting showed improvement as surface damage was three times lower compared to commercial sample. The friction coefficient was independent of sliding speed in sliding tests [106].

Other sliding experiments were conducted to verify the behaviour of BN when added to lubricating oil. Sliding of bearing steel and bearing steel vs. cast iron were examined and found that there was wear reduction in both cases whereas friction was increased in the former. Surface analysis also revealed that there were traces of boron over small cavities while the major constituent was boron oxide as B_2O_3 for steel vs. steel bearing, however, steel vs. cast iron mainly consisted of BN on wear scars demonstrating BN as a potential lubricating oil additive [107].

Stable Newtonian nanofluid with nanosheets of h-BN in mineral oil (MO) were prepared and examined for their thermal electrical properties. Nanosheets were prepared by exfoliating the h-BN powder in isopropyl alcohol and then dispersed in MO to form stable dispersion without compromising its electrically insulating properties. Effective thermal conductivities (k_{eff}) of nanofluids (NFs) increases with temperature (measurements are taken from room temperature to $50^\circ C$), indicating the role of Brownian motion on thermal conductivities measured, in accordance with Maxwell predictions. Other factors influencing the k_{eff} of NFs are the liquid layering and viscosity. Viscosity enhancement by using nano-fillers was negligible that helps to maintain effective K_{eff} . The high thermal conductivity value even at smaller filler concentrations is due to the high surface area of h-BNNSs [108].

Tribological properties of h-BN were studied using porous bush composites of different diameters infused with (h-BN and transformer oil). The effect of load on transition to seizure time for porous bearings and effect of PV on friction coefficient for bushes infused with (h-BN +oil) and Mobil DTE-BB lubricant were studied. h-BN is an effective lubricant as it lowers the transition time to seizure and also reduces the friction coefficient by forming a film over the surface on the sliding interface as h-BN particles align parallel to the direction of motion. Bench tests showed the impact of impregnation of h-BN with oil by satisfying 100,000 h of clutch operation in real engines [105].

Improved tribology was manifested by 2D atomic sheets reinforced mineral oil in the field of NFs. Multifunctional prospects of NFs (containing 2D nanosheets) are reported where a very small fraction of nanomaterials reduces the contact friction and is involved in thermal management. Thermal and tribological properties of h-BN and graphene reinforced metal

cutting lubricants were examined by studying the variation in viscosity with temperature and concentration of nanofillers.

Two different tests, ASTM standard D5183, and a polish method (from ITEePib) were performed for testing lubricants under conditions of scuffing and the results in general are in agreement with each other. The layering mechanism explained for the lubrication reduction with graphene engine oil fluid is more generalized to other layered materials based fluids such as h-BN. These multifunctional NFs maybe better candidates for various energy management fields in future [109].

Little research on the tribological properties of AISI 4140 steel with an engine oil additive that includes nano h-BN nanoparticles has been reported. The amount of nano h-BN in the engine oil varied from 0 to 10% by volume, and four different lubricant samples were prepared to study the effect of nanoparticles on friction and wear properties. Varying the concentration of h-BN nanoparticles does not change the viscosity of lubricants however; they displayed differences in CoF and wear results. Inadequate amount of nanoparticles in one sample leads to increased friction and wear. Other samples containing appropriate amount of nanoparticles exhibited 65% less wear as compared to neat sample containing no additive.

Nanoparticles completely covered the asperities therefore, the mending effect occurred in these samples, and they exhibited the lowest wear rate and the wear-track widths among the samples. The surface roughness values found from the samples supported these results. The presence of sufficient amount of nano h-BN additives in oil prevents direct contact and results in a decrease in friction and wear. This study represents a step toward a fundamental understanding of the friction and wear properties of nano h-BN [110].

The reported literature demonstrates various techniques for the production of h-BNNSs that involves chemical synthesis route, liquid exfoliation and ball milling procedure. However, the yield obtained was not satisfactory because of poorly optimized reaction/ milling conditions. Most importantly, the tribological applications of h-BNNSs were not evaluated.

2. Experimental method and characterization techniques

This chapter gives a brief overview of the experimental method used for the preparation of nanomaterials and the analytical techniques exploited for their characterization and testing. Nanoparticles prepared by the methods described in the thesis have been characterized by spectroscopic techniques such as confocal dispersive raman and microscopic techniques such as TEM, SEM and other standard material characterization techniques such as XRD measurements, TGA and particle size analysis (by dynamic light scattering (DLS)). This chapter details the instrumentation and physical principals behind these analytical techniques.

2.1 Experimental method

2.1.1. Ball milling

Ball milling is defined as a process in which the mechanical breakdown of solids into smaller particles will occur without any change in their state of aggregation [Bernotat and Schonert 1998]. Particles of indefinite shape and sizes (micron and sub micron domain) can be produced using this approach; as well as there will be induced defects into the solid structure that would increase the surface area of the material. The increase in surface area is accompanied by increasing proportions of high active surfaces due to the induced defects. This method is also known as mechano-chemical method, which is widely used for the synthesis of nanoparticles and nanocomposites. However, controlled size reduction through this route is somewhat tedious [111]. Process involves subjecting the powder sample along with balls (ceramic/steel/glass) into a milling vial and the sample particle encounters the impact of balls colliding with each other and with walls of vial. The process is typically used for decreasing the size of the particles and hence termed as top-down approach.

Following the advancement of this technology, more sophisticated ball milling machines capable of accelerating balls up to high speeds (large kinetic energy) have been developed. High-energy ball milling that is achieved by grinding with balls of large kinetic energy appears to be capable of structural modification and creating a number of interesting phases. A list of phases achieved

by ball milling includes nanocrystalline materials, quasi-crystals, supersaturated solutions and other non-equilibrium materials. In addition, the ball milling technique is capable of inducing chemical reactions that do not normally happen at room temperature (the phenomenon referred generally to as mechano-chemical or reactive ball milling). A more detailed overview of the ball milling technique can be found in several reports [112-114].

A number of ball milling devices (shaker mills, attritors, planetary ball mills, and vibratory ball mills) have been designed for processing and inducing structural transformations of powders and new phases.

A planetary ball mill has been used in the current study. The schematic of ball mill is shown in Figure 2.1.

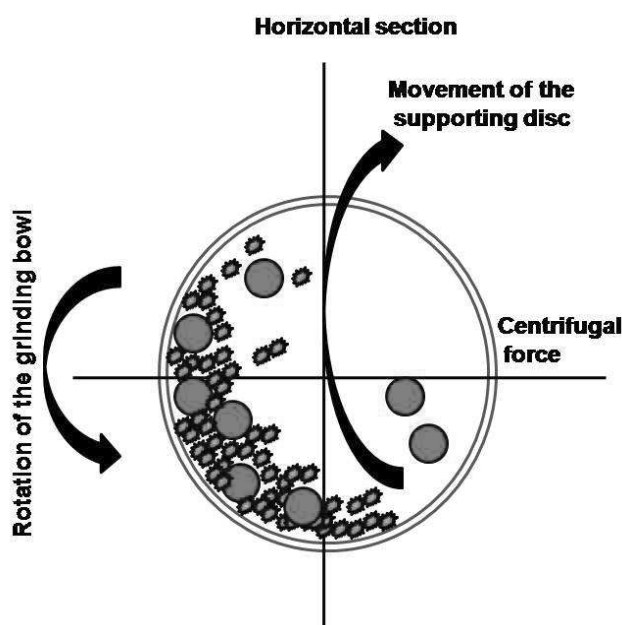


Figure 2.1: Movements of working parts and balls in a planetary mill [111].

It works on the principle of centrifugal acceleration where vials and supporting disc rotate in opposite directions; the centrifugal forces alternatively act in like and opposite directions [Suryanarayana 2001, Golosov 1971; Molčanov et al. 1988]. The charge inside the vials performs two relative motions; a rotary motion around the mill axis and a planetary motion around the vial axis [111]. Wet ball method was performed to produce nanoparticles as it is beneficial over dry milling process in which a powder sample was ball milled with milling balls, which causes lots of damage to the vial walls, leads to contamination by ball wearing and

particle agglomeration. However, during wet milling such encounters are very rare if the milling parameters are properly optimized.

Two different planetary mills were used in this study:

1. Retsch PM-400MA planetary ball mill with ZrO_2 (stabilized zirconia) having a volume of about 500 ml are used at rotation speeds in the range of 1000-1200 rpm and grinding balls (zirconia) of size 1mm, 0.5mm and 0.1mm ϕ are placed inside the vials along with the sample and milling medium for milling at desired speed and duration.
2. Pulverisette 7, Fritsch horizontal planetary ball mill with steel having a vial volume of 75ml used at 600-1000 rpm and grinding balls (steel and Zr_2SiO_4) of 1.0 mm ϕ (steel), 0.6-0.8 mm and 0.1-0.2mm ϕ (both Zr_2SiO_4) placed inside the vials along with the sample and milling medium for milling at desired speed and duration.

2.2. Characterization techniques

2.2.1. Particle size analysis

DLS is used to find out the particle size by analyzing the Brownian motion (random movement of particles in a liquid due to the bombardment by the molecules surrounding them) of suspended particles. The size of the particle is determined from the arbitrary motion and the speed of the particles in liquid medium. Hence, this technique employs a source of light (laser) to trace the particle path and then the scattered light is collected at the detector positioned at a fixed scattering angle. Scattering intensity for the particles moving under the Brownian motion will vary along with time. Across long time intervals, the intensity trace will appear to be representative of random fluctuations about a mean value. When viewed on a much smaller time scale, however, it becomes evident that the intensity trace is in fact not random but rather composed of a series of continuous data points. Smaller particles show quick movement in contrast with larger molecules. By keeping a watch on the particle movement the particle size can be obtained, if there is minimal movement and the particle position are similar, then the particle in the sample is large; likewise if prominent amount of movement and position of particle are quite dissimilar then smaller size of particle are obtained [115].

Data obtained through experiments is the correlation curve formed due to the constant random Brownian motion of particles in dispersion, which causes fluctuation in the intensity of scattered light. Correlation function is thus used to obtain size distribution and correlation function (G) of scattered intensity is given as:

$$G(\tau) = \langle I(t) \cdot I(t+\tau) \rangle$$

Where, τ = the time difference (the sample time) of the correlator.

In the current study particle size analysis is performed with Malvern Zetasizer (Nano-ZS) dynamic light scattering equipment dispersing the sample (CaCO_3 and MOS_2) in base oil after processing in the mill. The equipment operation is based on photon correlation spectroscopy, which examines the diffusion rate of suspended particles utilizing a backscatter angle of 173 degree. The equipment uses 5 mW He-Ne laser of wavelength 633 nm.

2.2.2 X-ray diffraction

XRD is used for the phase identification of crystalline materials. It provides information about the crystal structure and atomic spacing. It is based on the principle of constructive interference of monochromatic x-rays and the crystalline powder sample.

X-ray diffraction occurs in the elastic scattering of x-ray photons by atoms from the periodic lattice. The scattered monochromatic x-rays that are '*in-phase*' give constructive interference. If the distance between two periodic lattice planes is '*d*' and the angle between the incoming x-rays and the normal to the reflecting lattice plane is ' θ ' then Bragg's equation [116] is

$$n\lambda = 2d \sin\theta ; n = 1, 2, 3, \dots \quad (2.1)$$

where, λ is the wavelength of the x-rays and n is an integer called the order of the reflection. By measuring the angle, 2θ , under which constructively interfering x-rays leave the crystal, the Bragg's equation (2.1) gives the corresponding lattice spacing, which is characteristic for a particular compound.

Width of diffraction peaks signifies the dimension of the reflecting planes. Diffraction lines from the perfect crystals are very narrow. For crystals with size below five nm, peak broadening occurs due to incomplete and somewhat destructive interference in scattering directions where the x-rays are '*out of phase*'. The Scherer formula (equation 2.2) [117] relates crystal size to line width:

$$\langle L \rangle = \frac{K\lambda}{\beta \cos\theta} \quad (2.2)$$

where $\langle L \rangle$ is a measure of the dimension of the crystal in the direction perpendicular to the reflecting plane, λ is the x-ray wavelength, β is the full width at half maximum (FWHM) of the peak, θ is the angle between the beam and the normal to the reflecting plane and K is a constant (often taken as 1).

XRD studies are carried out at two different instruments:

- I. An 18 KW X-Ray Diffractometer (Rigaku, Japan) having a copper rotating anode was used. For analysis powder sample was grinded and spread on the sample holders. The patterns are recorded at 50 KV and 250 mA,
 - (i) from 5-75° at a scan rate of 2 deg / min with a step size of 0.01 deg for pristine CaCO₃ and milled samples.
 - (ii) from 0.5-10° at a scan rate of 0.5 deg / min with a step size of 0.01 deg for pristine CaCO₃ and milled samples.
 - (iii) from 5-50° at scan rate of 1 deg / min with a step size of 0.01 deg for pristine MoS₂, MoO₃ and milled samples.
- II. A Pan-analytical Xpert Pro equipped with a copper anode was used. For analysis, samples were prepared by displacing over the glass substrate directly taken from the milling vial (without sonication and centrifugation). The patterns are recorded,
 - (i) from 10-110° at a scan rate of 6.25 deg / min with a step size of 0.1 deg for pristine h-BN and milled samples.

The patterns were processed and peak search was conducted by search match to determine different phases present in the samples.

2.2.3. Electron Microscopy

Although some structural features can be revealed by x-ray diffraction, direct imaging of nanoparticles is only possible using transmission and scanning electron microscopes. Both are operating on the same basic principles as the light microscope but uses electrons instead of light [118].

The development of the transmission and scanning electron microscope in the late 1930's and early 1950's respectively primarily as an imaging devices, which exceeded the resolution power of the light microscope, by several orders of magnitude. Since the *de broglie* wavelength of electrons decreases with their increasing kinetic energies, fast moving electrons have very short wavelength associated with them and so are capable of very high resolution if that wavelength can be used in an appropriately designed instrument.

Resolving power of a microscope is given by the following formula:

$$d = 0.5 \lambda / \sin \alpha$$

where, λ represent the wavelength and α equals the one-half of the angular aperture. Since the wavelength of electrons is in the range of a few angstroms, in principle, the resolution of electron microscope could go up to a few angstroms. In both SEM and TEM, the system is composed of an electron gun that has a hot wire filament and a wehnelt shield. The electron beam comes from a source (filament), made of various types of materials. The most common is the tungsten hairpin gun. A small electric current heats the source. This produces a thermionic emission of electrons, which essentially is a cloud of electrons that form around any hot metal. The filament and shield called the cathode are then set to a very high electric potential between 25KV to 125KV. This gives the electrons in the cloud the incentive to move. As the filament heat is turn up the electron cloud forms, and all the electrons are accelerated towards the grounded anode if not for the bias shield. Surplus electrons collected onto the shield making the shield more negative, which in turn inhibits the release of more electrons. This is called self-biasing and is controlled by the bias resistor.

2.2.3.1. Transmission electron microscopy (TEM)

TEM is a microscopy technique in which an electron beam is transmitted through and interacts with the sample, leading to the formation of an image due to the interaction of the transmitted electrons. A beam of accelerated electrons can interact with an object in a conventional TEM in one of two ways [119]. Usually, elastic scattering takes place whereby the electrons change their path in the specimen without a loss of energy. Inelastic scattering can also occur, resulting in a loss of energy due to an interaction of the impinging electrons with the orbital electrons surrounding the nucleus of each atom in the object. Those electrons, which are not or hardly scatter, contribute positively to the image. Those that are considerably deflected are prevented

from doing so by apertures in the optical path. As a result, differences in light intensity (contrast) are created in the final image, which relate to areas in the object with different scattering potentials.

This fact can be deduced from the following formula of Rutherford, which describes the deflection potential of an atom:

$$K = \frac{-e.eZ}{r^2}$$

where, K is deflection potential, e= electron charge, z= positive charge and r =distance from electron to nucleus. As the atomic number increases, their scattering efficiency will also increase. Hence, heavy metals can form images with good contrast. The imaging system consists of an objective lens and one or more projector lenses. The chief lens in transmission microscopes is the objective. It determines the degree of resolution in the image. It forms the initial enlarged image of the illuminated portion of the specimen in a plane that is suitable for further enlargement by the projector lens. The projector lens, as it implies, serves to project the final magnified image on the screen or photographic emulsion. The great depth of focus provides the high magnification of the sample.

TEM measurements were carried out on Jeol (JEM 2100) instrument at 200KV having LaB6 filament with a point resolution of 0.194nm and lattice resolution of 0.14nm. For analysis, samples (CaCO₃ and MOS₂ based) were prepared by dispersing the powder sample in heptane by ultrasonication for 5 minutes. A drop of prepared sample was poured on a mesh type copper grid placed on filter paper and kept for drying.

For h-BNNSs analysis, studies were performed using a JEOL 2100F operated at 200KV under both TEM and scanning transmission electron microscope (STEM) modes.

2.2.3.2. Scanning electron microscopy(SEM)

SEM uses a focused electron beam to scan the sample surface and produce an image, which involves the electron interacting with the surface atoms in the sample producing signals that are detected to give sample's surface morphology and chemical composition.

The scanning electron microscope is able to provide images of three-dimensional objects because, in its normal mode of operation, it records not the electrons passing thorough the

specimen (as in TEM) but the secondary electrons released from the sample surface by the electron beam impinging on it [120]. The sample can therefore be of any size and thickness that will fit in the instruments evacuated sample chamber kept under vacuum. The secondary electrons do not have to be focused but are simply collected.

The broad magnification range of the scanning electron microscope, together with the ease of changing magnification, makes it easy to zoom from a gross image of the object to an image showing fine details. The images created without light waves are rendered black and white. The electron beam travels downward through a series of magnetic lenses designed to focus the electrons to a very fine spot. Near the bottom, a set of scanning coils moves the focused beam back and forth across the specimen, row by row. As the electron beam hits each spot on the sample, secondary electrons are generated from its surface. A detector counts these electrons and sends the signals to an amplifier. The final image is built from the number of electrons emitted from each spot on the sample. Detectors collect the secondary or backscattered electrons, and convert them to a signal that is sent to a viewing screen to produce an image. When the electron beam strikes the sample, some of the electrons will interact with the nucleus of the atom. The negatively charged electron will be attracted to the positive nucleus but if the angle is just right instead of being captured by the gravitational pull of the nucleus it will circle the nucleus and come back out of the sample without slowing down. These electrons are called backscattered electrons because they come back out of the sample. Because they are moving so fast, they travel in straight lines. In order to form an image with backscattered electrons, a detector is placed in their way. When they hit the detector a signal is produced that is used to form the image. Also, beam electrons interact with the electrons present in the atom rather than the nucleus. Since all electrons are negatively charged, the beam electrons will repel the electrons present in the sample. This interaction causes the beam electrons to slow down as it repels the specimen electrons, the repulsion may be so great that the specimen electrons are pushed out of the atom, and exit the surface of the sample, these are called secondary electrons. Unlike the backscattered electrons, the secondary electrons are moving very slowly when they leave the sample. Since they are moving so slowly, and are negatively charged, they can be attracted to a detector, which has a positive charge on it. This attraction force allows you to pull in electrons from a wide area and from around corners. The ability to pull in electrons from around corners is what gives secondary electron images a three-dimensional look.

To produce an image on the screen, the electron beam scans over the area to be magnified and transfers this image to the screen. The points of information are the product of number of points and lines an electron beam scans across horizontally and vertically. The signal read from the electrons coming off each point is transferred to a corresponding point on the screen [121]. Since the screen also has same points and lines across horizontally and vertically, there is a correspondence between the scan on the specimen and the screen. Since the length of the electron beam scan on the specimen is smaller than the length of the screen, a magnification is produced equal to the following equation:

$$\text{Magnification} = \text{Length of screen} / \text{Length of electron beam scan}$$

By changing the size of the scan on the sample, the magnification can be changed. The smaller the area of the electron beam scans, the higher the magnification.

Here, the SEM analysis was conducted on Hitachi S-3400N equipped with a tungsten filament. Samples (steel balls after tribology tests) were recorded at accelerating voltage of 15KV, emission current of 75mA, and working distance 14200 um under vacuum.

Few samples (h-BN nanosheets) were recorded under Zeiss supra 55VP scanning electron microscopes operated at 3 KV.

2.2.4. Thermo gravimetric analysis

Thermal analysis includes a group of techniques in which a physical property of a substance is measured as a function of temperature, while the substance is subjected to a controlled temperature program. Thermogravimetry provides a quantitative measurement of any weight change associated with a transition [122]. The composition and purity of the sample can be determined by using TGA by taking the known mass of the substance and heating it to a certain temperature so that some of the constituents decompose into gas. It is also used to determine the percentage by mass ratio of solute by taking in to account the heat utilized and stoichiometry ratio. Percentage by mass for known compounds can be estimated when the weight of substance left after heating is divided by the initial mass taken. Also, knowing the mass of the original mixture and the total mass of impurities liberating upon heating, the stoichiometric ratio can be used to calculate the percent mass of the substance in a sample.

In this study, the thermal stability and phase transitions of the samples were measured using TGA model 2960 thermal analyzing machine (TA Instruments, USA) under a flow of air. Nearly

5-10 mg of the sample (pristine and milled CaCO₃) were taken in the platinum pan and heated in air at the heating rate of 10 deg / min, up to 900°C.

2.2.5. Small angle x-ray scattering

Very low angles (0.1-10°) elastic scattering of the x-rays (wavelength 0.1-0.2 nm) by a sample in nm range is measured in SAXS. This angular range is of significance as it is characteristics of partially ordered materials and their shape and sizes. It is very powerful tool and widely used to study the form of particulate system like colloids and proteins, inhomogeneous structure like polymers and composites and layered materials. This is also a non-destructive method like XRD, in which x-ray scattering intensity versus scattering angle or scattering vector is recorded. If 'θ' is scattering angle for an incident x-ray of wavelength 'λ' then scattering vector (q) is given as:

$$q = \frac{4\pi \sin\theta}{\lambda}$$

For layered structure, the scattering vector appears at equi-distant as series of reflections (q₁, q₂, q₃,...) then the distance between the two layers 'd' is given as:

$$d = \frac{2\pi}{q}$$

For coated samples, the first reflection (q₁) can be considered in order to calculate the coating thickness.

SAXS measurements were carried out by dispersing the prepared particles in heptane in Anton Paar SAXSess mc² equipment. The equipment has a 40 KV x-ray generator emitting Cu Kα line. Imaging plate and 1D diode array detector has been used. The samples were taken in quartz capillary dispersing in xylene. In order to determine the scattering signal of the sample (milled CaCO₃) measurements are done in duplicate. After transmission correction, the x-axis was converted into scattering vectors (q) and the background measurement was subtracted from the sample measurement [123].

2.2.6. Contact angle measurement

This is an angle formed by liquid/vapour at the interference with solid. Different contact angle value represents different information such as: low values of contact angle indicates that the particle wets well while high value for contact angle shows poor wetting of the solid surface.

Full wetting of the surface indicates that it has zero contact angle. An angle less than 90 degrees implies the solid is well wet by the liquid, while a value higher than 90 degrees means low wetting. Generally, if the water contact angle is smaller than 90°, the solid surface is considered hydrophilic and, if angle is larger than 90°, the solid surface is considered hydrophobic. This technique helps in quantitatively measuring the wetting of a solid by the liquid surface.

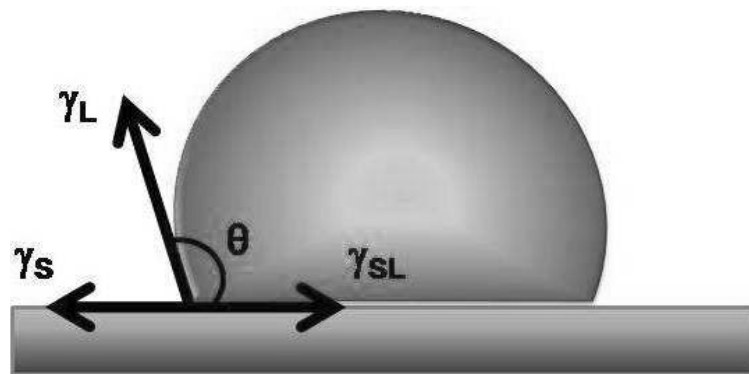


Figure 2.2: Schematic of contact angle measurement [124].

γ_ssolid surface tension

γ_Lliquid surface tension

γ_{SL}A solid and liquid boundary tension

$$\gamma_s = \gamma_L \cdot \cos \theta + \gamma_{SL} \quad (2.3)$$

This equation 2.3 is referred to as "Young's equation", and the angle θ formed by the solid surface and the tangent of the droplet is called a "contact angle". The contact angle is very easy to understand as an indicator of wettability, and has been adopted widely in industrial fields as an evaluation method of surfaces, as shown in Figure 2.2 [124].

Contact angle measurement was performed on OCA 15 plus goniometer from Data physics. This instrument can measure wetting behavior of solid surfaces by sessile drop method and can give video based measurement of static and dynamic contact angle. The measurement was obtained by taking a thin pellet prepared from powdered samples (milled CaCO_3) (1g) under 10 MPa pressure and dropping a water droplet onto the pellet.

2.2.7. Raman spectroscopy

The Raman phenomenon is a consequence of sample illumination with a monochromatic photon beam (laser), most of which are absorbed, reflected, or transmitted by the sample. However, a small fraction of photons interact with the sample. During this interaction, some energy is transmitted to elementary particles of which materials are constituted (electrons, ions). This causes their transition from ground energy levels to ‘virtual’ excited states. These excited states are highly unstable and decay instantaneously to the ground state by one of the following three different processes:

- Rayleigh scattering: the emission of a photon of the same energy allows the molecule to relax to its ground vibrational state (elastic scattering). Rayleigh scattering, therefore, bears no information on vibrational energy levels of the sample.
- Stokes and anti-stokes raman photons (inelastic scattering): emission of a photon with energy either below or above that of Rayleigh photons, thereby generating a set of frequency-shifted ‘Raman’ photons. The energy differences of the stokes and anti-stokes raman photons with respect to the excitation energy give information about molecular vibrational levels (Figure 2.3).

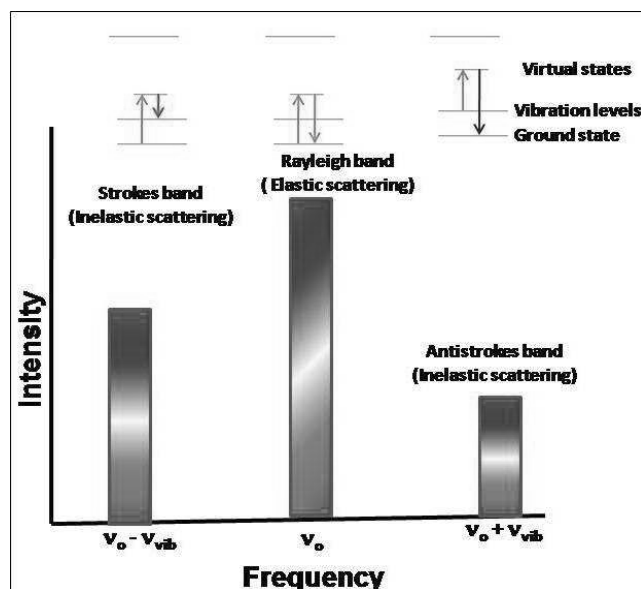


Figure 2.3: Spectrum of photon transition from elemental ground level to virtual states [125].

These photons are collected by a detector and transformed to electrical signals and finally to the corresponding raman spectrum. Usually, stokes bands which are more intense than anti-stokes

bands are called “Raman spectrum” of the sample. The Rayleigh band is filtered out before the detector [125].

Raman technology utilizes two techniques for spectra collection which involves dispersive raman and fourier transform raman.

Dispersive raman is a powerful spectroscopy as it helps in separating the collected raman scattered light into individual wavelengths by focusing the raman signal on grating that helps in separating the different wavelengths. For radiation only visible laser having shorter wavelength are used as it helps in enhancement of raman signal. Dispersive raman is often powerful for analyzing very dark samples, such as carbon black loaded or highly colored samples. Many other techniques suffer from total absorbance or sample heating, which is often not present when using the dispersive raman technique, owing to lower laser powers that can be used.

Raman analysis of wear track (steel balls after tribology tests), MoS₂ (pristine and milled), MoO₃, calcium stearate, SA, pristine and milled CaCO₃ was performed on STR 750 Confocal Dispersive Micro Raman Spectrometer equipped with 514.5 nm Ar laser (70mW) and Princeton Instruments Acton SP2750 Spectrograph having 1.4 cm⁻¹ dispersive pixel resolution. Raman stroke shift between 150 and 1000 cm⁻¹ for wear track and MOS₂ based samples and between 200 and 1700 cm⁻¹ for CaCO₃ based samples were recorded from 20 scan acquisition of 10 seconds laser excited area.

2.2.8. Surface area determination by BET method

The BET (Brunauer-Emmett-Teller) method is the most widely employed procedure to determine the surface area of the solid materials. By using the BET equation (2.4):

$$\frac{P}{V_a(P_0 - P)} = \frac{1}{V_0\chi} + \frac{(\chi - 1)}{\chi V_0} \frac{P}{P_0} \equiv \eta + \alpha \frac{P}{P_0} \quad (2.4)$$

where, P = adsorption equilibrium pressure, P₀ = standard vapor pressure of the adsorbate, V_a = volume at STP occupied by molecules adsorbed at pressure P, V₀ = volume of adsorbate required for a monolayer coverage, χ = constant related to heat of adsorption.

Plotting $P/[V_a(P-P_0)]$ versus P/P_0 yields a straight line with a slope $\alpha = (\chi - 1)/\chi V_0$, crossing the y-axis at $\eta = 1/\chi V_0$. The volume adsorbed in the first monolayer is found as $V_0 = 1/(\alpha + \eta)$. The volume V_0 can be converted into the number of molecules adsorbed by $N_0 = PV_0/RT$ and if we know the area occupied by each molecule (A_0) then the total area, $A = N_0 A_0$, can be found. For N_2 molecule $A_0 = 0.16 \text{ nm}^2$

To differentiate the adsorption mechanism between micropore and to that in meso and macropores, the t-plot analysis was developed by Lippens and de Boer and the same was applied [126]. The method consists of plotting the adsorption isotherm in terms of the volume of the adsorbate versus the statistical film thickness, t . The pore size distribution is obtained from the analysis of the desorption isotherms by applying the BJH model [127] which involves the area of the pore walls and uses the Kelvin equation to correlate the partial pressure of nitrogen in equilibrium with the porous solid to the size of the pores where the capillary condensation takes place.

BET surface area of the nanoparticles was determined by N_2 adsorption method at liquid N_2 temperature (77 K) using Quantachrome iQ2 adsorption unit. About 200 mg of sample (pristine and milled CaCO_3) was degassed at 313 K for 2 hours until the residual pressure was $< 10^{-3}$ Torr. The isotherms were analyzed in a conventional 11 point BET method in the region of relative pressure $P/P_0 = 0.05$ to 0.35 with the assumption for the nitrogen molecular area in an adsorbed monolayer is 0.16 nm^2 .

2.2.9. Tribological evaluation

Tribological properties such as wear scar, weld load and CoF, between the two rubbing surfaces are most important studies to benchmark the performance of lubricants. The relative wear preventing properties of lubricating fluids and greases in sliding and rolling applications are determined in different tribological evaluation mentioned above. For wear scar analysis, three 9mm ϕ steel balls are clamped together and covered with the test lubricant. A fourth 9mm ϕ steel ball is pressed into the cavity formed by the three clamped balls for three point contact, and rotated for a set duration. Lubricants are compared using the average size of the scar diameters worn on the three lower clamped balls. AW properties of the grease was examined using four

ball wear tester (Falex friction and wear test machine) as shown in Figure 2.4(a) by following the ASTM standard D4172 at 75°C; 45kg weight load for 60 minutes.

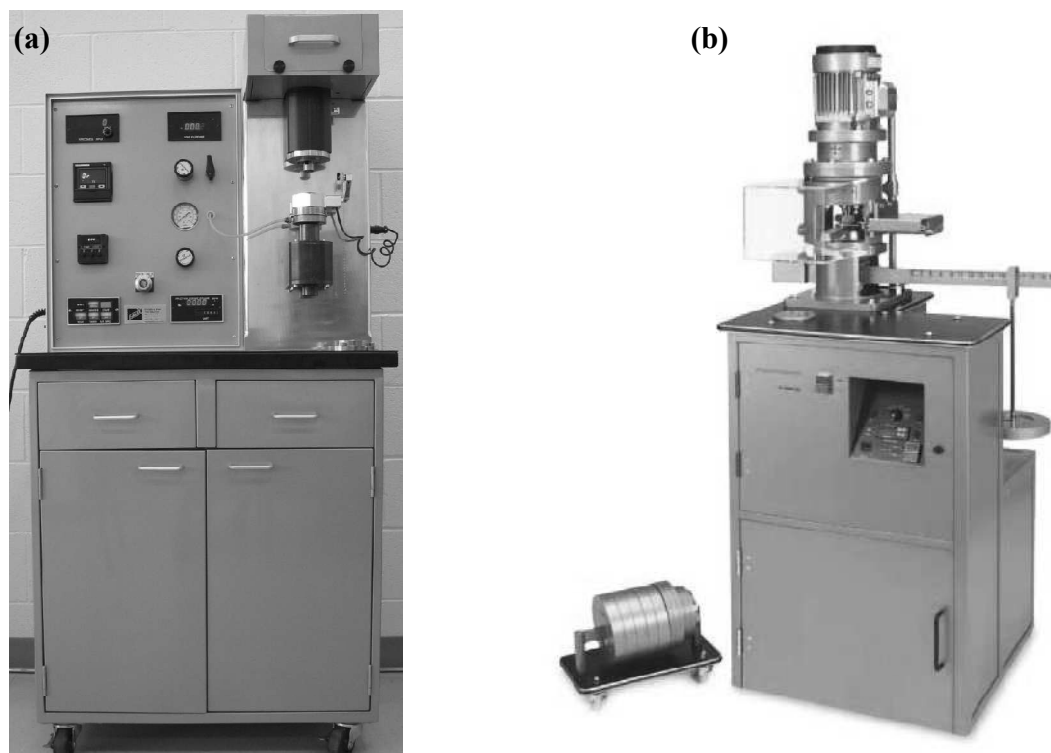


Figure 2.4: Photograph of (a) The Falex Four Ball Wear Test Machine and (b) Seta-Shell 4 Ball Lubricant Tester

For load carrying capability of oils and greases, four-ball extreme pressure lubricant tester is used. A ball, mounted in a chuck, is rotated against three stationary balls in a pot containing the sample lubricant. A load, adjustable in the range of 40 to 800kg, is applied to the balls via a balance beam and electric jack, followed by the torque transferred between the rotating and stationary balls which is measured and displayed in the digital timer, with a range of 0.1 second to 9999 hours, can be used to control the duration of the test if the torque exceeds a preset level, or the balls weld during a test power to the drive motor is automatically turned off. The torque or load applied is the measure of weld load (EP characteristics) of the sample. The EP characteristics of the lithium grease with or without MoS₂ additives were evaluated using a Seta-Shell four-ball EP tester (Stanhope-Seta, Chertsey, UK) as shown in Figure 2.4(b). The Weld Point-P_b, Kg is reported for all the samples by using IP 239 method. All the experiments

were carried out at room temperature. All the above measurements were performed in triplicate and best were taken for evaluation.



Figure 2.5: Photograph of Optimol SRV

Anti-friction or friction-reduction was examined using an Optimol SRV oscillating friction shown in Figure 2.5 by following DIN 5706. Test involves two test specimens (e.g. a ball and disk) installed in the test chamber and pressed together with a specified normal force. The top specimen oscillates on the bottom specimen. The basic configuration includes specimen holders for point, line or area contact. Frequency, stroke, test load, test temperature and test duration are pre-set. Friction force is continually measured by a sensor. The friction coefficient is automatically calculated and recorded during the entire test duration. For analysis, basic parameters involved are normal force: 1-2000 N, stroke: 0.1-5 mm (50 Hz), frequency: 1-511 Hz, temperature: ambient to +350° C, test duration: 1min-999h. All the tests were carried out with test conditions: 50°C for 50N, 200N and 300N for duration of 60 minutes [128].

Wet milling of CaCO_3 with different capping agents to produce hydrophobic core shell nanostructure.**3.1. Introduction**

Overbasing is the most important application of CaCO_3 in lubricant formulation. This can be achieved by taking advantage of the excellent dispersant properties of the long chain sulfonate molecule. Excess base in the form of calcium carbonate can be dispersed in micellers to produce so-called overbased sulfonates (refer to Figure. 1.7). Thus, surface modification by surfactants enables to disperse and/or stabilize CaCO_3 in the oil medium to be used for overbasing application. Several studies have been performed on the surface modification of CaCO_3 nanoparticles [2-9, 42].

Most of the synthesis routes involve direct carbonation and mineralization of CaO or Ca(OH)_2 in the presence of surfactant like fatty acids and solvent medium such as water or alcohol. The process mimics the crystallization of CaCO_3 within living system and hence often termed as bio-mimetic synthesis or bio-mineralization of CaCO_3 . Solution and carbonation routes were employed by many researchers for the synthesis of hydrophobic CaCO_3 nanoparticles. Hydrophobic CaCO_3 crystals are obtained through carbonation route from Ca(OH)_2 slurry under CO_2 purging at desired temperature in the presence of different surface modifiers such as fatty acids [4,7,18,19], ODP [3,29], Na-SA, terpineol [24], DA [25,26] [30-33,129]. There are reports that have mentioned carbonation process assisted by ultrasonication, in which by optimizing the synthesis parameters they had obtained desired particle size [130].

In contrast to the above mentioned soft chemical approach, ball milling technique also termed as mechano-chemical approach has been employed to synthesize hydrophobic CaCO_3 . It is a widely used method for the synthesis of nanoparticles and nanocomposites; in which the mechanical breakdown of solids into smaller particles (macro to micro or micro to nano or sub micro particles) occurs [38]. Generally, the surface area of the solids would increase due to the induced particle size during milling. The size reduction through this method depends upon various milling parameters affecting the process. These factors are material of milling media, ball to solid weight ratio, filling volume of milling chamber, milling atmosphere, milling speed and time. In mechano-chemical approach the newly created surface of the small particles *in situ*

modified by the surfactant molecules to make them hydrophobic. This small molecule surface modification continues until the creation of new surface ceases due to the limitation of the milling parameters and process conditions. The particle size reduction is not as easy as that of controlling these milling factors. The desired size reduction could be achieved by following optimized milling parameters.

Particle size reduction and *in situ* surface modification through mechano-chemical bonding of PCC nanoparticles with modifiers and the product application in overbasing has not been reported in the scientific literature.

In this chapter, hydrophobically surface modified core shell type CaCO_3 nanoparticles production, where shell is the organic-inorganic hybrid structure by ball milling route and characterized by relevant physicochemical techniques is reported.

3.2. Experimental work

As discussed in chapter 2 section 2.1.1. planetary ball mill was used for synthesizing hydrophobically modified core shell CaCO_3 nanoparticles using different dispersants, such as long chain fatty acids, succinic anhydrides and amines.

Figure 3.1 shows the molecular structure of different dispersants.

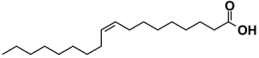
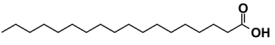
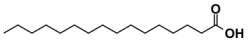
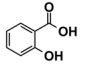
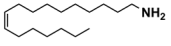
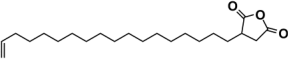
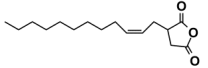
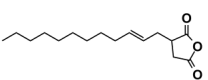
CAPPING AGENT	STRUCTURE	MOLECULAR WEIGHT
Oleic acid $\text{C}_{17}\text{H}_{33}\text{COOH}$		282.46
Stearic acid $\text{C}_{17}\text{H}_{35}\text{COOH}$		284.48
Palmitic acid $\text{C}_{15}\text{H}_{31}\text{COOH}$		256.43
Salicylic acid $\text{C}_7\text{H}_6\text{O}_3$		138.12
Oleyl amine $\text{C}_{18}\text{H}_{37}\text{N}$		267.50
ODSA $\text{C}_{22}\text{H}_{38}\text{O}_3$ Octadecenyl succinic anhydride		350.54
TPSA $\text{C}_{18}\text{H}_{28}\text{O}_3$ Tetrapropenyl succinic anhydride		266.42
DDSA $\text{C}_{18}\text{H}_{28}\text{O}_3$ Dodecenyl succinic anhydride		266.38

Figure 3.1: Detailed molecular structures of the dispersants used.

To begin 1:1 molar ratio of CaCO_3 and selected dispersant dissolved in suitable medium was taken in ZrO_2 milling vial along with ZrO_2 milling balls. The milling time and milling speed for different ball sizes (1, 0.5 and 0.1mm ϕ) were fixed for 2 hours and 1200rpm respectively.

The details of the milling process parameters are given in Table 3.1.

Table 3.1: Details of the milling process parameters.

1.	Mole ratio of CaCO_3 and selected dispersant	1:1
2.	Medium suitable for capping agent	Three times of sample dosage.
3.	Volume of ZrO_2 balls (1mm, 0.5 mm and 0.1mm ϕ).	1/3 of vessel volume (500ml).
4.	Rotating speed	1200rpm
5.	Milling time	2 hr

After milling, the milled samples were rinsed and washed several times with suitable solvent so as to remove excess dispersant followed by centrifugation and drying.

The samples are described in Table 3.2 with six letters, in which first three refer to capping agent and CaCO_3 (C) while the last three are milling medium hexane (hex), methanol (met) and xylene (xyl).

Table 3.2: Description for samples.

S.No.	Sample description	Capping agent	Medium
1.	OACHex	Oleic acid	Hexane
2.	SACHex	Stearic acid	Hexane
3.	PACHex	Palmitic acid	Hexane
4.	SCCmet	Salicylic acid	Methanol
5.	OLCmet	Oleylamine	Methanol
6.	ODCmet	ODSA	Methanol
7.	TPCmet	TPSA	Methanol
8.	DDCxyl	DDSA	Xylene

3.3. Effect of milling on CaCO_3 with different dispersants

The experiments were carried out to investigate the effect of different dispersants on the shape, size and surface characteristics of the CaCO_3 after milling treatment.

XRD analysis of milled samples helps in discovering the polymorph form of CaCO_3 , change in crystallite size and confirms the coating over CaCO_3 surface when scanned over low angles.

The XRD patterns in Figure. 3.2 show that the products obtained after milling with different capping agents were typically calcite in nature despite of their different morphologies and sizes; Figure 3.3 (a, b) shows the low angle diffraction of representative samples (SACHex and OACHex). The distinct patterns observed are matching well with calcium stearate and calcium oleate reflections (JCPDS File).

CaCO_3 were first de-agglomerated and then further reduced to smaller particles by grinding actions and, at the same time, the newly created surfaces of smaller particles were covered by the agents under milling impact [39].

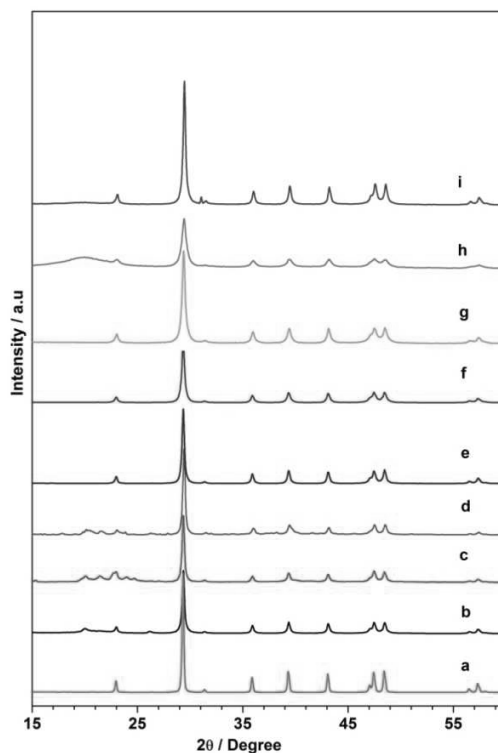


Figure.3.2: XRD patterns of CaCO_3 particles after milling in different capping agents (a) uncoated CaCO_3 , (b) OACHex, (c) SACHex, (d) PACHex, (e) SCCmet, (f) OLCmet, (g) ODCmet, (h) TPCmet, and (i) DDCxyl.

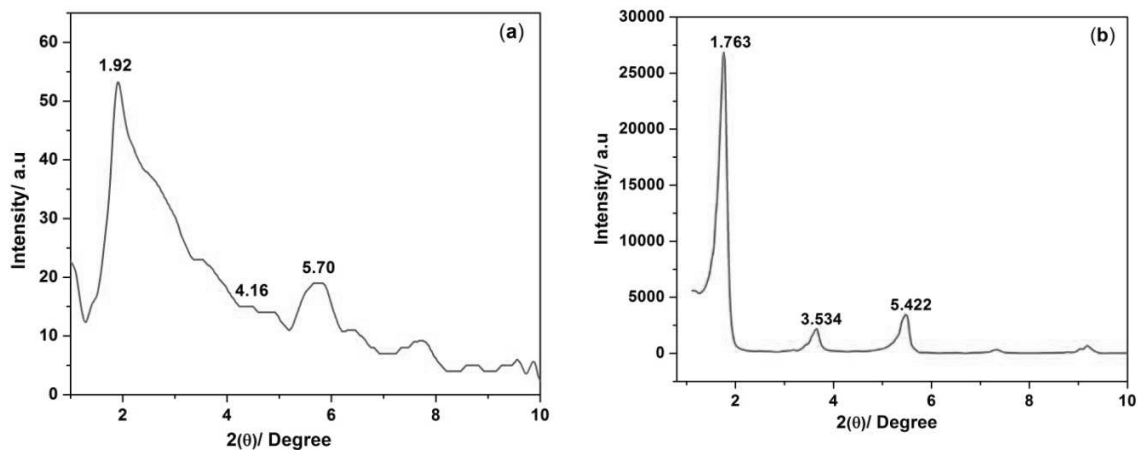


Figure.3.3: Low-angle XRD patterns for (a) OACHex, (b) SACHex

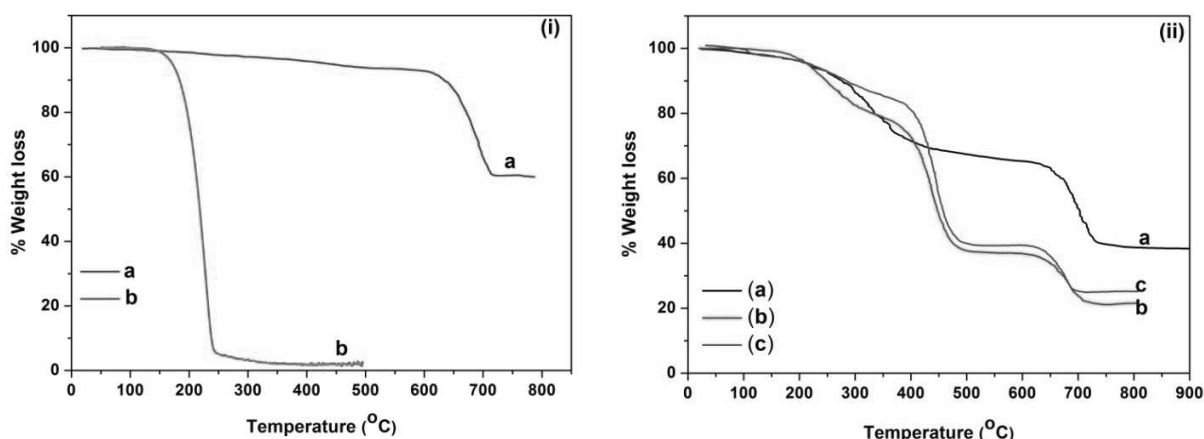
Table 3.3 comprises the crystallite sizes of the fresh (uncoated) and milled (coated) CaCO_3 with different capping agents; a decrease in crystallite size was observed after milling for all the samples. The impact of ball milling on the particle size reduction is a well-known fact as well as the coating by capping agents reduces the surface energy of calcite and could control the particle-particle interaction which was confirmed by Anshan and Taylor using IGC (inverse gas chromatography [130].

Table 3.3: Crystallite sizes of CaCO_3 milled with different capping agents.

S.No.	Sample	XS (Å)
1.	CaCO_3	519.87
2.	OACHex	299.37
3.	SACHex	338.75
4.	PACHex	321.12
5.	SCCmet	281.25
6.	OLCmet	372.00
7.	ODCmet	344.00
8.	TPCmet	341.50
9.	DDC _{xyl}	333.25

To compare the amount of coating with different dispersants over CaCO_3 surface thermal gravimetric technique was used to reveal the presence of organic moiety over the surface of CaCO_3 core.

TGA results from uncoated and coated CaCO_3 are given in Figure 3.4. Figure 3.4i shows TGA curve of the uncoated CaCO_3 and SA. The uncoated CaCO_3 undergoes two decomposition steps: a weight loss of 8.514% below 600°C and a large weight loss of 42.03% above 600°C indicating the complete decomposition of CaCO_3 to CaO and CO_2 . TGA curve of SA shows about 95% weight loss below 250°C indicating the complete thermal decomposition of organics under air atmosphere. Figure.3.4 (ii-iv) shows TGA curves for the coated CaCO_3 samples; overall there are three weight loss steps. The first step with minimal weight loss was primarily due to desorption of adsorbed solvents and excess of dispersants occurred below 250°C . The second step was in the temperature range from 250°C to 650°C , where the weight loss may be attributed to the thermal decomposition of coating agent. The final third weight loss observed after 650°C was due to the thermal decomposition of CaCO_3 to CaO and CO_2 . The weight loss of third step was found to be about 15- 40% for all of the samples that the percentage loss depends up on the second step weight loss; more (less) the second step less (more) the third step weight loss. The second step weight loss was found to be an important characteristic of the coated CaCO_3 .



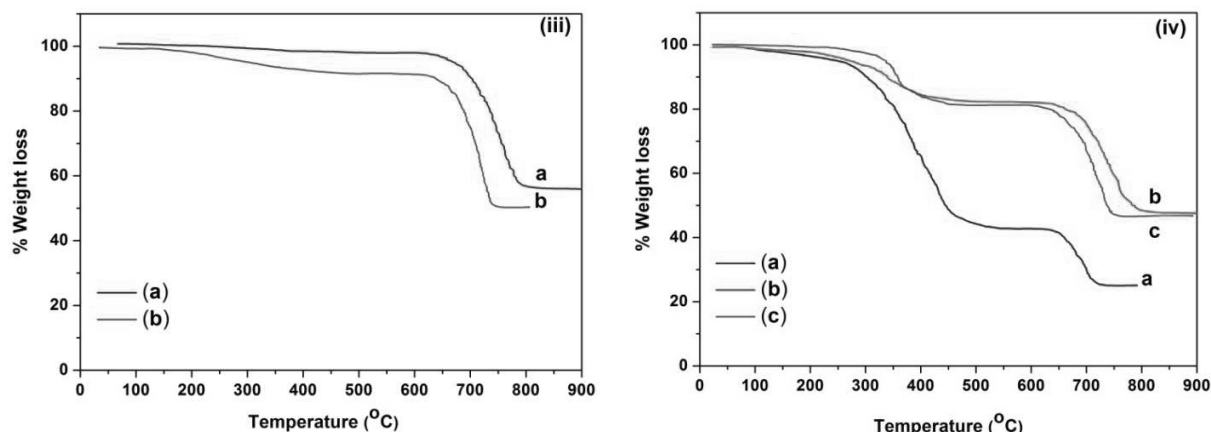


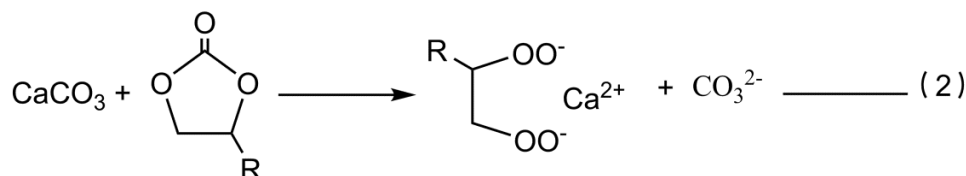
Figure.3.4: (i) Showing the thermal decomposition pattern for the (a) uncoated CaCO_3 and (b) SA; (ii) Showing the decomposition pattern for coated CaCO_3 with different capping agents (a) OACHex, (b) SACHex, (c) PACHex; (iii) (a) SCCmet, (b) OLCmet; (iv) (a) ODCmet, (b) TPCmet, (c) DDCxyl.

Table 3.4: The weight loss during the temperature range of 250°C-450°C corresponding to decomposition of calcium salt of capping agent for different capping agents.

S.No.	Calcium salts of Capping agent	Weight % loss of shell(approximate)
1.	Calcium salt of oleic acid	27
2.	Calcium salt of stearic acid	52
3.	Calcium salt of palmitic acid	49
4.	Calcium salt of salicylic acid	03
5.	Calcium salt of Oleylamine	06
6.	Calcium salt of ODSA	50
7.	Calcium salt of TPSA	15
8.	Calcium salt of DDSA	14

Table 3.4 indicates that the weight loss was more where efficacious reaction takes place between the CaCO_3 and capping agent. Typical acid-base reaction is expected with fatty acid and succinic anhydride based coating agents. However, in the case of SA and oleylamine minimal weight loss was observed indicating an ineffective reaction with calcite under milling condition. The reaction of SA might be hindered due to the presence of intramolecular hydrogen bonding

whereas no reaction is expected with oleylamine an organic base. Thus, a plausible reaction mechanism of calcite with coating agents except SA and oleylamine are in equation (1) and (2).



The thermal stability of the coated CaCO_3 was less than 200°C under air atmosphere. The physical stability of these samples is verified in the oil medium to form stable dispersion, which is essential for the lubricant application. All the samples except SCCmet and OLCmet (5-10%) were mixed with group II base oil to give stable, partially clear nanodispersion. These dispersions on left undisturbed in the glass cylinders were stable up to a month time.

The morphology and particle size of milled samples were characterized using TEM. Figure.3.5a shows that original CaCO_3 particles are agglomerated and cubic in shape with an average particle size of approximately 200 nm. With the addition of capping agents, the CaCO_3 powders were de-agglomerated and their shape was little distorted due to breaking down of primary crystals (Figure 3.5 (b-i)). Sample obtained after milling was in a size range of 85 to 120 nm. The dispersants have the reactivity of different extent for binding with CaCO_3 and results in different efficacy to stabilize the reduced size. From the images, it can be inferred that different dispersants gave different impressions to CaCO_3 particle shape and sizes. Most of the images show that particles were de-agglomerated and coated by dispersants. The maximum rupturing and de-agglomeration of cubes was observed for sample with ODSA capping (Figure 3.5g).

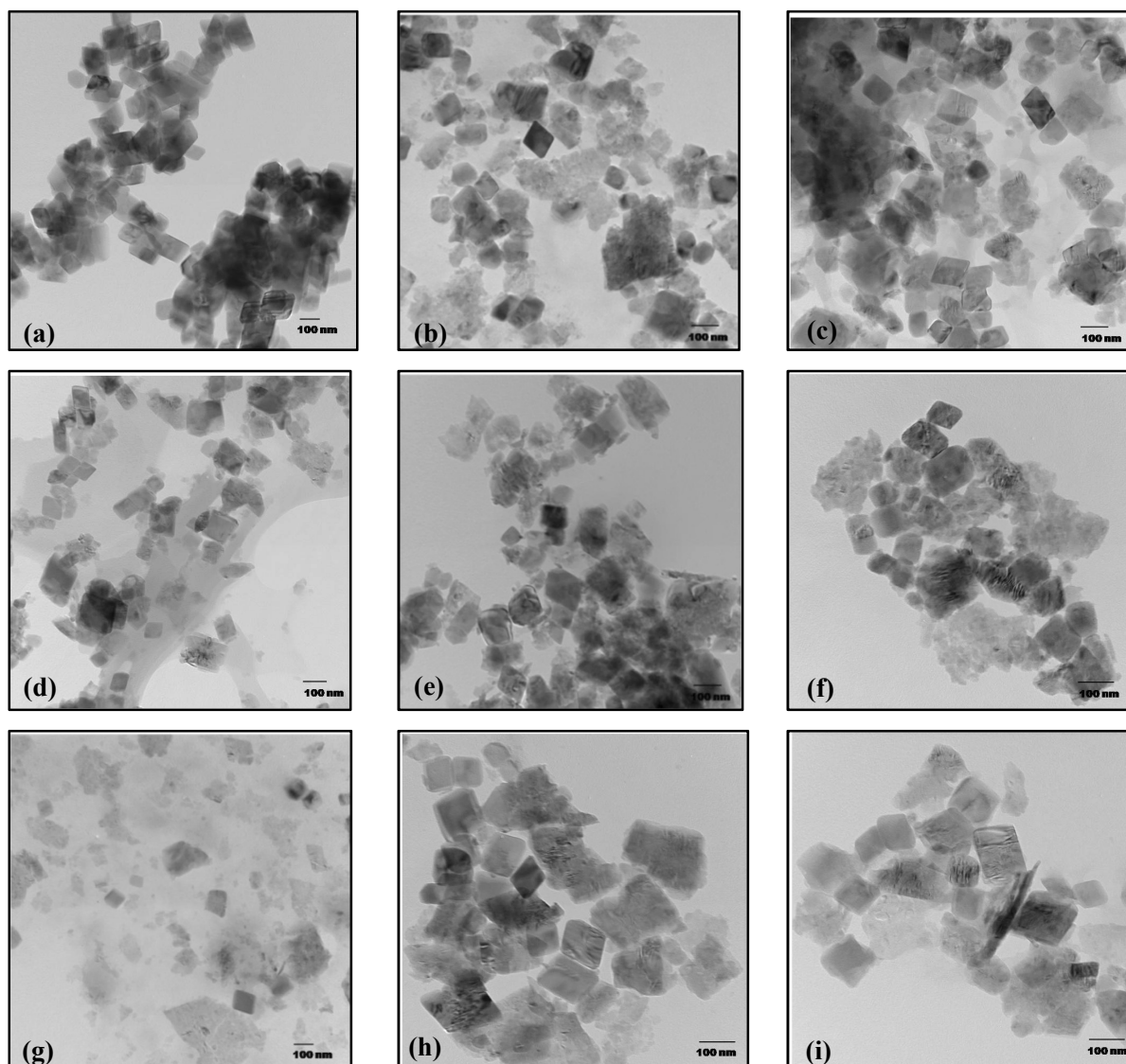


Figure.3.5: The TEM images of CaCO₃ particles: (a) uncoated CaCO₃, (b) OACHex, (c) SACHex, (d) PACHex, (e) SCCmet, (f) OLCmet, (g) ODCmet, (h) TPCmet, and (i) DDCxyl.

3.4. Coating thickness and surface density

From the results of TGA and TEM analyses, the shell thicknesses was estimated along with the surface density for every dispersant. Two quantities were obtained from TGA;

- i. The weight of CaO after the CaCO₃ decomposition,
- ii. The amount of capping agent used during the reaction to form the shell.

The cubic core-shell CaCO_3 structure is shown in Figure 3.6. where, a and b respectively, are length of the sides of core and shell. The particle size histogram derived from TEM images (Figure 3.7) gives the size of cubic particles of maximum distribution.

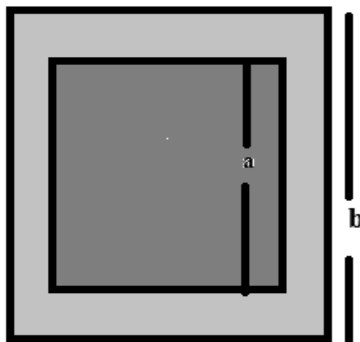


Figure.3.6: Representation of cubic core-shell CaCO_3 nanoparticle.

From the length a and b were obtained the volume of the cubic structure for n number of cubic nanoparticles;

$$V_{\text{core}} = a^3 \times n \quad (3.1)$$

$$V_{\text{total}} = b^3 \times n \quad (3.2)$$

The shell structure is made up of CaCO_3 and capping agent and if the shell volume is V_{shell} then can be obtained from equation 3.1 and 3.2 as

$$V_{\text{core}} = V_{\text{total}} - V_{\text{shell}} \quad (3.3)$$

The total volume and shell volumes are calculated from TGA weight loss by using respectively the bulk density of CaCO_3 (0.675 gcm^{-3}) and the dry bulk density of the prepared samples.

Thus the coating thickness is obtained from length of the sides a and b as follows;

$$t = \frac{b-a}{2} \quad (3.4)$$

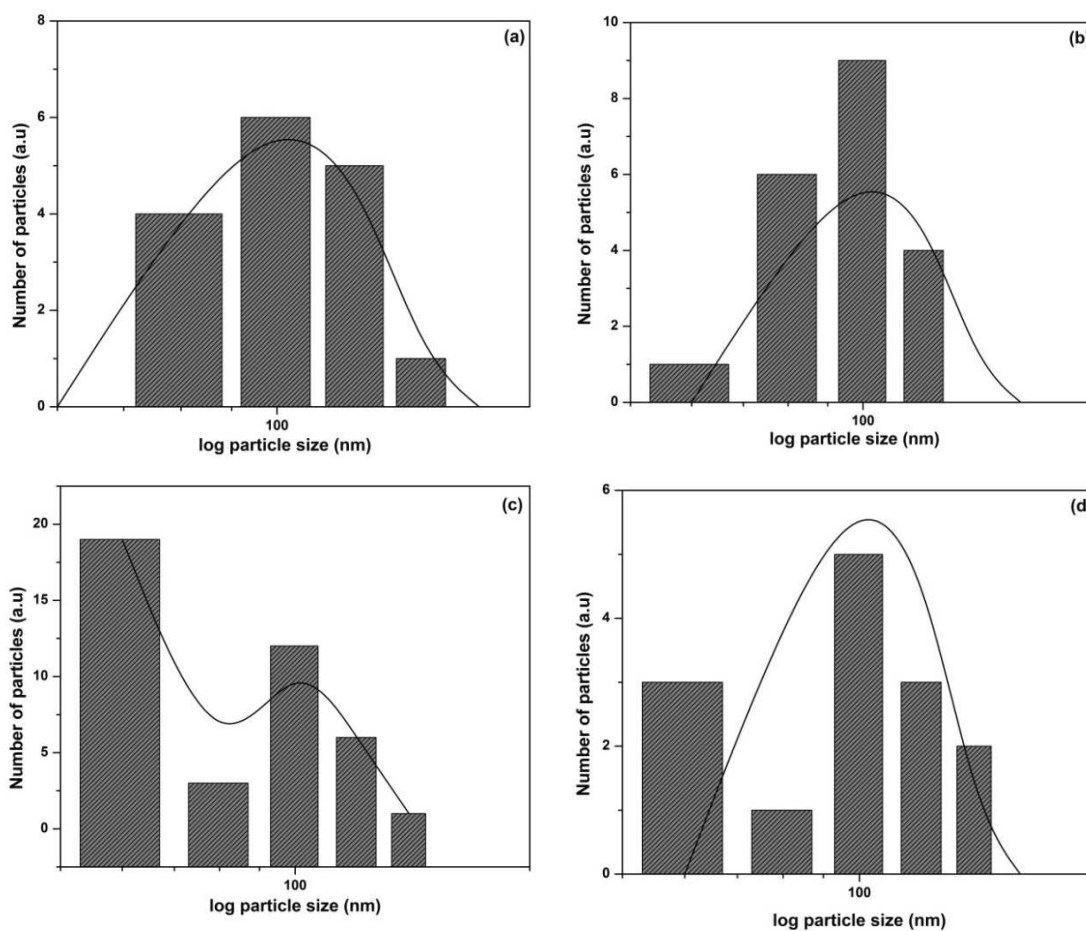
If we consider the reaction stoichiometry as two moles of capping agent involved per mole of CaCO_3 (except in the case of ODSA, DDSA, TPSA and oleylamine where one mole was utilized) then the weight (W) of the capping agent in the shell can be obtained from the TGA

weight loss. Thus, the surface density of the capping agent (the number of capping molecules coated over one cube) is given as follows:

$$\frac{W \times NA}{M \times 6a^2} \quad (3.5)$$

Where NA is Avogadro number and M is formula weight of capping agent.

Histograms derived from six representative TEM images, recorded at different positions of a grid, are given in Figure. 3.7.



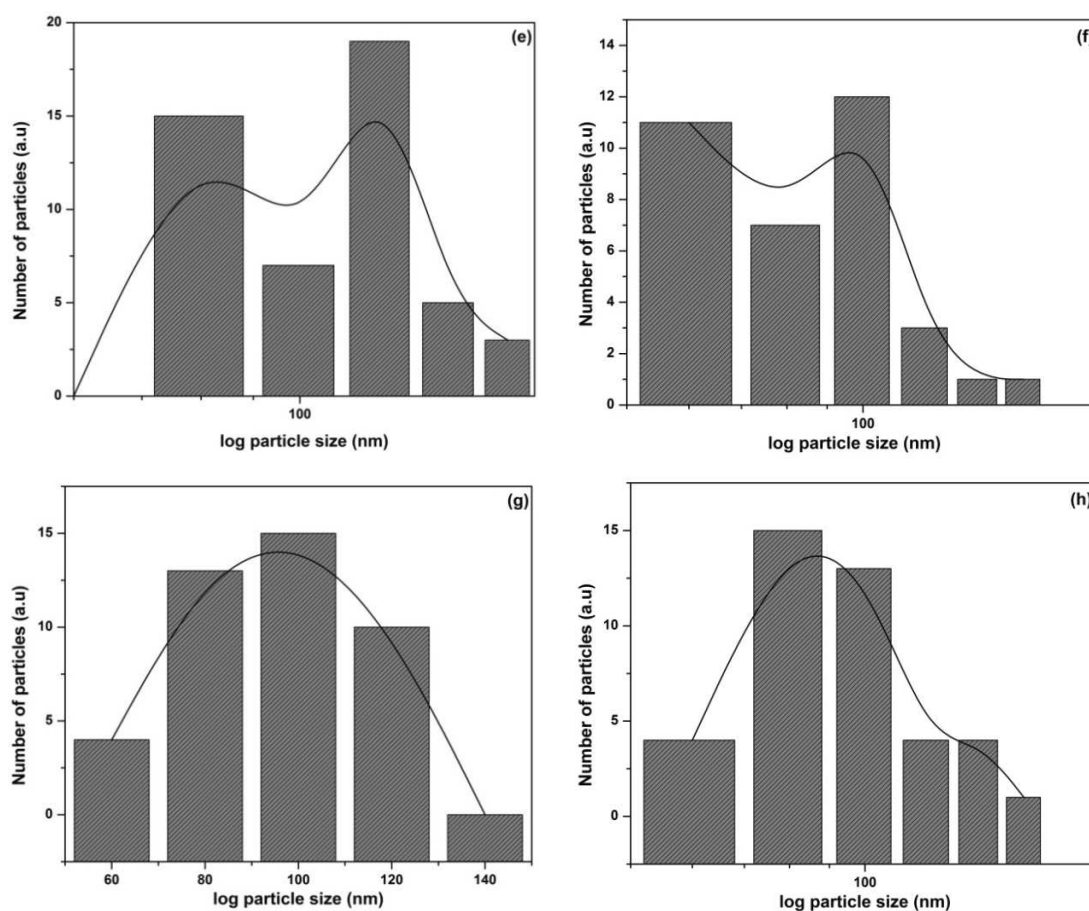


Figure.3.7: Showing the histogram plots for (a) OACHex, (b) SACHex, (c) PACHex, (d) SCCmet, (e) OLCmet, (f) ODCmet, (g) TPCmet, (h) DDCxyl.

Table 3.5: The shell thickness and surface density calculated using above calculations, with the help of TEM and TGA results.

S.No	Sample	TEM particle size(nm)	Thickness of Coating(nm)	Surface Density (molecules/nm ²) (10 ¹³)
1.	OACHex	102	1.85	2.65
2.	SACHex	103	3.35	5.04
3.	PACHex	101	3.00	2.41
4.	SCCmet	102	0.00	0.00
5.	OLCmet	118	0.35	0.90
6.	ODCmet	97	16.3	4.25
7.	TPCmet	95	1.00	5.70
8.	DDCxyl	87	1.69	2.90

From Table 3.5 we conclude that maximum coating thickness was obtained for ODSA coated CaCO_3 (16.3 nm) followed by SA coated CaCO_3 (3.35nm), while the surface density calculated for both these sample show different effects due to stoichiometric molar ratios being different for both the capping agents. However, SA coated sample displays no surface coating as per the calculation and likewise oleylamine shows a very negligible surface coverage having surface density of 0.9×10^{13} molecules/ nm^2 with coating thickness of 0.35 nm only. Similar findings were observed in TGA results.

Below are the TEM images (Figure. 3.8) for coated OA samples 3.7(a) at 40,000X showing cuboidal crystals. It was observed that surface of these crystals starts crumpling 3.8(b) when the sample was exposed to beams for a time of 10 seconds. Further, when the exposure time was increased to 30 seconds it was discovered that the entire surface film has been crumpled 3.8(c). A similar observation has been reported earlier [132]. This observation further confirms the presence of organic coating on the CaCO_3 surface generated by mechano-chemical reaction, which has been decomposed by the high electron beam energy inside the TEM.

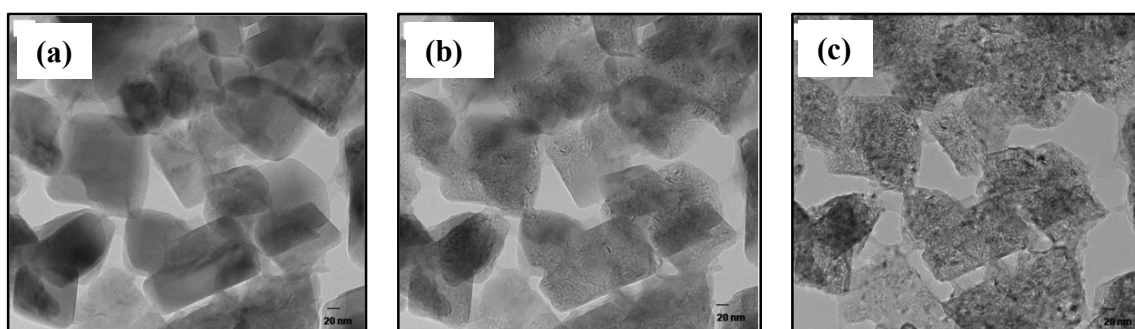


Figure.3.8: Showing the TEM images (a) OACHex, (b) OACHex after 10 sec of beam exposure and (c) OACHex after 30 sec of beam exposure.

3.5. Coating effect and surface area

Surface area analysis of the milled samples was conducted to measure the change in surface area during the milling process. Table 3.6 shows the values of the surface area for different milled samples.

Table 3.6: Surface area for various milled samples compared with thickness of coating.

S.No.	Sample name	Thickness of coating(nm)	Surface area (m ² /g)
1.	CaCO ₃	...	14.9
2.	OAChex	1.85	7.3
3.	SAChex	3.35	9.7
4.	PAChex	3.00	29.76
5.	SCCmet	0.00	33.42
7.	OLCmet	0.35	28.21
6.	ODCmet	16.3	4.83
8.	TPCmet	1.00	25.08
9.	DDC _{xyl}	1.69	14.73

The fresh sample shows low surface areas, about 14.9 m²/g. It is evident from the table that the samples, which were effectively coated, show a decrease in surface area compared to fresh samples. For instance, the maximum coated sample ODCmet shows the smallest surface area because of the coating over the surface. Similarly SA coated sample also gives lower surface area values. The degree of coating varies depending on the reactivity of dispersants with CaCO₃ and that affects the surface area of the sample. However, the surface area of samples (PAChex, OLCmet, SCCmet) are more than the fresh sample. There was zero or very negligible coating observed with these samples because of no reaction between OLCmet or SCCmet with CaCO₃. The newly generated surfaces during milling were not coated with dispersants molecules and thus higher surface area was observed for these samples.

3.6. Conclusion

Synthesis of hydrophobic core shell type CaCO₃ particles via the ball milling approach using different capping agents was presented. The observed results demonstrate that coating was successfully done that helps in reducing the agglomeration of NPCC to different extents. It has also been demonstrated that organic substrate (capping) alters the crystal morphology and surface properties of CaCO₃ by making it hydrophobic. It was found that different capping

agents show different tendencies to coat the CaCO_3 surface and have different influence on the particle size, morphology and surface hydrophobic property. These coated calcite samples are potential candidate for overbasing applications in lubricant technology.

Ball milling of selected dispersant (stearic acid) for optimization of milling parameters

4.1. Introduction

CaCO_3 is a widely used material in different chemical industries for numerous applications in oil, paint, plastics industries and agriculture sector. In the downstream oil sector for the preparation of basic additives calcium compounds are the natural choices due to their availability in the pure form and used in maintaining the reserve basicity in the product matrix. Owing to its alkalinity, the most important application of CaCO_3 is overbasing in lubricant formulation. During combustion, the sulfurous and nitrogenous impurities present in fuel get oxidized to inorganic acids. In turn, the lubricant itself undergoes oxidative degradation to form organo-acids. These acids would cause severe corrosion to the engine parts if allowed to build up and thus may reduce the drain interval duration. In order to treat the acid build up, overbasing or detergents is one of the most important additives added to lubricants. The role of overbasing additive is not limited to prevent acid build up or rust formation, which promotes engine cleanliness, oxidation inhibition and extended trouble-free operation. Nano CaCO_3 (and $\text{Ca}(\text{OH})_2$) in the colloidal form stabilized by a surfactant layer is used as an overbasing additive in lubricant formulations [2-9, 42].

Surface modification of CaCO_3 is of prime importance in making overbasing additives; the surfactant layers help to disperse otherwise non-dispersible CaCO_3 in the oil medium. Recently, we reported the surface modification of CaCO_3 using different surfactants through ball milling approach. The clear advantage of milling approach for surface modification of CaCO_3 over chemical synthesis routes has been well documented [133].

In solution and carbonation routes there are certain conditions (reaction time, temperature, gas flow, pH) that exist that crucially affecting the crystal growth and morphology of CaCO_3 ; whereas in ball milling process no such significant problems exist, except the above-mentioned milling parameters. However, these parameters can be controlled in an industrial scale with ease to give better tailored hydrophobic materials. The desirable phase and morphology of the solids (for instance calcite and cubic CaCO_3) can be selected for milling with suitable surface modifier (SA).

Recently, super-hydrophobic CaCO_3 nanoparticles have been prepared by surface modification of CaCO_3 using OA followed by polydimethylsiloxane (PDMS) through simple process. PDMS helps in creating super hydrophobicity (contact angle was found to be 167°) as well as dual type of roughness on the surface that adheres tightly to the substrate due to high adhesion of the polymer [134]. A silane-coupling agent was also found to modify the CaCO_3 surface by improving the dispersion and interfacial compatibility between CaCO_3 and styrene-butadiene rubber (SBR) latex using hydrothermal route. A silane-coupling agent modified CaCO_3 nanoparticles assists in decreasing the viscosity of CaCO_3 by improved hydrophobicity and reduced surface energy and hence making it compatible with SBR latex [135].

The coating thickness of surfactants over CaCO_3 was reported and the coating efficacy was correlated with respect to the reactivity of CaCO_3 and surfactant molecule. Nevertheless, the milling parameters should also play an important role in achieving efficient coating over CaCO_3 . In the preparation of nanodispersion for overbasing applications the stability of the dispersion of active materials is very important; it is desirable to control particle size in order to be gravitationally stable when dispersed in desired matrix [136]. Further, the low average particle size in the nanometer range and monomodal narrow particle size distribution of surface modified CaCO_3 is important for preparing stable dispersion. Surface modified CaCO_3 has potential applications in lubrication provided the nanoparticles form a stable dispersion in the lubricant matrix by having a balanced brownian motion and gravitational pull.

In this regard, coating of CaCO_3 with SA was investigated by applying various milling parameters such as milling duration, sample to ball ratio, molar CaCO_3 to SA ratio and milling medium. The coated CaCO_3 materials were characterized by relevant physicochemical techniques and the results are presented here.

Surface modification of precipitated CaCO_3 particles realized in a planetary ball mill using SA as a modification agent for making dispersion in hydrocarbon oil was investigated. Different milling parameters such as milling time, ball/sample weight ratios, sample dosage and milling medium were varied and analyzed for optimization of efficient coating. The physical properties of the hydrophobically modified CaCO_3 were measured; the particle size and morphology of the resulting samples were evaluated using TEM and XRD techniques. The surface coating thickness was estimated using SAXS.

4.2. Experimental work

SA (laboratory grade), hexane (laboratory grade) were purchased from commercial market. Precipitated CaCO_3 (THIOX- CARB 300) having particle size of 6-10 μ was purchased from Specialty minerals Lifford, Birmingham. Precipitated CaCO_3 was ball milled in Retsch PM-400MA planetary ball mill with ZrO_2 (stabilized zirconia) balls in ZrO_2 vessels by keeping the volume of milling content to one third of vessel volume (500 ml). SA was mixed with precipitated CaCO_3 in different mole ratio. Hexane was used as the milling medium. The milling was carried out in three steps, as per the sequence detailed below.

- Step 1: Milling with 1 mm ball at 1200 rpm followed by sieving.
- Step 2: further milling of the sample obtained after step1 with 0.5 mm ball at 1200 rpm and sieving.
- Step 3: and third milling of the sample obtained after step 2 with 0.1 mm ball at 1200 rpm and sieving.

The stepwise milling led to effective particle size reduction in small stages otherwise direct milling of initial CaCO_3 with 0.1 mm balls would not be effective.

Vibratory particle sieving was performed using a 3D sieve shaker (AS 200 of M/s Retsch) to separate the milling balls from the sample after milling. During sieving, it was ensured that no solid particles remained by increasing the amplitude of vibration. Different sizes of sieves were used to separate different ball sizes, as mentioned in Table 4.1 below.

Table 4.1: Sieve sizes used while separating the balls from the sample.

S.No.	Sieve Size (micron)	Ball size (mm)
1.	600	1
2.	300	0.5
3.	70	0.1

The mass of the sample remains nearly the same (negligible loss due to interstitial volume among the balls) after each sieving step because no particles were separated during sieving and the whole mass was kept for further milling. Hence, the ball to sample ratio was considered the same in every milling step.

The milling time for different ball sizes (1, 0.5 and 0.1mm ϕ) were also varied (2, 4 and 6 hours). After the milling, procedure samples were washed in order to remove excess of SA with hexane through centrifuging and dispersing steps. After washing, the wet sample was subject to particle size and TEM analysis, the sample was dried at 60°C for XRD and contact angle measurement. The samples are described in Table 4.2 with eight alpha-numeral characters, in which the first two letters refer to stearic acid (S) and CaCO₃(C), followed by three digits that indicate, respectively, the molar ratio between S and C, balls to sample (S+C) weight ratio and time (in hours sample were sequentially milled with 1, 0.5 and 0.1mm balls); the last three letters are milling medium hexane (hex).

Table 4.2: Description of samples

Sample description	S:C (molar ratio)	Ball: (weight ratio)	Sample	Milling time/h (*3)	Milling medium
SC112hex	1	1		2	Hexane
SC114hex	1	1		4	Hexane
SC116hex	1	1		6	Hexane
SC216hex	2	1		6	Hexane
SC226hex	2	2		6	Hexane
SC246hex	2	4		6	Hexane

The synthesized samples were characterized using various analytical techniques, such as XRD, TGA, raman, TEM and SAXS.

4.3 Effect of milling parameters

The experiments were carried out to investigate the effect of milling parameters such as milling time, sample to ball ratios, reactant molar ratios and milling medium, on the shape and size of the hydrophobic CaCO₃ particles and the results are discussed in this section.

The XRD patterns from the fresh and milled CaCO₃ samples are given in Figure 4.1-4.3.

The molar ratio of reactant (CaCO₃: SA = 1) and ball to sample ratio (1:1) were fixed to optimize the milling time. The samples were milled for different time intervals (2, 4 and 6 hrs) as detailed

in the methods and the effect of milling time on the phase purity and crystallite size are summarized in Figure 4.2 and Table 4.3.

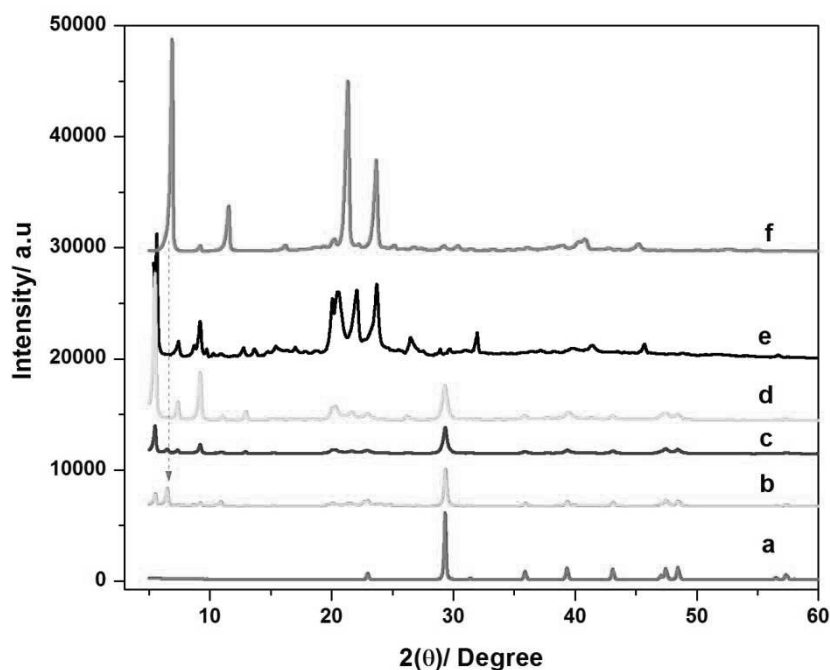


Figure 4.1: XRD pattern for (a) unmilled sample, (b) SC112hex, (c) SC114hex, (d) SC116hex, (e) pure calcium stearate and (f) SA.

Table 4.3: Crystallite size (Å) and particle size (nm) for sample ball milled for different time intervals.

Sample	XRD Xs Å{1 0 4}	DLS particle size (nm) d ₉₀
SC112hex	414	434
SC114hex	257	260
SC116hex	191	224

The major reflections observed are from calcium stearate (below $2\theta = 15$) and calcite (above $2\theta = 20$) that match well with the reflections of standard calcium stearate and fresh CaCO_3 . For comparison purposes, standard SA was given in Figure 4.1. The intensity of calcium stearate reflection increases with milling time that implies the formation of calcium stearate during milling of CaCO_3 with SA. The major peak of calcite ($2\theta = 29.35$) broadens that indicates the

primary crystallite size of fresh CaCO_3 was significantly reduced with milling time. It is noteworthy that the major reflection of SA ($2\theta = 6.95$, indicated by arrow) was observed in 2 and 4 h samples and that disappeared in the 6h sample. This indicates the presence of SA on the surface of calcite despite the samples being subjected to effective washing after milling. This may be attributed to the SA (molecular form or strongly adsorbed form) coating along with calcium stearate on the calcite surface during milling up to 4h. Beyond 4h, this adsorbed SA was converted to calcium stearate. Thus, the 6h milling time was found to provide complete coating and effective for particle size reduction and hence was chosen to optimize other milling parameters. The particle size d_{90} (Table 4.3) observed from DLS has also indicated the effective size reduction after 6h milling and was recorded as mentioned in chapter 2 section 2.2.1. The effect of molar ratio of reactant (SA: CaCO_3 , from 2 to 1) on the particle size reduction was significant as it is evident from the d_{90} value; however, there are hardly any changes in the XRD reflections (Figure 4.2 a, b) and the crystallite size (Table 4.4).

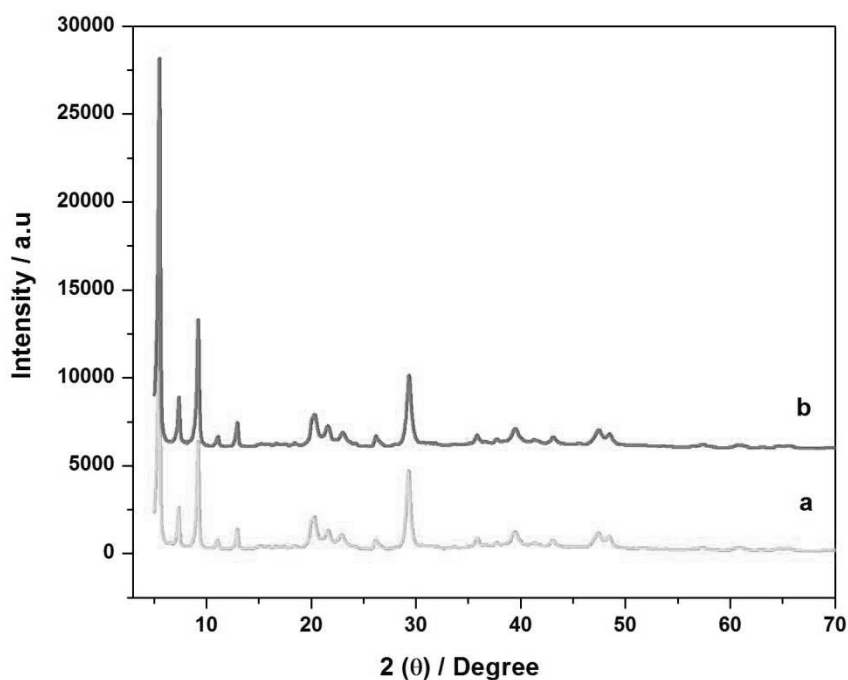


Figure 4.2: XRD patterns showing the effect of different doses of SA w.r.t CaCO_3 for SA modified CaCO_3 (a) SC116hex and (b) SC216hex

Table 4.4: Crystallite size (Å) and particle size (nm) for samples ball milled with different sample doses.

Sample	XRD Xs Å{1 0 4}	DLS particle size d ₉₀ (nm)
SC116hex	191	224
SC216hex	177	131

This indicates that the crystallite size reduction depends more on the milling time than the molar ratio of the reactant. On the other hand, the higher amount of SA might lead to complete or near complete coating of calcite that could hinder the agglomeration of calcite particles and hence smaller particle size was obtained with molar ratio (SA: CaCO₃, from 2 to 1) in the DLS. The effect of ball to sample ratio on the crystallite and particle size reduction were also studied; the higher the amount of balls (2:1 or 4:1), the greater the reduction in crystallite size, which indicates the greater impact of milling on the sample (Table 4.5).

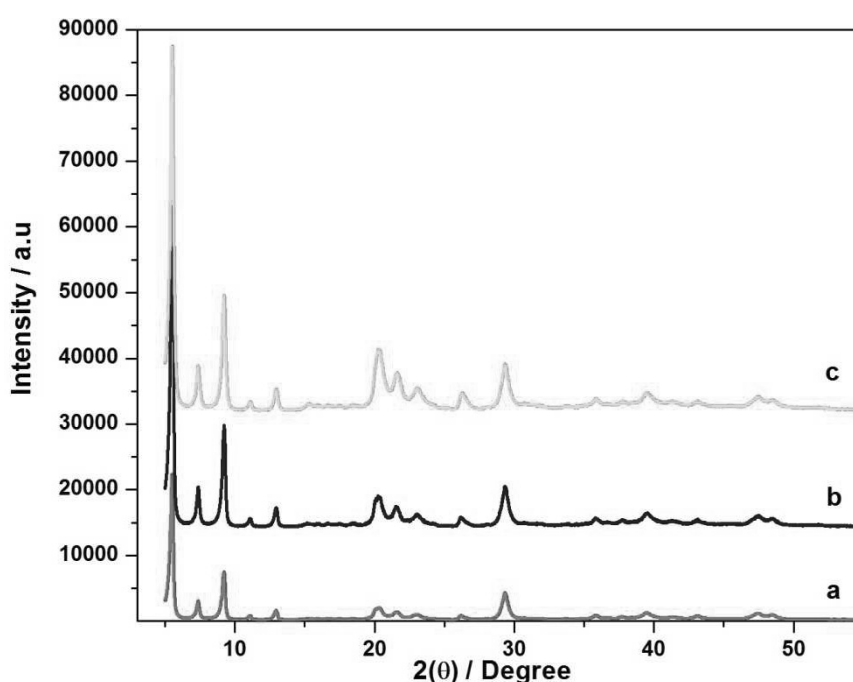


Figure 4.3: XRD patterns showing the effect of different ball ratio for SA modified CaCO₃ (a) SC216hex, (b) SC226hex and (c) SC246hex.

Table 4.5: Crystallite size (Å) and particle size (nm) for samples ball milled with different ball ratios.

Sample	XRD Xs Å {1 0 4}	DLS particle size(nm)d ₉₀
SC216hex	177	131
SC226hex	129	102
SC246hex	114	78

However, due to crystal breakdown, there are new surfaces exposed and thus the particles tend to agglomerate in order to dissipate the high surface energy. The DLS d₉₀ results for ball to sample ratio (Table 4.5) also indicate increased particle size.

The following findings are observed from the above results that crystallite size depends largely on the impact of milling (duration and ball amount), whereas the particle size depends on the amount of SA used for milling. XRD patterns observed for all of the samples show the presence of calcium stearate and calcite (Figure 4.2 and 4.3), which reveals that the calcite phase remains intact during milling regardless of the parameters applied. Particle size reduction is discussed in detail in section 4.4 under morphology of particles.

Raman analysis was carried out, as described in chapter 2 section 2.2. to support the other analytical techniques. Raman results confirm the formation of the calcium salt layer of SA.

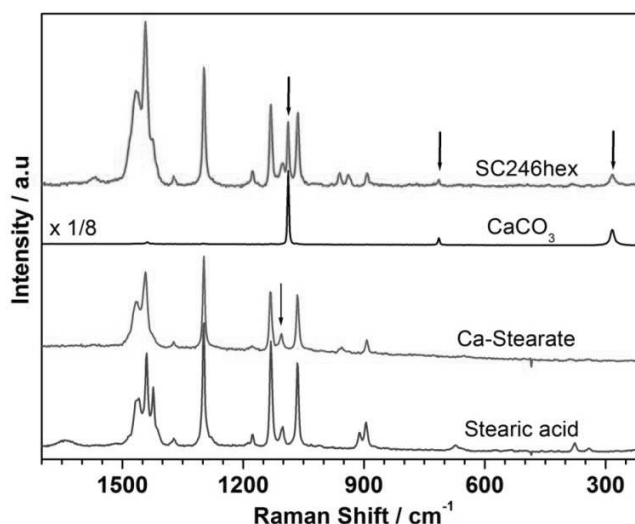


Figure 4.4: Raman spectra. (Note spectrum intensity of CaCO₃ was reduced to one eighth to match with the intensity of other spectra).

Raman spectra of CaCO_3 , SA, calcium stearate and ball milled CaCO_3 are given in Figure 4.4. Pure CaCO_3 shows two weak and one strong stoke line at 285, 714 and 1088 cm^{-1} . The spectra of calcium stearate and SA are similar, except for the absence of 1422 and 911 cm^{-1} peak in former. The spectrum of milled sample SC246hex shows predominantly the features of calcium stearate, in addition excitation lines of CaCO_3 were observed (indicated by arrow). The existence of such combined spectral features clearly indicates the calcium stearate coating over CaCO_3 .

Thermo gravimetric studies were carried out for the starting material and milled sample, as described in chapter 2, section 2.2.4.

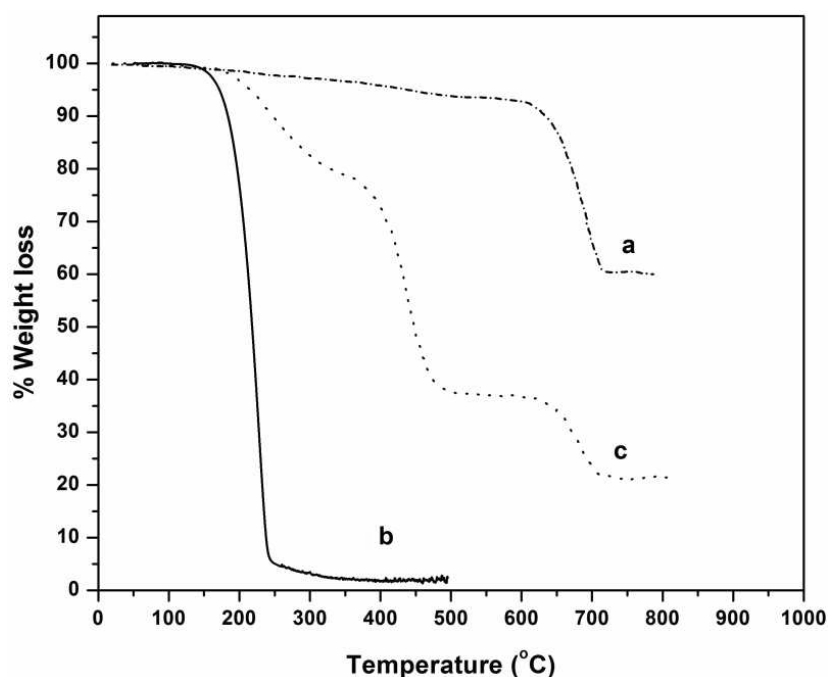


Figure 4.5: TGA curves of (a) unmodified CaCO_3 , (b) SA and (c) SA modified CaCO_3 (SC116hex) from room temperature to 900°C at heating rate of 10 deg/min in air medium.

TGA of fresh CaCO_3 (Figure 4.5a) was obtained in air medium with a total weight loss of 50.54%. The decomposition curve consists of two stages; the first before 600°C with a weight loss of 8.514% that corresponds to the decomposition of Ca(OH)_2 impurity in this CaCO_3 and the second after 700°C, indicating the complete decomposition of CaCO_3 into CaO and CO_2 with a loss of 42.03%. Figure 4.5b shows TGA of SA in the presence of air medium, which is a single step weight loss (95.86 %) at 250°C that reaches to 99.56% at 400°C, indicating the complete decomposition of SA. A small weight loss tailing before becoming a zero loss straight

line is observed near 300°C. The reason could be the burning of residual carbon, which might form from the decomposition of SA under air atmosphere. Overall, this small weight loss is negligible compared with the main weight loss. On the other hand, the decomposition pattern of milled CaCO₃ shown in Figure 4. 5c (SC116hex) comprises of a three step weight loss. The first step was only 10.37%, which is attributed to the loss by decomposition of adsorbed SA that was not removed by washing procedure from the milled sample and was completed before 350°C. The second step weight loss starts just after first step and ends before 600°C and is showing about 62.90% weight loss, which is attributed to the thermal decomposition of calcium stearate or chemically embedded SA might also be termed as an organic-inorganic hybrid shell. The final or third step weight loss is due to the decomposition of CaCO₃ into CaO and CO₂. The decomposition onset and end temperature of this third step weight loss matches well with that of fresh CaCO₃(Figure 4.5a). These above three stage TGA weight losses show that the milled CaCO₃ consists of three components; calcite core, chemically embedded SA (shell) onto the core and physically adsorbed SA onto the shell. It is worth mentioning that physically adsorbed SA decomposes at a higher temperature (almost 100°C) compared to that of pure SA (Figure 4.5b). This shows that physically adsorbed SA is well oriented (tail to tail) over the calcium stearate shell, which could influence the decomposition temperature of SA. A similar trend was observed for all samples (data not given) that show the formation of a calcium stearate shell on the calcite surface during milling conditions.

4.4. Morphology of particles

The morphology and particle size of fresh and ball milled CaCO₃ were characterized using TEM studies as mentioned in chapter 2 section 2.2.3. Figure 4.6 shows that fresh CaCO₃ was though agglomerated, purely cubic in nature with an average particle size of approximately 200 nm. Ball milling for fresh CaCO₃ with SA leads to particle size reduction through gradual destruction of the cubic morphology depending upon the milling conditions and parameters. The addition of SA as a capping agent was observed to hinder the agglomeration of CaCO₃ particles. The formation of calcium stearate as a shell over the surface of CaCO₃ enables the deagglomeration of the particles [34].

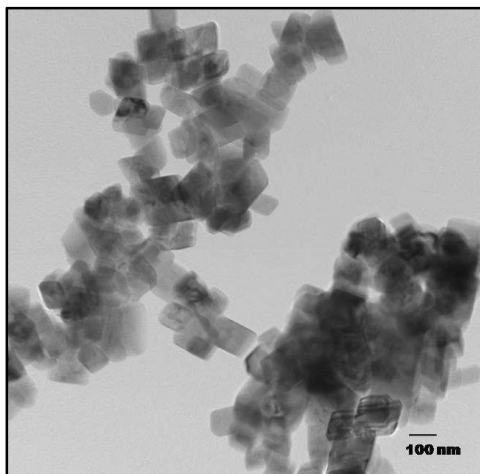


Figure 4.6: TEM image of uncoated CaCO₃ particles.

The milling time dependency of morphology and particle size of calcite samples after 2, 4 and 6h milling duration is given in Figure 4.7(a, b and c). The cubic morphology was intact during the first 2h milling time as is evident from Figure 4.7a compared with the fresh calcite in Figure 4.6. However, 4 and 6h milling duration was found to severely affect the morphology and size reduction. The indefinite shape of particles indicates the severity of the milling condition and the particle size reduces substantially with milling time and the particles appeared as agglomerates in Figure 4.7(b and c). The particle size observed from DLS measurement also implies the size reduction with milling duration, as shown in Table 4.1. Thus, 6h milling duration was kept fixed to evaluate the influence of other parameters on the morphology and size reduction. A similar effect on the particle size was observed with the ball to sample ratio (1, 2 and 4), as shown in Figure 4.7(d-f); the greater impact of larger quantity of balls on the sample was evident from the observed size reduction in the representative images.

The reactant molar ratio (SA: CaCO₃, 2 and 1) dependency of particle size (Figure 4.7 (c and d)) was hardly visualized in the TEM unlike DLS studies revealed, which is due to the agglomeration of particles after solvent evaporation during sampling.

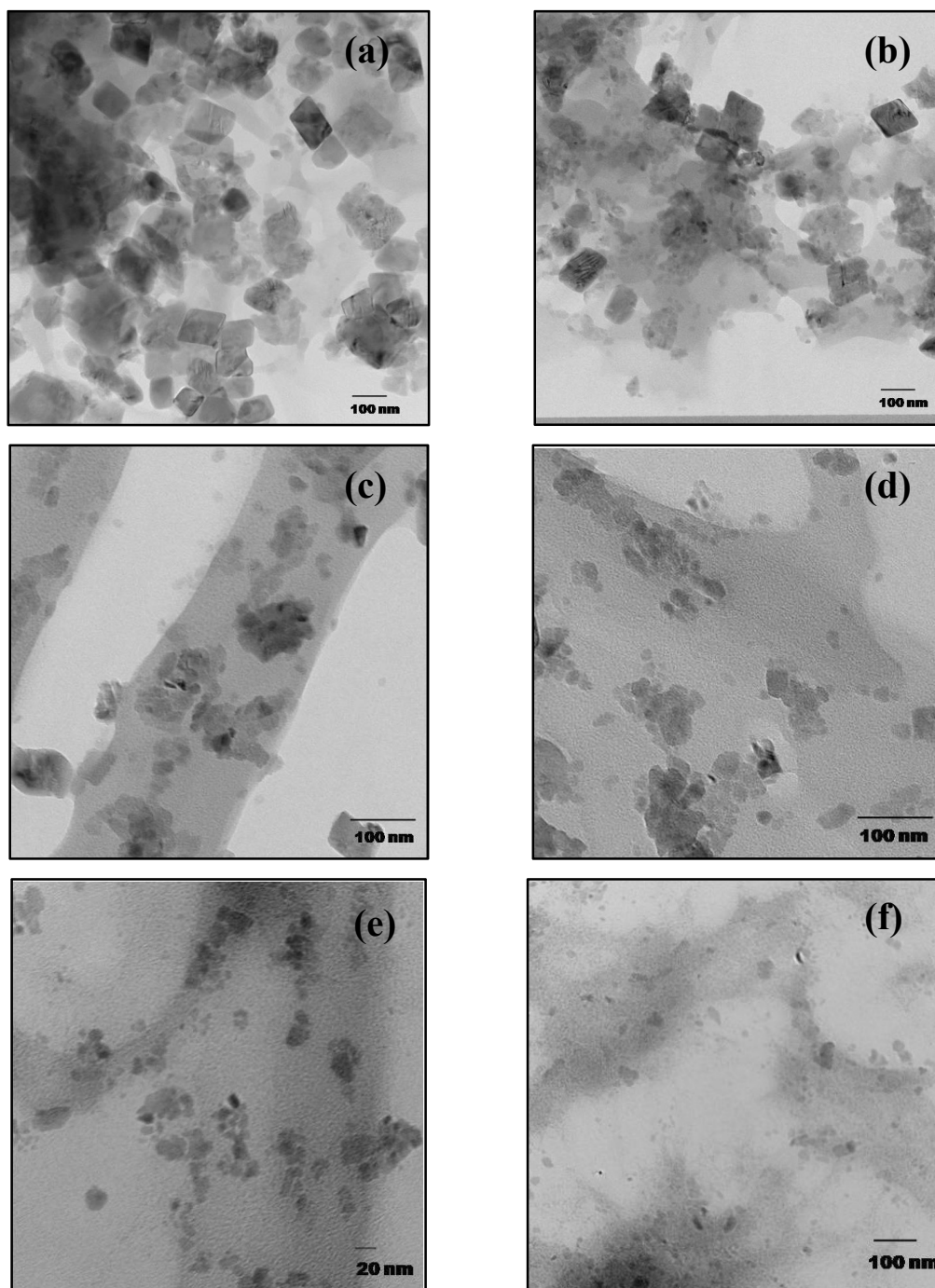


Figure 4.7: TEM images of SA coated CaCO_3 particles (a) SC112hex, (b) SC114hex, (c) SC116hex, (d) SC216hex, (e) SC226hex and (f) SC246hex.

4.5. Analysis of modified surface

The hydrophobic characteristics of the modified CaCO_3 surface are measured by the contact angle measurement, as described in chapter 2, section 2.2.6., shown in Figure 4.8, (for comparison fresh CaCO_3 was also given). A water droplet on fresh CaCO_3 (Figure 4.8a) resulted in no stable drop shape and water was imbibed in the pellet slowly. The contact angle of water on pure CaCO_3 was found to be small (nearly 59°) and this is due to the hydrophilic nature of fresh CaCO_3 . The contact angle of ball milled CaCO_3 (SC116hex) shows, 99.3° (Figure 4.8b), which indicates a small, hydrophobic character imparted on the calcite surface due to stearate shell coating.

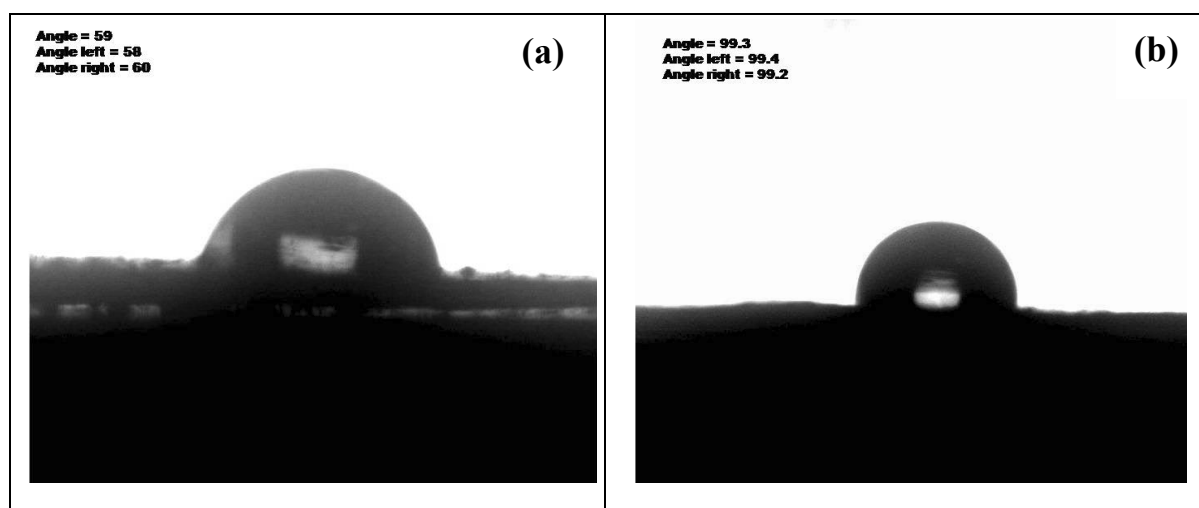


Figure 4.8: Contact angle measurement of CaCO_3 in (a) absence of organic additive and (b) presence of SA.

SAXS analysis was performed in order to determine the type/ characteristics of coating and the value of coating thickness.

Figure 4.9 shows the SAXS pattern from (SC226hex and SC246hex). The scattering curves of both samples are nearly identical. At $q = 16.3 \text{ nm}^{-1}$ the most intense reflection of the calcite structure of CaCO_3 was observed. At $q = 18.5 \text{ nm}^{-1}$ the most intense reflection of the aragonite structure of CaCO_3 has also been observed. The most intense reflections were found at large scattering angles of both the calcite and aragonite phase of CaCO_3 . It may be inferred that during high intensity milling a minute fraction of calcite might have been converted into aragonite; which was stable under surface capping and not detected from the XRD results. Additionally, at q values of 12.8, 14.4, and 15.3 nm^{-1} , signals were observed which correspond to

distances in real space of 0.49, 0.44, and 0.41 nm, and this was attributed to calcium stearate shell structure. Two weak reflections at $q = 8.0 \text{ nm}^{-1}$ (very weak) and $q = 9.3 \text{ nm}^{-1}$ can also be seen.

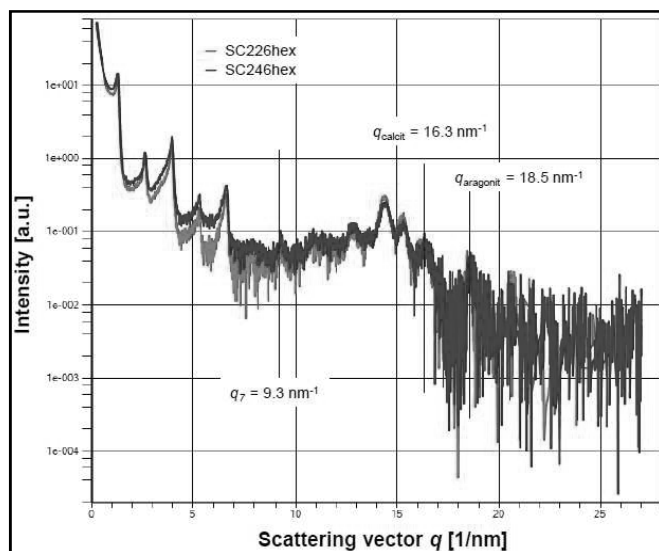


Figure 4.9: Small angle X-ray scattering (Imaging Plate); red curve SC226hex and blue curve SC246hex.

The scattering signal of these samples is dominated by a multi-lamellar structure, which is most likely due to the strongly adsorbed SA and stearate coating. This multi-layer structure was due to the use of excess acid, which reacted to the freshly generated CaCO_3 crystallites and led to further adsorption of SA. It might be inferred by SAXS study that the shell structure of organic-inorganic coating of CaCO_3 nanoparticles was done effectively and parameters were optimized. The layer thickness determined from the position of first reflection q_1 ($d = 2\pi/q_1$) is 4.7 nm (including multi-layer) for both these samples. This shows that the surface coating of CaCO_3 could be complete or has reached saturation under these conditions.

4.6. Conclusions

This chapter reports the synthesis of hydrophobic CaCO_3 via ball milling, using SA as a surface modifier. Several parameters like milling time, sample to ball ratio, molar ratio of reactant and milling medium were varied. Results from this work show that SA coating successfully reduced agglomeration of CaCO_3 after milling. It has also been demonstrated that an organic substrate

(SA) alters the surface properties of CaCO_3 by making it hydrophobic. It was found that different milling parameters have different influence on the particle size of CaCO_3 . On increasing the milling time, ball to sample ratio and molar ratio of SA to CaCO_3 the particle size considerably reduced, as evident from DLS and TEM results. Longer milling time and higher ball ratio have a direct impact on the size reduction; whereas a higher amount of SA hinders the agglomeration of CaCO_3 particles by surface coating. Hydrophobic character was imparted on milled CaCO_3 sample, which was also confirmed by contact angle measurement. Thus, the surface modified hydrophobic CaCO_3 nanoparticles are potential candidates for overbasing applications in lubricant technologies.

Tribological behavior of surface modified exfoliated MoS₂ nanosheets**5.1. Introduction**

Tribological applications of MoS₂ have been limited because of the dispersibility issues in hydrocarbon/oil media. Furthermore, it is easily oxidized in air to molybdenic oxide which has a negative influence on the AW and friction reducing properties of the lubricating oil. Hence, oil soluble MoDTC/ MoDDP has been used which *in situ* get converted to MoS₂ between the surfaces of mating metal parts under tribochemical condition [137]. This solubility issue in hydrocarbon oil medium could be resolved by improving MoS₂ dispersibility in the oil matrix by reducing its size or by exfoliating and stabilizing its layers.

The major challenge was to disperse inorganic nanomaterials within a non-polar hydrocarbon medium while maintaining the fineness of these particles in the dispersed state in the formulation. The requirement could be met by using MoS₂ particles in nanometer dimension.

The exceptional tribological properties were shown only by IF-like MoS₂ such as, nanospheres and hollow cage. Mass production and cost effective process need to be developed. Nevertheless, in order to evaluate tribological properties of the nanosized particles; the particles must be stable in hydrocarbon media, which could be achieved by modifying the nanoparticles surface using dispersant/capping agents/surfactant to make the surface hydrophobic and compatible with oil/ hydrocarbon non-polar phase.

The use of lecithin for exfoliating, as well for stabilizing the exfoliated graphene sheets during ultrasonication by reverse micelles formation in solution and over the graphene surface to prevent self-aggregation of exfoliated sheets was recently reported by Martin Pykal et. al. [138]. They found the poor results of exfoliation when chloroform was used for exfoliating the graphene sheets without lecithin.

This chapter describes a unique design of MoS₂ nanosheets tribology in oil giving a stable additive, consisting of layered inorganic nanoparticles (MoS₂) with organic agents (phospholipids (lecithin) in the presence of ZDDP (Zinc Dialkyl Dithiophosphate)/ ashless phosphorus free AW additive).

The stable oil-dispersible MoS₂ requires a nanosized structure, an oil compatible hydrophobic surface and stability in oil. To meet these requirements, micron-sized MoS₂ powders were ball

milled in the presence of Zn and P based AW additive (ZDDP), ashless phosphorus free AW additive as well as lecithin, which acts as an exfoliating agent. The impact of ball milling generates few layered sheets with high surface energy and severely strained structure, chemically linked and coated with AW additive and lecithin to minimize the surface energy of the newly generated nanosheets to achieve a stable dispersion. This chemically coated MoS₂ exfoliated nanosheets dispersed in oil and under lubrication conditions they would navigate through the asperities of the rubbing surface and form a durable tribo film to reduce friction and wear.

5.2. Experimental work

MoS₂ (98.2% pure) was purchased from Electro Ferro Alloys Pvt. Ltd., lecithin (P content 2.1%), ZDDP and ashless phosphorus free AW lubricant additives [Methylene bis(dibutyldithiocarbamate)] (MBDDC) were arranged by IOCL, paraffinic oil having profile of viscosity (40 cP at 25°C, 12cP at 40°C and 3-4cp at 100°C) were used in all experiments.

Micron sized MoS₂ and respective dispersants in various weight ratios were milled in a Retsch PM-400MA planetary ball mill with ZrO₂ balls in ZrO₂ vessels. Paraffinic oil was used as the milling mediums in all the experiments. The whole milling process includes the following three milling steps using different sizes of balls:

1. Milling with 1 mm balls at 1200 rpm followed by sieving to separate the balls from materials.
2. Further milling (sample obtained after step 1) with 0.5 mm balls at 1200 rpm and sieving.
3. Third milling (sample obtained after step 2) with 0.1 mm balls at 1200 rpm and sieving.

Vibratory sieving was performed in a 3D sieve shaker (AS 200 of M/s Retsch) to separate the balls from the sample only after milling. During sieving, it was ensured that no solid particles were left by increasing the amplitude of vibration. Different sizes of sieves were used to separate different ball sizes (mentioned in Table 5.1 below).

Table 5.1: Sieve sizes used while separating the balls from sample.

S.No	Sieve hole size (μ)	Ball size (mm)
1.	600	1.00 \pm 0.12
2.	300	0.50 \pm 0.08
3.	70	0.10 \pm 0.01

The duration for each milling step was fixed at 3 hours. The details of the milling process parameters are in Table 5.2.

Table 5.2: Milling parameters.

Weight ratio of MoS ₂ and selected (exfoliating/ surface stabilizing agent)/ additive.	1:2
Lecithin : ZDDP/ MBDDC	1:2, 2:1
Total volume of milling vessel	500 ml
Volume of ZrO ₂ balls (1mm/0.5 mm/0.1mm ϕ).	125 ml
Rotating speed	1200 rpm
Milling time	3 hr

The samples prepared are represented in Table 5.3 by alphanumeric characters in which the first two digits represents the weight ratio of selected exfoliating/ surface stabilizing agent [Lecithin (L)] and AW additive [ZDDP (Z) or MBDDC (V)] followed by solid MoS₂ (M). For instance, 12LZM is MoS₂ milled in the presence of 1:2 mixtures of lecithin and ZDDP. The ratios mentioned are as used while preparing MoS₂ dispersion in oil.

Table 5.3: Samples description

Sample description	Dispersant	Ball fineness up to	% MoS ₂	%Lecithin	% Z (V)
12LZM	L+Z	0.1mm	27.5	18	36(0)
21LZM	L+Z	0.1mm	22	30	15(0)
12LVM	L+V	0.1mm	25	17	0(32)
21LVM	L+ V	0.1mm	24	33	0(17)

5.3. Grease preparation

Base oil and fatty acid (weight ratio 1:1.5), and lithium hydroxide [LiOH (0.1 wt %)] were charged in a reactor and allowed to react at 200°C for 10-15 minutes before bringing down to 90°C as detailed reports about the method can be found in [139]. Prepared MoS₂ nanoparticles were added to the grease product at 90°C with constant and thorough mixing for 20 minutes and homogenized. The amount of nanodispersion in grease composition was taken in such a way to give 2.5 wt% of MoS₂ in the final grease product.

Several sets of samples were prepared by blending nano MoS₂ dispersion (concentration of nano MoS₂ was about 2.5%) with freshly synthesized lithium grease (Li grease). Another set of samples include the base grease, base grease with ZDDP or ashless phosphorus free AW additive or with micron sized MoS₂. The composition of each prepared sample is discussed in Table 5.4 below.

Table 5.4: Effective concentration of MoS₂ and dispersants present in grease sample.

S.No.	Sample	MoS ₂ (%)	Z or V (%)	L (%)
1.	Li grease	0	0	0
2.	Li grease + μ MoS ₂	2.5	0	0
2.	Li grease + 12LZM	2.5	3.3	1.7
3.	Li grease + 21LZM	2.5	1.7	3.3
4.	Li grease + 12LVM	2.5	3.3	1.7
5.	Li grease + 21LVM	2.5	1.7	3.2
6.	Li grease + Z	0	3.3	0
7.	Li grease + V	0	3.3	0

5.4. Characterization and tribological testing of prepared samples

TEM images in Figure 5.1(a-d) show the presence of separated exfoliated sheets of MoS₂ after milling different combination of exfoliating agent / stabilizing agent (lecithin) with AW additives. The diffraction pattern taken from 12LZM sample in Figure 5.1e confirms the hexagonal structure of MoS₂ and the similar pattern was observed for all samples.

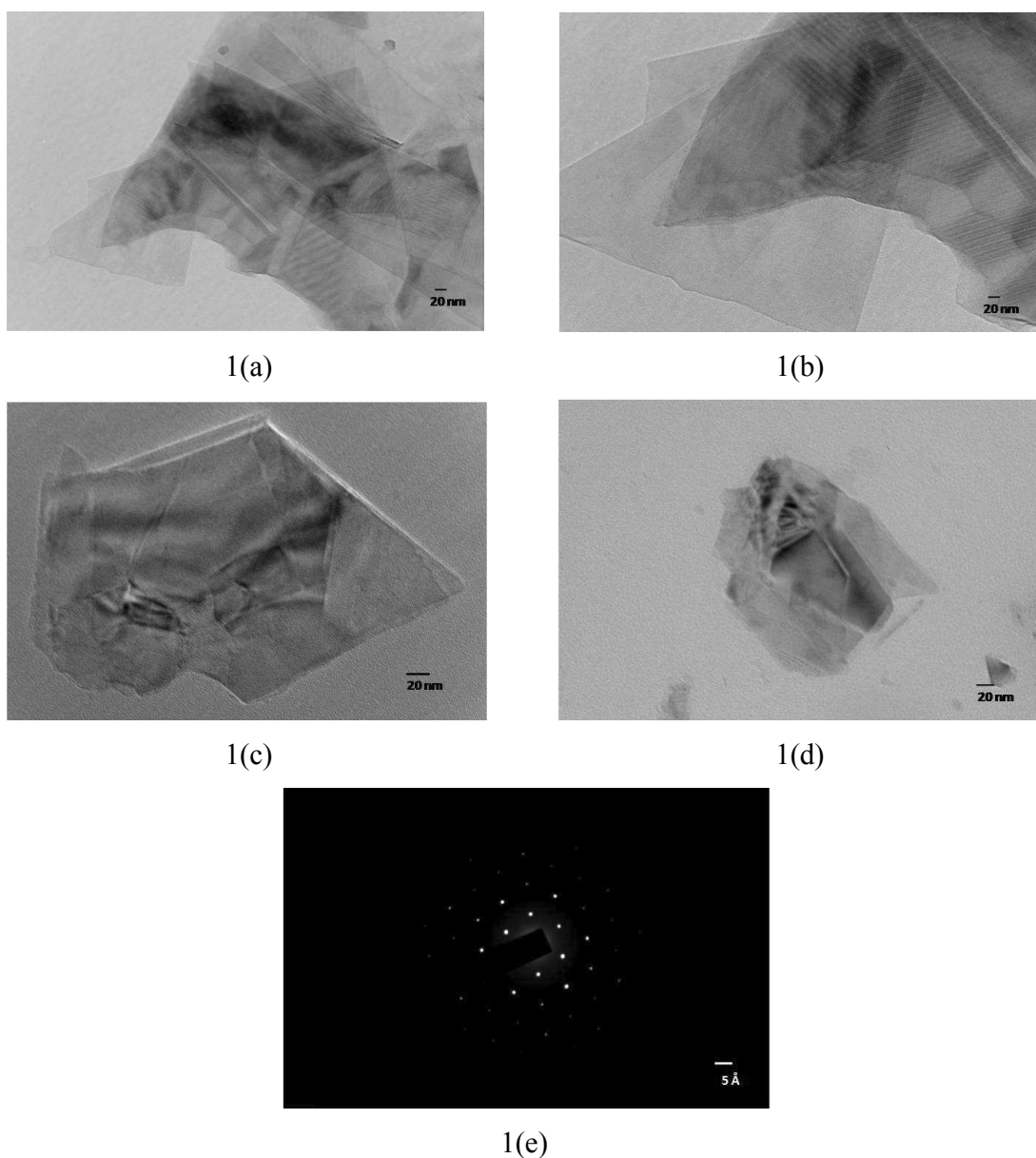


Figure 5.1: TEM images of MoS₂ dispersions containing exfoliated sheets prepared through milling (a) 12LZM, (b) 21LZM, (c) 12LVM, (d) 21LVM and (e) SAED pattern matching with the hexagonal structure of MoS₂.

XRD pattern was recorded for 12LZM, 21LZM, 12LVM, 21LVM samples after ball milling against pure 2H-MoS₂ and molybdenum oxide, in order to check the oxidation of MoS₂ during the milling process in the hydrocarbon medium. No reflections related to molybdenum oxide

were observed in milled samples (Figure 5.2). It is evident from this result that none of the ball milled sample was oxidized.

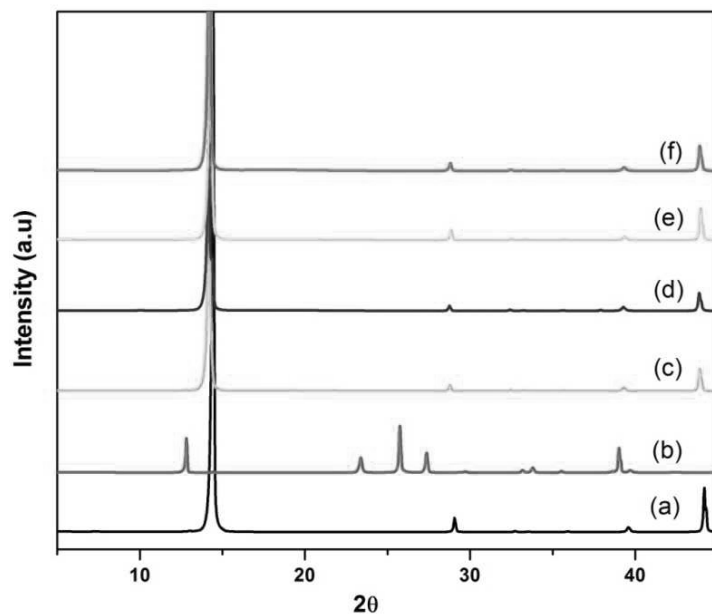


Figure 5.2: XRD plots of (a) 2H-MoS₂, (b) Molybdenum oxide, (c) 12LZM, (d) 21LZM, (e) 12LVM and (f) 21LVM.

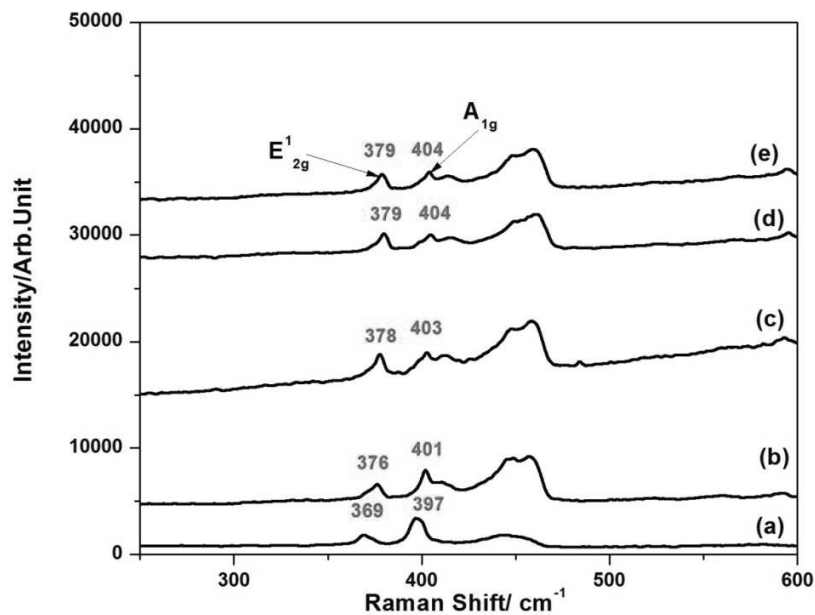


Figure 5.3: Raman spectra of (a) standard MoS₂, prepared dispersions (b) 12LZM, (c) 21LZM (d) 12LVM and (e) 21LVM.

In addition, Raman analysis of the synthesized dispersion supports the exfoliation of MoS₂ into sheets is shown in Figure 5.3. It was found that the intensity of E_{2g}¹ peak increases, while that of A_{1g}¹ peak decreases, which implies the decrease in the number of sheets [140]. Also, a blue shift was observed for the E_{2g}¹ peak from 369 to 379 cm⁻¹ and A_{1g}¹ peak from 397 to 404 cm⁻¹ of the respective samples. The presence of lecithin enhances the exfoliation process as already described in the literature [138].

Table 5.5: Particle size for various ball milled samples.

S.No	Sample	Average major axis (nm)	Average minor axis(nm)
1.	12LZM	715	90
2.	21LZM	819	108
3.	12LVM	733	92
4.	21LVM	4784	393

Table 5.5 shows the sheet size distribution of MoS₂ nanosheets present in the prepared dispersions. The initial particle size of MoS₂ (10μ) was reduced to the sub-micron range after three stages of milling treatment.

The backscattered laser scattering analysis assumes all particles are spherical and it displays the average radius or length of the particles.

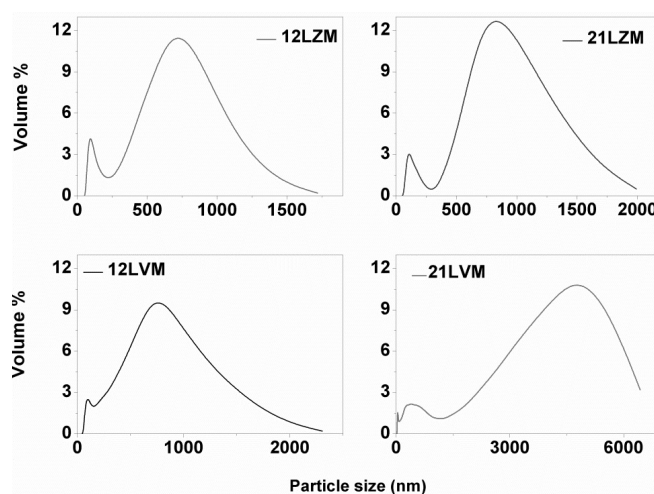


Figure 5.4: Volumetric distribution for various dispersions.

From TEM measurements, it was found that obtained dispersions consist of nanosheets of different length and width. The volumetric distributions are of bimodal distribution with one major axis (the higher one) being the length of the nanosheets, and the smaller one (the minor axis) is the width of the nanosheets as shown in Figure 5.4.

The obtained average nanosheet length of MoS₂ was found to be around 700-820 nm, showing a narrow size distribution for all LZM samples. However, for LVM samples the size distribution was much wider (700-480 nm). This marginal variation in the particle size in the minor axis could be attributed to the viscosity of the medium used during milling. However, the larger sheet length may be due to the difference in dispersion composition, which will be resolved in future work.

Lecithin is the most viscous followed by ZDDP and then MBDDC. The overall effect of viscosity of medium along with the surface tension of the medium affects the exfoliating capability [138]. The average length of the exfoliated sheets measured through TEM [141] is following the same trend as the d₅₀ obtained from DLS.

5.4.1. EP Characteristics

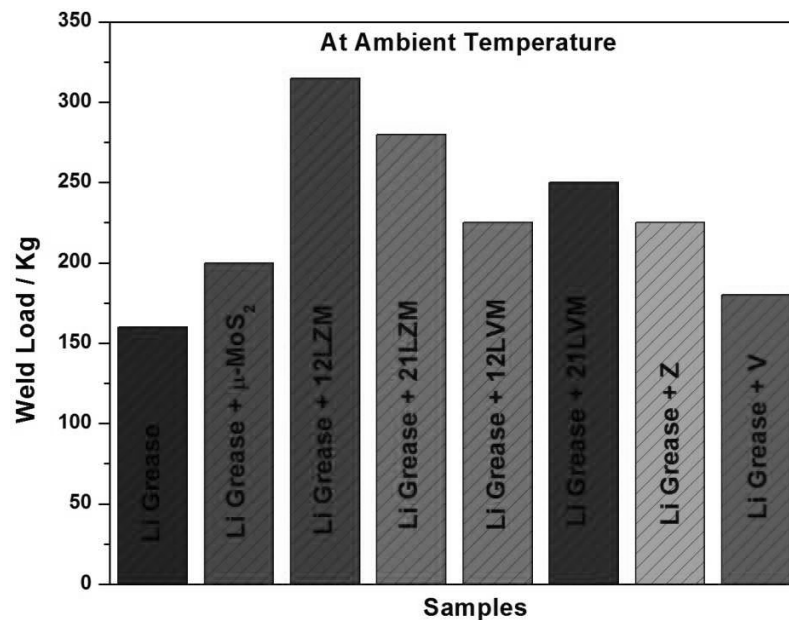


Figure 5.5:EP data for the various samples blended with Lithium grease.

Figure 5.5 shows the EP data for various samples synthesized after homogenizing the fixed ratio of nano MoS₂dispersion into freshly synthesized Li-grease.

The base Li-grease has about 160 kg weld load, whereas substantial improvement can be seen with the addition of nano MoS_2 dispersion along with Z or V. The maximum load bearing of 315 kg was obtained from the sample (12LZM) that has MoS_2 and 1:2 mixtures of lecithin and ZDDP. For the similarly processed sample (21LZM) with higher lecithin content (2:1, lecithin: ZDDP), a marginally lesser weld-load of 280 kg was observed. In contrast, when MBDDC was used, the sample 21LVM exhibited better load bearing capability than 12LVM. Therefore, the observed load bearing capacity in the samples 12LVM and 21LVM was influenced by the amount of lecithin; whereas the amount of ZDDP had the same effect on the samples 12LZM and 21LZM. The marginal difference in the weld load value may be linked with the varied number of exfoliated layers in MoS_2 . In the case of base grease mixed with only MBDDC and ZDDP, ZDDP gave a better weld load.

5.4.2. Wear and Friction Tests

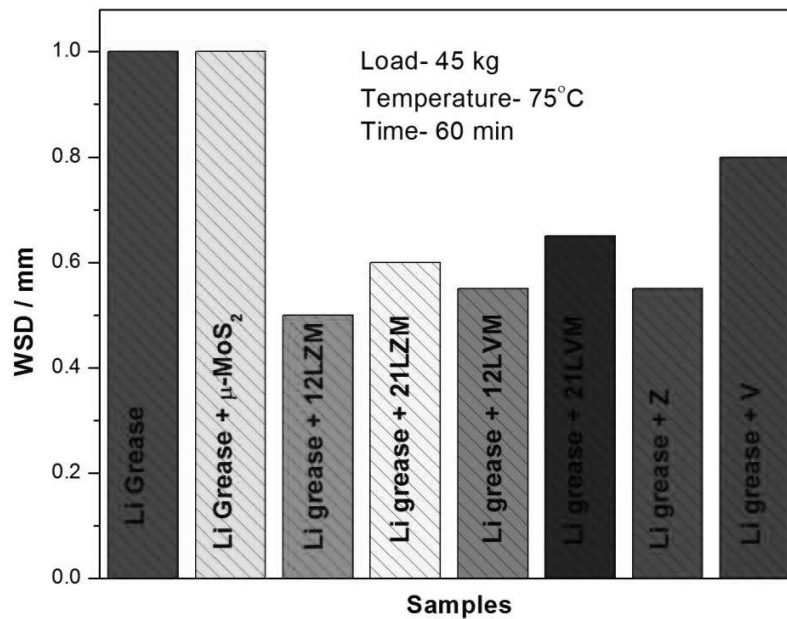


Figure 5.6: Wear data for the various samples blended with Lithium grease.

Figure 5.6 shows the WSDs measurement data for Li-grease containing different MoS_2 additives. The base Li-grease and Li-grease with $\mu\text{-MoS}_2$ samples with no additives produce the largest WSD at 1mm. However, the grease sample blended with only ZDDP or MBDDC develop less wear scar in some cases comparable to nano additive greases (0.55mm). The samples blended

with exfoliated nano-MoS₂ sheets dispersion showed comparatively much smaller WSDs. It should be noted that the samples (Li-grease blended with 21LZM and Li-grease blended with 21LVM) gave marginal wear reduction i.e. between 0.6-0.65 mm, while significant wear reduction was observed for the samples (Li-grease blended with 12LZM, Li-grease blended with 12LVM, and Li-grease blended with Z) giving a similar outcome for WSDs as 0.55mm. ZDDP alone (Li-grease blended with Z) or in combination (12LZM) exhibit good AW property showing the efficacy of P based AW additive.

In comparison of a pair of samples (12LZM and 12LVM) and (21LZM and 21LVM) the samples with ZDDP produce less wear scar. It signifies the effect of ZDDP in comparison to MBDDC. However, excess P is not desirable as evident from the higher WSD value in the sample 21LZM. On the other hand, the addition of lecithin to MBDDC blends improved AW property due to the P content (12LVM).

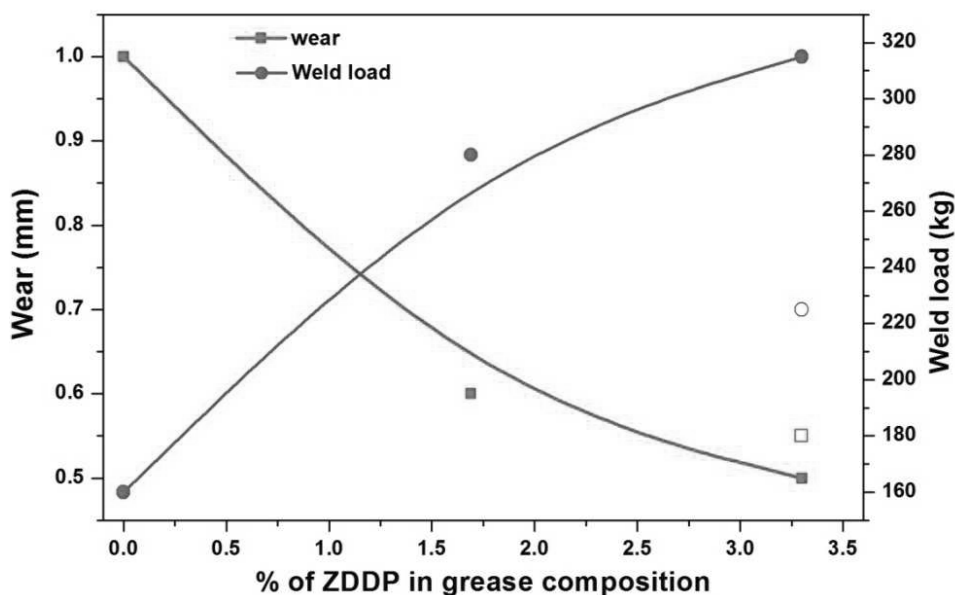


Figure 5.7: Wear and weld load trend of the grease samples that with varying concentration of ZDDP.

The wear and weld load trends of the grease samples show that wear value decreases while weld load value increases with increasing concentration of ZDDP in the presence of lecithin moiety. However, at same concentration of ZDDP (3.3%) in Li-grease composition without lecithin the observed wear value was nearly the same, whereas the weld load value was found to be much smaller. The phosphorous concentration in the latter case was low and it is desirable for good

AW behavior, whereas EP property was affected and hence low weld load was observed. It indicates that, at high ZDDP concentration, lecithin molecules behave synergistically along with MoS₂ nanosheets, as depicted in Figure 5.7.

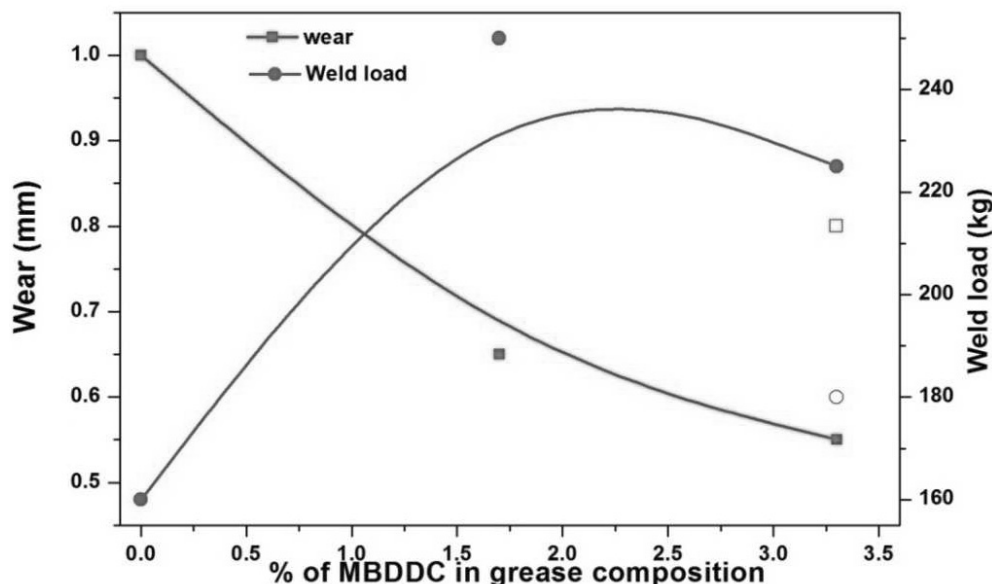


Figure 5.8: Wear and weld load trend of the grease samples that with varying concentration of MBDDC.

On the other hand, with increasing MBDDC concentration in the Li-grease samples wear value decreases and weld load value remains nearly constant in the presence of lecithin moiety. However, the grease with same MBDDC concentration (3.3%) in the absence of lecithin yielded wear and weld load value nearly the same. It indicates that at high concentration of MBDDC, lecithin molecules do not have much contribution and MoS₂ nanosheets nor does it behave synergistically nor antagonistically with other moieties (Figure 5.8); possibly due to the affinity of both for the same surface.

All the above permutation of MoS₂ nanosheets with different AW additive at various concentrations concludes that addition of MoS₂ nanosheets helps in improving the load-bearing tendency of the Li base grease; whereas addition of MBDDC merely improves the EP property compared to other samples as indicated by the weld load result of 12LVM.

Further, it emerged that Li-grease blended with MoS₂ nanosheets (12LZM) is the most desirable formulation to be further explored.

The friction test was performed for the sample (Li-grease blended with 12LZM) at different loads for a fixed period of interval (60 minutes) at 50°C under varying loads (Figure 5.9). A reduction in CoF from 0.13 to about 0.1 after 60 minutes was observed at 300N load. MoS₂ is a well-known friction modifier, thus addition of MoS₂ nanosheets in dispersion leads to the decrease in friction with increased load bearing tendency [66].

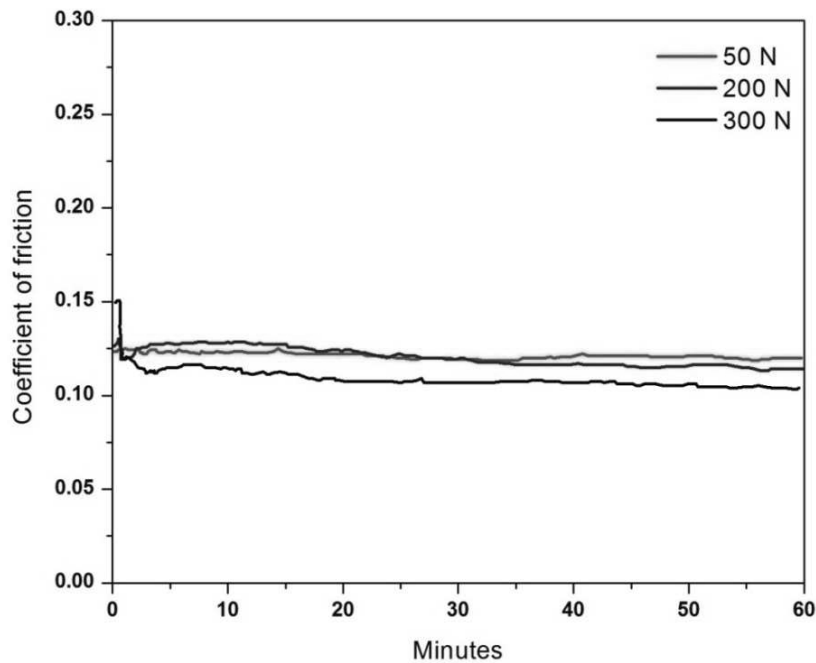


Figure 5.9: Coefficient of friction for Sample (Li grease + 12LZM) at different loads at constant temperature.

The slight reduction in CoF with increasing load is due to the efficacy of MoS₂ nanosheets to reach and work in the asperity zone for wear reduction and reduction in CoF at high loads.

The higher applied load facilitates MoS₂ nanosheets to flow more easily through the asperities existing on the rubbing surfaces. The contact between the asperities is prevented, possibly by the formation of a thin, runny film containing MoS₂ nanosheets that keeps the rubbing surfaces completely apart and thus reduces the friction between them [66].

MoS₂ nanosheets, along with phosphate in the asperity zone, may create a glossy phosphate and synergistically MoS₂ nanosheets comes to the asperity in the disc takes care of the EP property in the steel on steel lubrication.

5.4.3. SEM and EDS analysis of the Worn Surfaces

The samples were selected on the basis of their EP and WSD performances for SEM analysis.

Figure 5.10 shows the SEM images of worn surfaces of the stationary steel balls tested for Li based grease (Figure 5. 10 a1) and with different combinations of additives (Figure 5.10 b1,c1). The base grease gave the largest scar, while addition of near MoS₂ nanosheets with other AW additives leads to reduction in scar diameter.

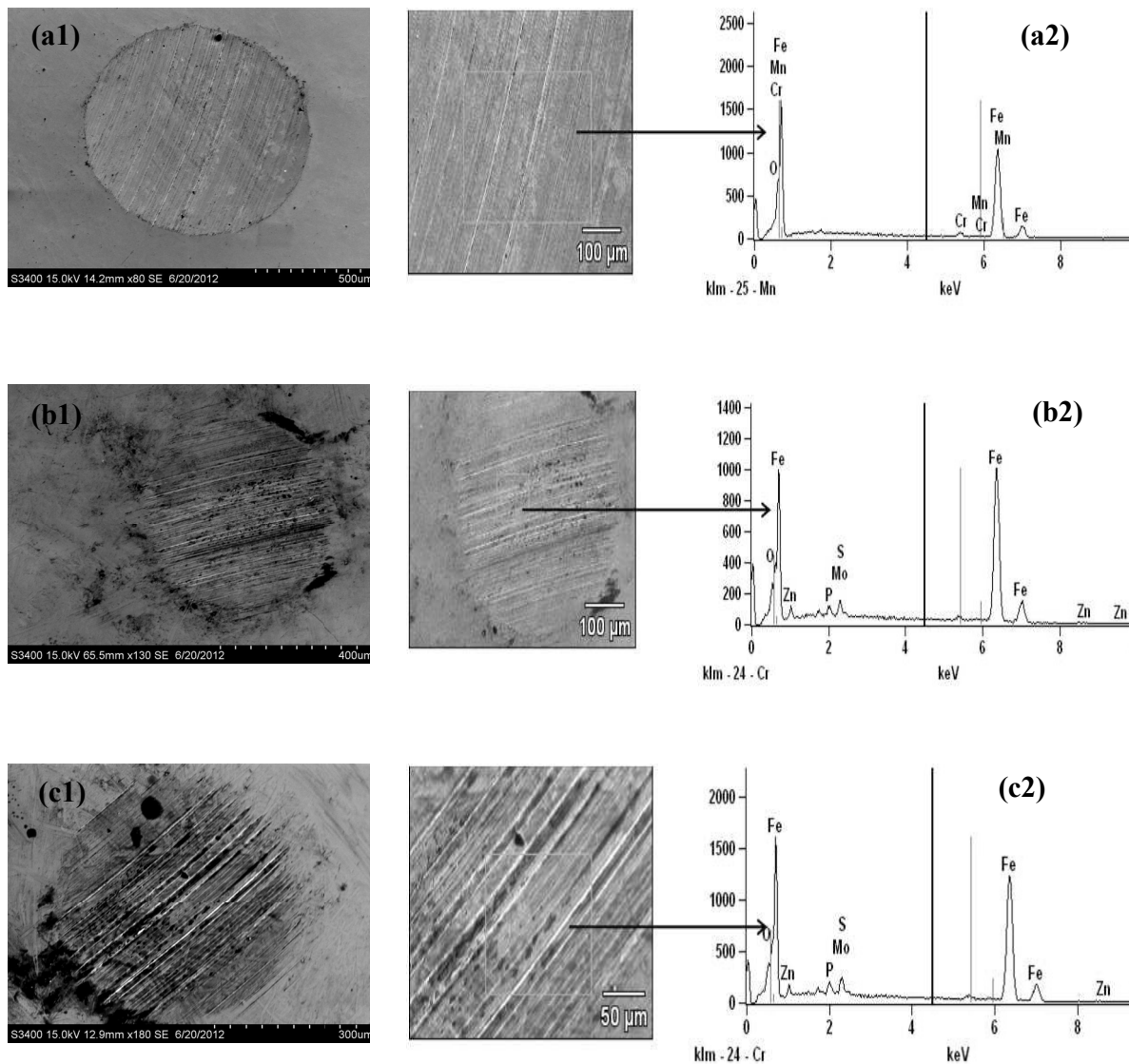


Figure 5.10: SEM images of the wear scar surface on the stationary steel balls tested with (a1)base Li grease, (b1) Li grease+12LZM and (c1)Li grease+21LZM. Figure 8(a2, b2, c2) displays the corresponding EDS pattern taken from the respective wear surfaces.

The qualitative elemental composition of the wear tracks obtained from EDS is given in Table 5.6. The wear track of balls tested with additive added grease contains P, S, Zn and Mo, in addition to Fe, unlike the ball tested with neat base grease. It is a well known aspect of ZDDP and MoS₂ combination that tend to form a durable phosphate based tribofilm layers contain incorporated MoS₂ fragments over the surface of the balls during rotation [142, 65, and 143]. There is a varying degree of roughness found on the track of Figure 5.10 (b1 and c1) compared to Figure 5.10 (a1). This indicates a minimum initial wear proceeds on the surface of the balls until elemental (S, P, Zn & Mo) incorporation in the form of sulphide/ phosphate occurs, which resists further surface wear. The amount of Zn (0.8%) present on the surface remains the same irrespective of the amount of ZDDP used whereas there was an increase of P (1.1%) content, which is higher than Li-grease blended with 12LZM (Li-grease+12LZM) (Mo- 2.3% and P- 0.6%). The observed higher P was due to the higher amount of lecithin in Li-grease+21LZM and Mo was also present more in this case on the wear track. This is due to the synergism between MoS₂ nanosheets, ZDDP and lecithin in tribofilm. It is also known that molybdenum in phosphate-based tribofilm exists in the form of MoS₂, not as oxygenated molybdenum compounds [68].

It is also evident from the percent oxygen composition detected on the surface of steel balls (Table 5.6) decreases due to tribofilm formation. To check the ambiguity in semi-quantitative analysis, standard samples were run in EDS and all the analysis was performed in a single stretch.

Table 5.6: EDS analysis for different sample after four-ball test.

S.No	Sample	Elements (%) from semi quantitative analysis				
		O	P	S	Zn	Mo
1.	Balls(Li grease)	2.3	0
2.	Balls (Li grease+12LZM)	1.7	0.6	0.3	0.8	2.3
3.	Balls (Li grease+21LZM)	1.9	1.1	0.2	0.8	2.3

There is only a marginal difference observed in WSD with Li-grease blended with 21LZM (Li grease+21LZM) (0.60) and Li-grease blended with 12LZM (Li-grease+12LZM) (0.55) despite the presence of qualitative varying amounts of Mo and P on the track. This indicates that AW contribution from Mo and P is negligible, indeed Zn alone resists wear as is evident from the observed minimum WSD (0.55) with Li-grease blended with Z (L+Z). Nevertheless, load-bearing ability requires the combination of Mo and P with Zn on the surface. The weld load study confirms the best weld load result (315 kg) observed with Li-grease blended with 12LZM (Li-grease+12LZM). This could be attributed as a synergy between Mo, lecithin and ZDDP where P contributions from both the molecules are in the ratio of (0.2:2).

5.4.4. Raman analysis of the Worn Surfaces

Figure 5.11 shows dispersive Raman spectra from the selected area on the wear track of balls from base grease, 12LZM and 21LZM (Figure 5.11 (a, d, e)). There are two strong stroke shifts observed at 383.5 and 407.8cm^{-1} corresponds to 2H-MoS_2 E_{2g}^1 and A_{1g} modes [144, 145].

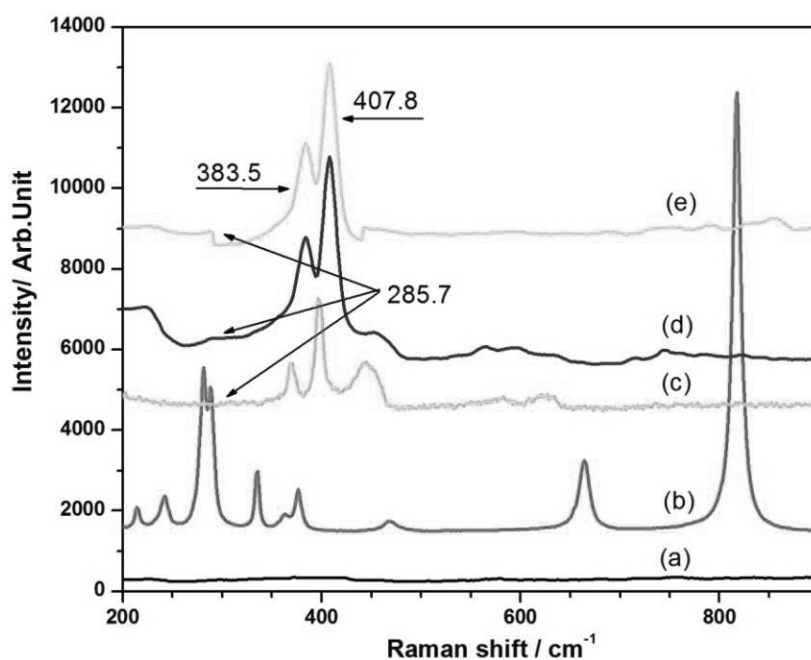


Figure 5.11: Raman spectra of standard molybdenum compounds and worn surfaces in balls after four balls test.

The less intense peak observed around 285.7 cm^{-1} was also a characteristic line from MoS_2 (Figure 11(c)) [146]. This confirms that reduction in wear scar was due to the tribofilm formation with MoS_2 nanosheets and confirms the presence of MoS_2 in between the rubbing

surfaces. However, the presence of P in the wear surface has not been visualized through Raman spectroscopy although same has been qualitatively visualized by EDS in a considerable amount. Raman excitation from pure molybdenum oxide (Figure 5.11 (b)) is also given for reference and shows peaks at 281, 287, 334.9, 376.9, 663.9, and 817.9 cm^{-1} . On comparing the spectral features of molybdenic oxide with the worn surfaces data, no raman excitation was found to be related to molybdenum oxide and thus demonstrates that surface passivated MoS_2 nanosheets are not oxygenated under tribochemical conditions.

5.5 Conclusions

MoS_2 nanosheets synthesized by ball milling technique with oil, dispersant and AW additives helps to improve the AW, anti-friction and EP properties of Li-grease. SEM analysis of the wear track demonstrates that the wear scar surface is much smoother and smaller in diameter than that of base grease. The formation of tribo film is supported by the elemental composition analysis on the surface. Raman spectra also confirm the presence of MoS_2 over the surface of steel ball after the four-ball test. Exfoliated MoS_2 nanosheets functionalized by ZDDP and lecithin demonstrate substantial improvement in tribological properties of the base grease.

This study shows that inorganic layered nanosheets of MoS_2 exfoliated, and chemo-mechanically stabilized, with P containing organic surface stabilizing/exfoliating agent (lecithin) and AW additive (ZDDP), give significant improvement in lubricant performance and tribological properties.

High-efficient production of boron nitride nanosheets via an optimized ball milling process and their tribological studies

6.1. Introduction

BNNSs have many unique characteristics such as a wide band gap, environmentally benign, inert to most chemicals and the ability to lubricate in extreme temperatures. They possess superior thermal stability and adherence properties that present an opportunity to formulate new solid lubricants with BN, for applications where conventional materials perish and fail to deliver the desired performance. It is also considered as a green lubricant additive after being evaluated for its tribological properties in water dispersion [147].

BNNSs can be produced in a bottom-up or top-down manner. The bottom-up method includes chemical vapour deposition[148-150], chemical reaction[151] and segregation method[152]; and the top up is mainly exfoliation of bulk h-BN crystals via mechanical [91, 102,153] or chemical methods [154]. It has been demonstrated that tailored wet ball milling is an efficient and high yield method to produce atomically thin BNNSs of high crystallinity [102]. Among water, ethanol, dodecane and benzyl benzoate milling agents, benzyl benzoate gives rise to the best peeling results, due to its relatively high density and similar surface energy to h-BN. The peeling efficiency or nanosheet yield by ball milling can also closely relate to many other milling parameters, such as ball size, milling speed and ball-to-powder ratio, which have not been investigated. Here, we carefully studied various milling parameters for optimized production of large quantities of BNNSs in benzyl benzoate by ball milling. We also study the effect of h-BNNSs on lubricating properties of base oil.

6.2 Experimental work

A standard amount (0.5 g) of h-BN powder (PT110, Momentive) and 10 ml benzyl benzoate (purity $\geq 99\%$ Sigma-Aldrich) were milled in a horizontal planetary ball mill (Pulverisette 7, Fritsch) using steel vials. The vials were sealed and filled with argon (Ar) gas, at a pressure of 200 kPa above atmospheric pressure, to avoid environmental contamination. The milling speed was varied (600 and 800 rpm) with different powder to ball ratios (1:10, 1:20 and 1:50) for up to

10 h. At different time intervals (0.5, 1, 2, 5 and 10 h), a small amount of sample was removed from the vials for analysis.

6.2.1. Yield estimation of h-BNNSs

To estimate the production yield of nanosheets, ball milled samples (2-3 mL) were mixed with benzyl benzoate (5-10 mL) followed by bath sonication for 15 minutes and centrifugation at 800 rcf for 60 minutes. The supernatant containing nanosheets was separated from the settled large particles. Supernatant and settled particles were filtered over a membrane (0.45 µm pore sized) with the help of a vacuum pump. Membrane containing nanosheets and large particles were dried and weighed to calculate the percentage yield:

$$Percentage\ yield = \frac{weight\ of\ nanosheets}{total\ weight} \times 100$$

Total weight = weight of nanosheets + weight of weight of large particles.

6.3. Effect of milling on h-BNNSs production

6.3.1. Milling time effect

The starting h-BN particles have a characteristic disc-like shape with diameters of 10-20 µm and a thickness less than 100 nm, as shown in the SEM image in Figure 6.1a. The study of milling time effects on BN peeling was based on 1mm steel balls with a ball-to-powder weight ratio of 10:1 at a milling speed of 800rpm in benzyl benzoate. According to SEM studies, most of the h-BN particles become delaminated after 2 h milling. Figure 6.1(b and c) show partially exfoliated h-BN particles caused by the impact from the milling balls, which predominately produce shear force during milling. Under the shearing force, the weak interplane bonds break and thinner BN sheets can be produced. However, the yield of few-layer BN is still low at this (2 h) stage. With the extension of milling time to 5 h, the exfoliation is more complete, as shown in Figure 6.1d that there are more BNNSs than BN particles. After 10 h milling, the yield of BNNSs further increases, but the size of the BNNSs is slightly reduced compared with that of the 5h milled BNNSs. This indicates that certain milling time is required to allow the complete exfoliation of BN, but extended milling should be avoided to reduce damage on BNNSs. In this particular case, 10 h milling is the optimum milling time.

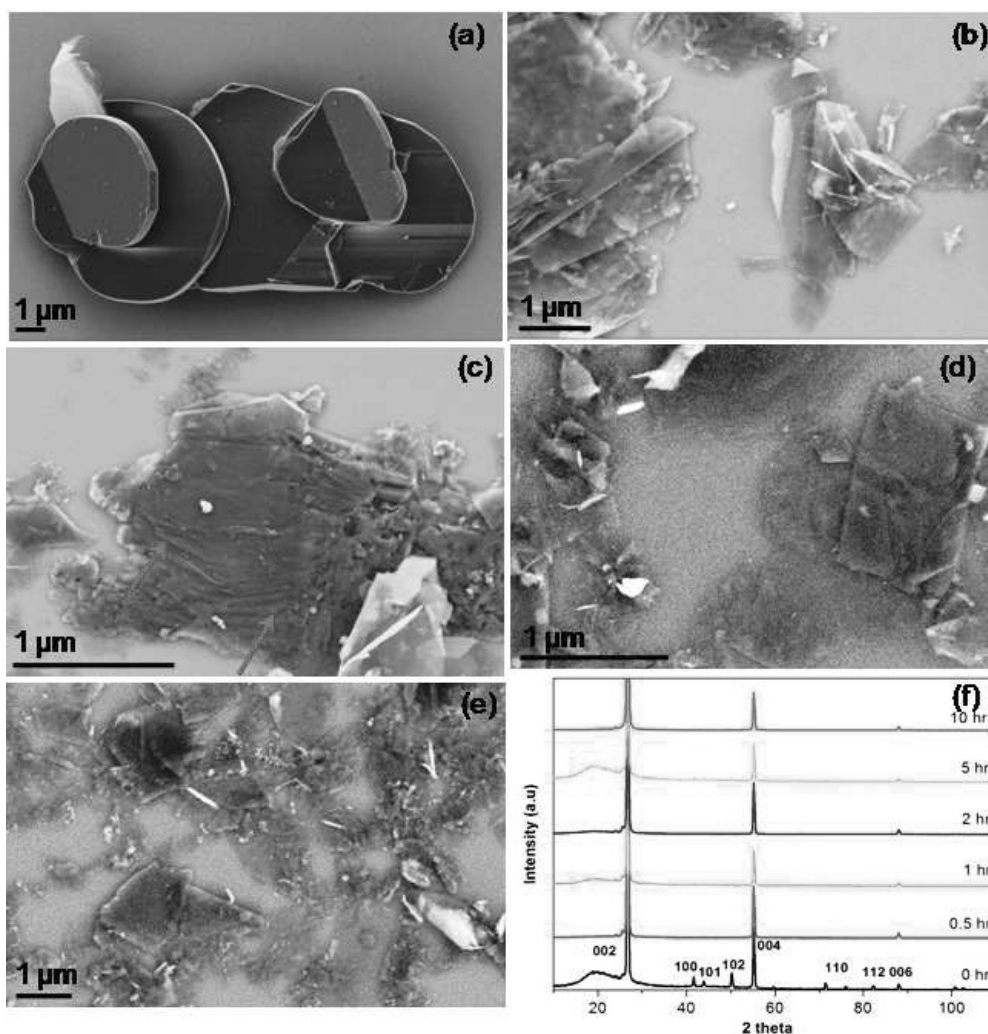


Figure 6.1: SEM images of (a) starting h-BN particles, (b, c) partially exfoliated h-BN particles after 2h milling, (d) more exfoliated particles after 5h milling, (e) completely exfoliated particles after 10h milling, and (f) normalized XRD spectra of the initial h-BN particles and the sheets ball milled for different periods of time without centrifugation.

Figure 6.1f shows the normalized XRD spectra of the BN milled for different periods of time. The starting particles show a typical XRD spectrum from h-BN with strong (002) and (004) peaks. Even after 10 h milling, the relative intensities of the (004) and (006) only slightly decrease and there is no measurable broadening of the (002), (004) and (006) peaks. These suggest that the milling has a small impact on the in-plane structure of BN. The (100), (101), (102), (110) and (112) peaks, in contrast, almost disappear after 0.5h milling, which is caused by the preferential orientation of milled BN on the substrate attributed to their reduced thickness-to-size ratio. Therefore, the milling effectively exfoliates BN to thin sheets.

6.3.2. Ball-to-powder ratio effect

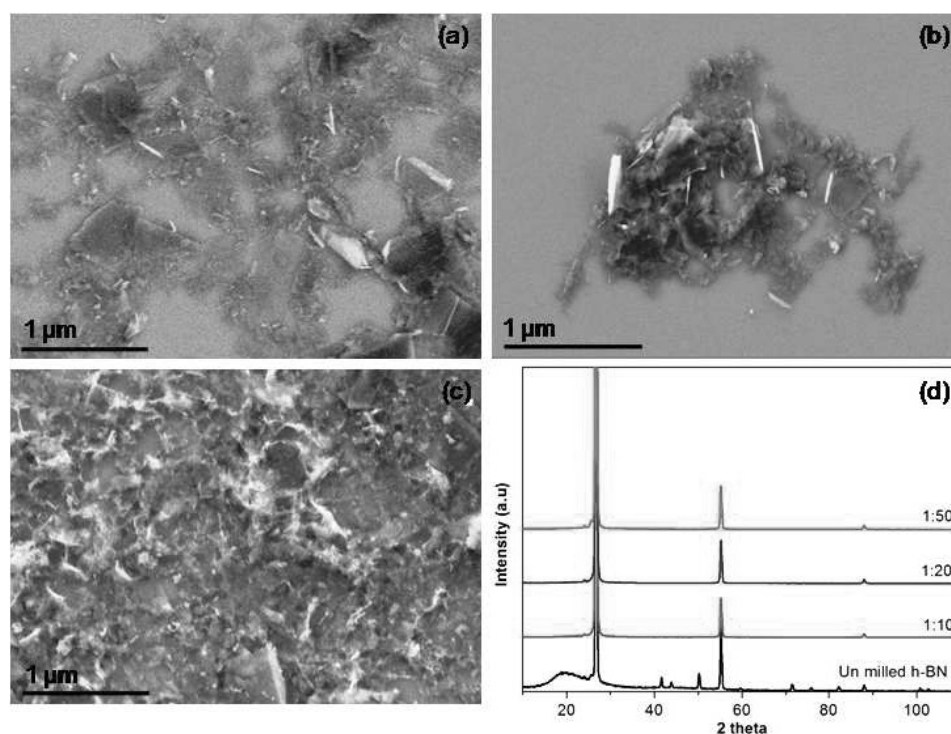


Figure 6.2: SEM images for sample ball milled with different ball / powder ratio (a) 10:1, (b) 20:1, (c) 50:1 and (d) normalized XRD spectra of the initial h-BN particles and the sheets ball milled with different ball / powder ratio without centrifugation.

The milling effect of various ball-to-powder weight ratios was investigated using 1 mm steel balls for a milling time of 10 h. Compared to the results from the ball-to-powder ratio of 10:1, similar amount of BNNSs are produced when the ratio increases to 20:1 (Figure 6.2a). However, the 20:1 ratio produces more BNNSs of less than 200 nm in diameter. When the 50:1 ratio is applied, numerous particles, rather than sheets, are found. These particles are due to wrapping or damage to BNNSs [155]. This indicates that the increase of ball-to-powder ratio can result in higher yield of sheets but at the cost of more damage to the BNNS, owing to a higher chance of ball-to-vial or ball-to-ball collision and possibly stronger collision. The XRD patterns of samples milled with the different ball ratios are similar and no noticeable broadening of the (002) and (004) peaks for all three samples (Figure 6.2c). Therefore, the ideal ball-to-powder ratio is 10:1.

6.3.3. Milling speed effect

Milling speed is another important parameter. The milling speed was reduced to 600rpm with optimized conditions (a milling time of 10 h and ball-to-powder ratio of 10:1). The amount of BNNSs produced at 600 rpm is close to that produced at 800 rpm, but 600 rpm produced sheets are thicker and larger in size (Figure 6.3a) due to the smaller shear force created by the balls and hence less exfoliation.

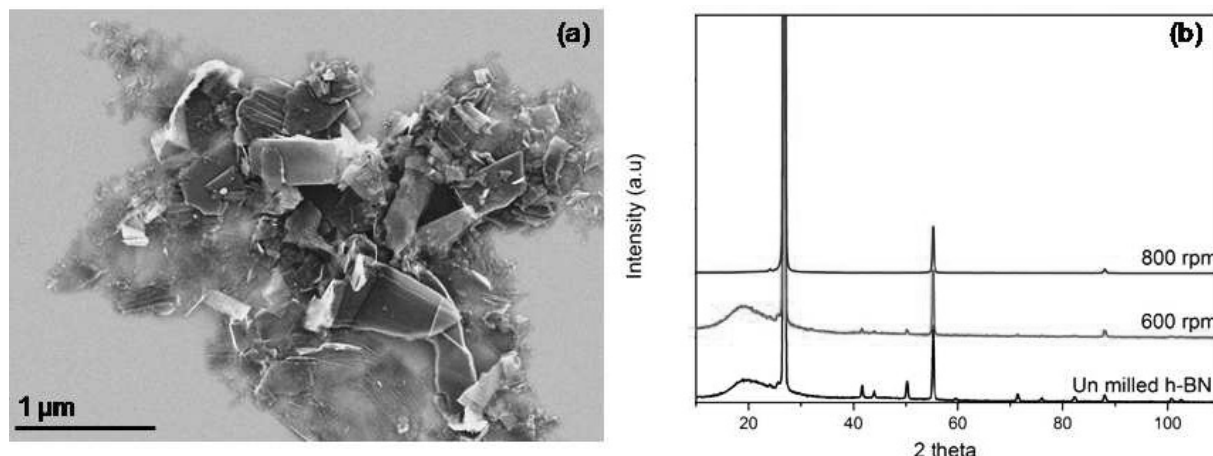


Figure 6.3: SEM images for sample ball milled with different milling speed (a) 600 rpm, (b) normalized XRD spectra of the initial h-BN particles and the sheets ball milled with different milling speed without centrifugation.

The XRD characterization (Figure 6.3b) reveals that the intensities of (004) and (006) peaks decrease with the increase of milling speed, suggesting more change to the c-direction of BN crystal and therefore more thickness reduction. In addition, the (100), (101) and (102) peaks are still visible after 600 rpm milling, whereas these peaks disappear for the sample milled at 800 rpm. This indicates that the 600 rpm milled sheets have a smaller size-to-thickness ratio and hence less effective exfoliation.

6.3.4. Ball size effect

The effect of ball sizes (1, 0.6-0.8 and 0.1-0.2mm) on the extent of exfoliation was also studied by keeping other milling parameters the same (milling time of 10 h, ball-to-powder ratio of 10:1 and speed of 800rpm). SEM analyses reveal that the 0.6-0.8 mm balls produce similar amounts of BNNSs (Figure 6.4a). However, when the 0.1-0.2 mm balls are used, the yield of BNNSs dramatically increases and their thickness is smaller and more homogeneous (Figure 6.4 (b and c)). This result is not surprising by considering the greater surface area and lighter weight of 0.1-

0.2 mm balls, compared to those of 0.6-0.8 or 1 mm balls. The larger surface area can create more chance of ball-to-ball or ball-to-wall interaction/impact and therefore more shearing on the BN. In addition, their lighter weight makes the shear force gentler so that damage on BNNSs is minimized. The XRD patterns from samples produced by different sized balls are compared in Figure 6.4d.

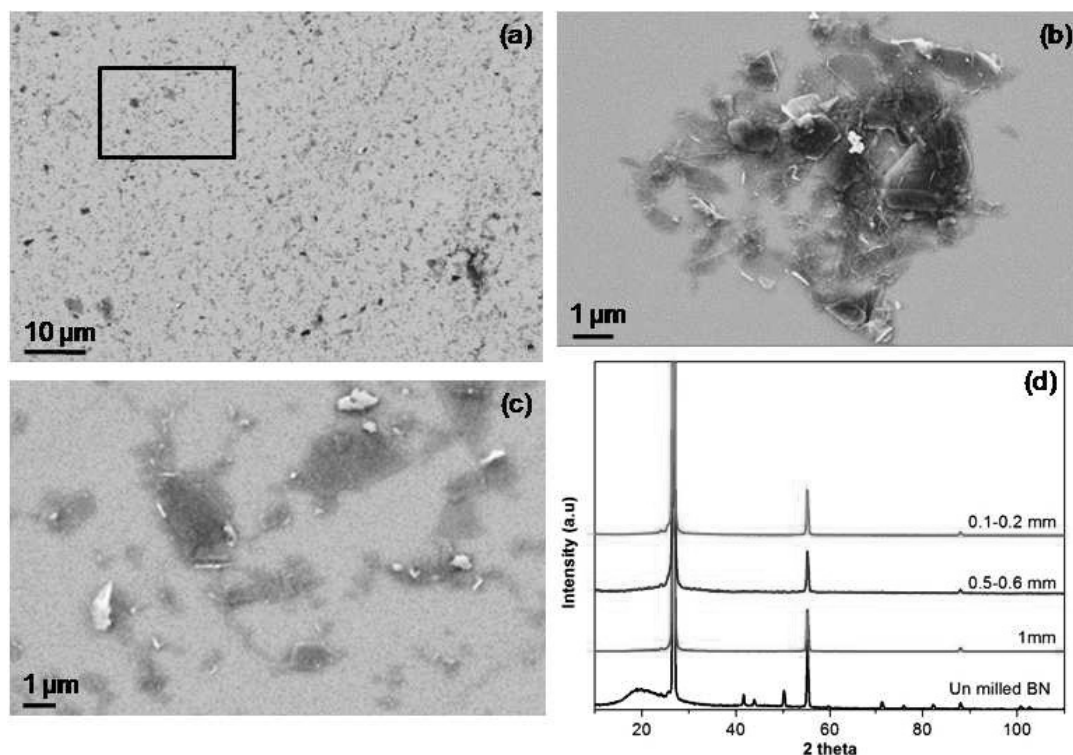


Figure 6.4: SEM images of sample ball milled with different ball sizes (a) 0.6-0.8 mm (b) 0.1-0.2 mm, (c) higher magnification of selected area (indicated as box) from image “a”, and (d) normalized XRD spectra of the initial h-BN particles and the sheets ball milled with different ball sizes without centrifugation.

To confirm that the 0.1-0.2 mm balls give the best exfoliation, we estimated the production yield of all above-mentioned samples using different milling conditions. It is the 0.1-0.2 mm balls with 800 rpm and ball-to-powder ratio of 10:1 that give rise to the highest yield of 13.8%. The milling with 0.1-0.2 mm balls at 600 rpm has slightly lower yield of 13.0%. These yield values are several times larger than those using 1mm or 0.6-0.8 mm balls.

The crystallinity, thickness and chemical composition of the milling produced BNNSs by 0.1-0.2 mm balls are investigated by TEM and EELS (electron energy loss spectra). Figure 6.5a shows

a BNNS suspended over a wholly carbon supporting film on a TEM grid. Folds and partial exfoliation are observed, which is similar to many other investigated BNNSs. The electron diffraction pattern in Figure 6.5b shows one set of bright dots and several sets of weaker dots both of a six-fold symmetry. This suggests that the BNNS is still crystalline and the in-plane structure is not damaged, consistent with the XRD results.

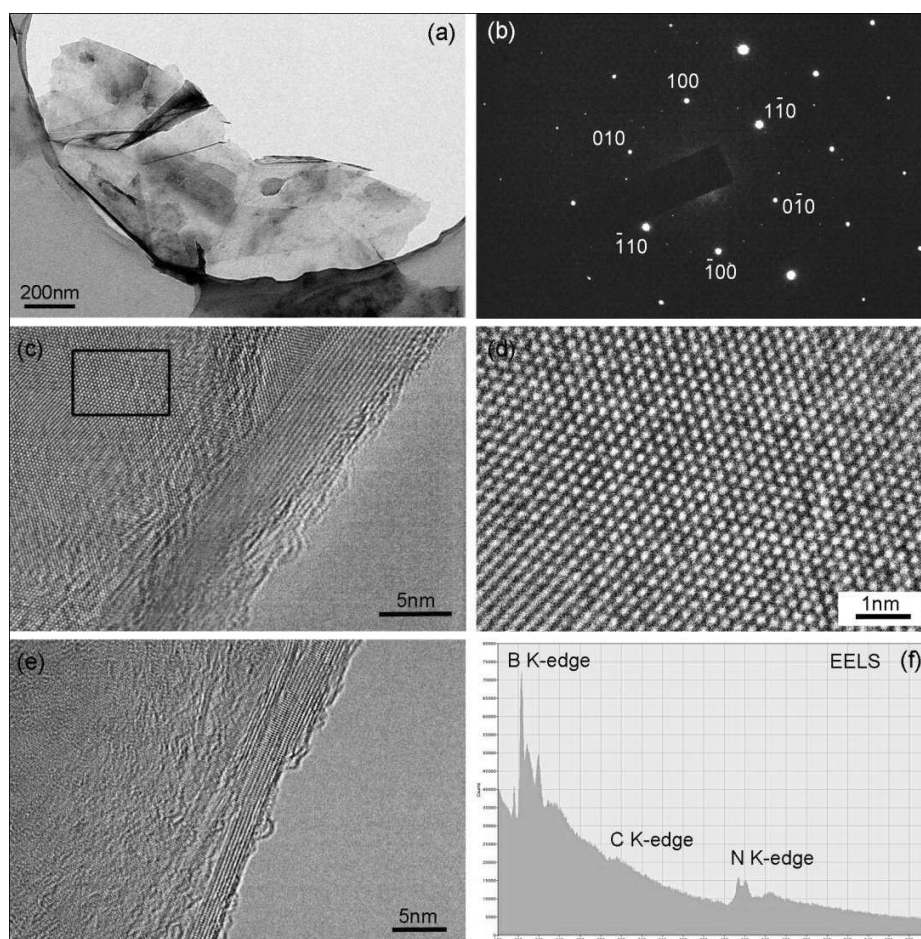


Figure 6.5: (a) TEM Images of the BN sheets obtained, (b) the corresponding SAED pattern, (c) and (d) high-magnification TEM images, (e) and (f) TEM images of a monolayer and a bilayer BNNS and (g) EELS spectra of the BNNS.

The presence of the sets of weaker diffraction dots suggests the stacking of the BNNS is twisted, or there are folds or incomplete exfoliation. A high-resolution TEM (HRTEM) image in Figure 6.5c shows the edge of part of the BNNS, indicating a thickness of 2 nm (~6 layers). The highly crystalline nature of the BNNS is confirmed by the HRTEM image in Figure 6.5d, showing a pattern of lattice dots with a distance of 0.25 nm, representing the distance between two adjacent

BN hexagonal rings. Therefore, the distance between B and N atoms is calculated to be 0.144 nm, typical for h-BN crystals. We also find a monolayer and bilayer BN, as shown in Figure 6.5 (e and f). The EELS spectrum in Figure 6.5g shows predominately B and N, along with a small amount of carbon. The carbon could come from the residue of benzyl benzoate, which is not fully evaporated during the TEM sample preparation.

6.4. Tribology studies

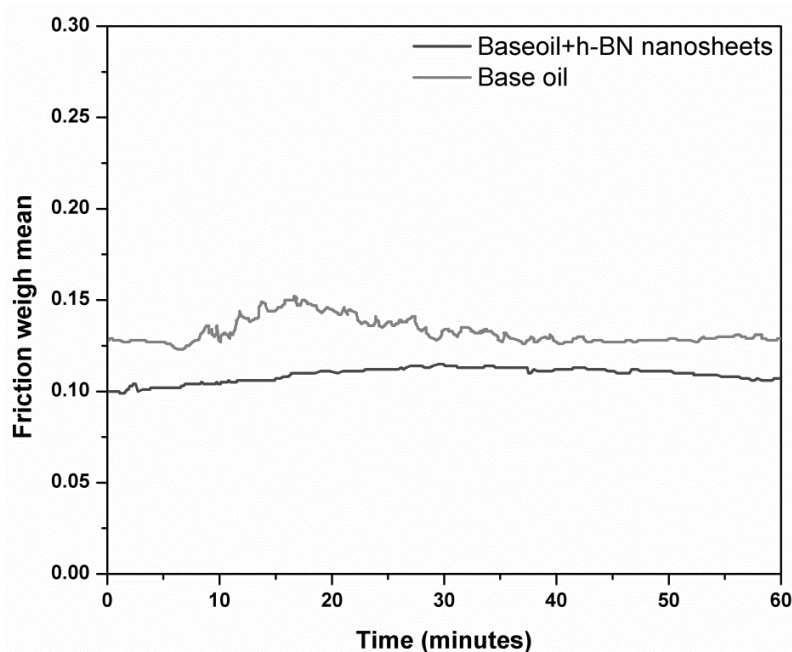


Figure 6.6: Coefficient of friction for Sample (base oil, base oil-BN nanosheets) at fixed load and constant temperature.

Figure 6.6 shows the plot of friction of coefficient versus time of neat base oil and base oil containing h-BNNSs under mentioned conditions. Oil containing h-BNNSs has shown lower friction compared to the neat oil and such a drop in friction could be due to the alignment of nanosheets on the metal surface parallel to the direction of motion [105].

Figure 6.7 shows SEM images of worn surfaces of the stationary balls tested for neat base oil and base oil containing nanosheets. The base oil gives the largest scar, of around 1mm, while h-BNNSs blended base oil shows remarkable reduction in WSD (0.5mm).

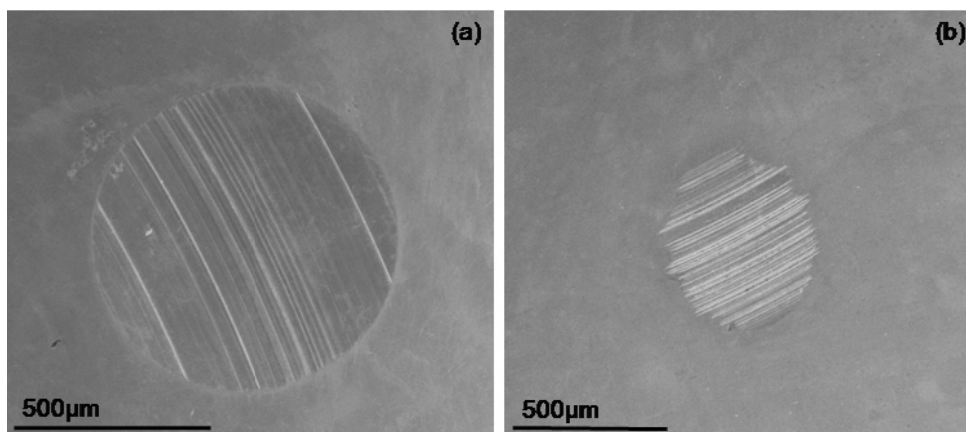


Figure 6.7: shows the SEM images of worn-surfaces of the stationary balls tested for sample (a) neat base oil and (b) base oil with h-BN nanosheets.

This reduction in wear scar is due to the good AW property of h-BN nanosheets. Several mechanisms (e.g. the ball bearing effect, a protective film, the mending effect and the polishing effect) have been invoked to explain the friction reduction enhancement in lubricants that contains nanoparticles [156]. The mending-effect mechanism is considered to be valid for nano h-BN particles because of their layered structure and softness.

6.5. Conclusions

Wet ball milling is highly efficient in BNNSs production with little damage to the in-plane structure. Milling time, ball-to-powder ratio, milling speed and ball size all play important roles in achieving high yields. Under the optimized milling condition and with benzyl benzoate as the milling agent, the production yield is about 13.8% and the BNNSs are 0.5-1 μm with thicknesses of a few nanometres. The resultant BNNSs are of relative high crystallinity and chemical purity. Synthesized h-BNNSs help in reducing the wear scar and CoF of base oil in four-ball tests. SEM analysis of the wear track demonstrates that the wear scar surface is much smaller in diameter than that of neat base oil. This study shows that h-BNNSs when added to base oil give substantial improvement in lubrication.

Conclusions and future work

Conclusions

This thesis has explored the synthesis of inorganic nanoparticles and their application in lubricant technologies. The obtained results indicate that inorganic nanoparticles play a vital and significant role as additives in lubricants and greases. Owing to their hydrophilic nature, the surface of inorganic nanoparticles, i.e. CaCO_3 , MoS_2 , need to be modified in order to be stabilized in oil medium. Therefore, the major work of this thesis was to carry out surface modification of inorganic nanoparticles within oil medium (*in situ*) using capping agents/dispersants through a ball milling process to give nano or near nanometer-sized dispersions. The prepared dispersion was subjected to tribological evaluation to assess its efficacy as a lubricant additive.

Particle size reduction and *in situ* surface modification through (milling route) mechano-chemical bonding of precipitated CaCO_3 nanoparticles with capping agent/dispersant, and their application in lubricant over basing, have not been reported in the literature. Being a new concept, different dispersants were examined for their binding abilities on the surface of CaCO_3 . The surface modification of CaCO_3 nanoparticles using long alkyl chain capping agents renders the surface hydrophobic. The surface coated nanoparticles were characterized using various physiochemical methods and the surface coating thickness was determined by geometric calculations utilizing the results of TEM and TGA analysis. The milling parameters were optimized for the production of SA modified CaCO_3 . Particle size reduction by milling and surface hydrophobicity provided by dispersants, especially SA, enhances the dispersion stability of nanoparticles within the oil medium. The developed CaCO_3 dispersion has potential as a TBN booster in a variety of lubricant formulations.

Likewise, the direct application of MoS_2 in lubricant formulation is limited, due to the dispersibility issues in hydrocarbon/oil media. MoS_2 nanosheets were produced using a unique combination of organic agent (phospholipids (lecithin)) and AW additives through ball milling

treatment. These agents and additives were found to exfoliate bulk MoS₂ to the nanosheets of few layers in addition to prohibit the oxidation of MoS₂ during milling. The obtained MoS₂ dispersion was found to be oil dispersible due to nanosized structure and hydrophobic character. The nanosheets generated through ball milling process have a strained structure and high surface energy, thus chemically linked and coated with AW additive and lecithin to minimize the surface energy. The chemically coated MoS₂ nanosheets are dispersible in oil, homogenized with lithium based grease and were tested for their antifriction and wear resistant properties. An improvement in tribology results was noticed when MoS₂ nanosheets were used and blended with lithium based grease.

The production of high quality nanosheets of h-BN through tailored wet milling has been achieved. h-BN is a well known EP additive and helps in the reduction of wear scar and CoF when blended with base oil during tribology testing. The sheets obtained were highly crystalline and chemically pure with a diameter of 0.5-1 μm and thicknesses of a few nanometers. Substantial improvement was observed in lubricating performance of base oil blended with h-BN nanosheets.

Future work

The synthesis of a core shell structure of CaCO₃ using bifunctional surfactants (like hydroxyl stearic acid) is worth examining in order to increase the coating efficacy and reduce the amount of surfactant used. The coating of calcium hydroxide, instead of carbonate, can also be tested for over basing additive development with these surfactants. Similarly, the synthesis of MoS₂ and BNNSs through exfoliation using ionic liquids is one promising option because of the interesting properties of ionic liquids.

There was a marginal variation in the particle size measurements of nano sheets in the minor axis, which could be attributed to the viscosity of the medium used during milling. However, the larger sheet length may be due to the difference in dispersion composition and this could be resolved in future using acoustic and electro-acoustic particle size measurement methods. The nanomaterials studied in this thesis though are found to be enhancing, as additives, the lubricating properties there are lots of scope to work in transferring the knowledge into larger

scale processes, as bulk scale production and designing of nanomaterials with desirable properties is a challenging task. The study of friction and wear resistance requires knowledge of surface interactions with these additives. This field is rapidly developing, however, most applications that can be realized by exploiting nano tribological ideas are still in the embryonic stage.

In summary, the inorganic nanoparticles as additives enhance the lubricity of base oil, as demonstrated from various tribological evaluations. There is an immense scope for this work to be applied in modern lubricant technology.

References

1. Q. Sunqing, D. Guoxu, J. xiu, G. Chen, Wear and friction behaviour of CaCO_3 nanoparticles used as additives in lubricating oils, *Lubr. Sci.* 12 (2000) 205-212.
2. Q. Wang, X. Zhang, W. Dong, H. Gui, J. Gao, J. Lai, Y. Liu, F. Huang, Z. Song, J. Qiao, Novel rigid poly(vinyl chloride) ternary nanocomposites containing ultrafine full-vulcanized powdered rubber and untreated nano-sized calcium carbonate, *Mater. Lett.* 61 (2007) 1174–1177.
3. Y. Sheng, B. Zhou, J. Zhao, N. Tao, K. Yu, Y. Tian, Z. Wang, Influence of octadecyl dihydrogen phosphate on the formation of active super-fine calcium carbonate, *J. Colloid Interface Sci.* 272 (2004) 326–329.
4. C. Wang, Y. Sheng, X. Zhao, Y. Pan, H. Bala, Z. Wang, Synthesis of hydrophobic CaCO_3 nanoparticles, *Mater. Lett.* 60 (2006) 854–857.
5. M. Fuji, N. Maruzuka, J. Yoshimori, T. Takei, T. Watanabe, M. Chikazawa, K. Tanabe, K. Mitsuhashi, Surface active sites introduced onto calcium carbonate powder by a new surface preparation process, *Adv. Powder Technol.* 11 (2000) 199–210.
6. J.Z. Liang, Evaluation of dispersion of nano- CaCO_3 particles in polypropylene matrix based on fractal method, *Composites Part A.* 38 (2007) 1502–1506.
7. C. Wang, Y. Sheng, H. Bala, X. Zhao, J. Zhap, X. Ma, Z. Wang, A novel aqueous-phase route to synthesize hydrophobic CaCO_3 particles in situ, *Mater. Sci. Eng. C* 27 (2007) 42–45.
8. C. Wang, X. Zhao, J. Zhao, Y. Liu, Z. Wang, Biomimetic nucleation and growth of hydrophobic CaCO_3 nanoparticles with oleic acid in a methanol solution, *Appl. Surf. Sci.* 253 (2007) 4768–4772.
9. X. Ma, Y. Liu, Y. Yu, H. Lei, X. Lv, L. Zhao, S. Run, Z. Wang, The influence of the different modifying agents on the synthesis of poly(methylmethacrylate)-calcium carbonate nanocomposites via soapless emulsion polymerization, *J. Appl. Polym. Sci.* 108 (2008) 1421–1425.
10. J.C Armstead, Precipitated calcium carbonate's particle size, surface treatment affect sealant rheology, *Adhesives age* 40 (2007) 18-22.

11. T.D. Lam, T.V. Hoang, D.T. Quang, J.S. Kim, Effect of nanosized and surface modified precipitated calcium carbonate on properties of CaCO₃/ polypropylene nanocomposites, *Mater. Sci. Eng. A.* 501 (2009) 87–93.
12. Challa S.S.R. Kumar, *Mixed Metal Nanomaterials*, John Wiley & Sons, 3 (2009) 282-83.
13. Y. Chen, X. Ji, X. Wang, Facile synthesis and characterization of hydrophobic vaterite CaCO₃ with novel spike-like morphology via a solution route, *Mater. Lett.* 64 (2010) 2184–2187.
14. C. Wang, C. Piao, X. Zhai, F. N. Hickman, J. Li, Synthesis and character of super-hydrophobic CaCO₃ powder in situ, *Powder Technol.* 200 (2010) 84–86.
15. Y. Zhao, S. Li, L. Yu, Y. Liu, X. Wang, J. Jiao, The preparation of calcium carbonate crystals regulated by mixed cationic/cationic surfactants, *J. Cryst. Growth* 324 (2011) 278–283.
16. S. Mihajlovic, A. Dakovic, Z. Sekulic, V. jovanovic, D. Vucinic, Influence of the modification method on the surface adsorption of stearic acid by natural calcite, *J. Serbian Chem. Soc.* 74 (2009) 1-19.
17. H. Zhang, X. Zeng, Y. Gao, F. Shi, P. Zhang, J.F. Chen, A facile method to prepare superhydrophobic coatings by calcium carbonate, *Ind. Eng. Chem. Res.* 50(2011) 3089–3094.
18. J. Jiang, J. Liu, C. Liu, G. Zhang, X. Gong, J. Liu, Roles of oleic acid during micropore dispersing preparation of nano-calcium carbonate particles, *Appl. Surf. Sci.* 257 (2011) 7047–7053.
19. X. Chena, Y. Zhu, Y. Guo, B. Zhou, X. Zhao, Y. Du, H. Lei, M. Li , Z. Wang, Carbonization synthesis of hydrophobic CaCO₃ at room temperature, *Colloids Surf. A: Physicochem. Eng. Aspects* 353 (2010) 97–103.
20. Y. Dihayati, A.R. Aziz, E.C. Abdullah, Y.C. Leong, S. Harcharan, Encapsulation method for CaCO₃ particles, *Journal of applied sciences* 7 (2007) 2046-2050.
21. L. Du, Y. Wang, G. Luo, In situ preparation of hydrophobic CaCO₃ nanoparticles in gas-liquid microdispersion process, *Particuology* 11 (2013) 421-427.

22. Z. Yang, Y. Tang, J. Zhang, Surface modification of CaCO_3 nanoparticles with silane coupling agent for improvement of the interfacial compatibility with styrene-butadiene rubber (SBR) latex, *Chalcogenide letters* 10(2013)131-141.
23. K. W. Kow, E. C. Abdullah, A. R. Aziz, Effects of ultrasound in coating nano-precipitated CaCO_3 with stearic acid, *Asia-Pac. J. Chem. Eng.* 4(2009) 807–813.
24. L. Xiang, Y. Xiang, Y. Wen, F. Wei, Formation of CaCO_3 nanoparticles in the presence of terpeneol, *Mater. Lett.* 58 (2004) 959– 965.
25. Y. Chen, X. Ji, G. Zhao, X. Wang, Facile preparation of cubic calcium carbonate nanoparticles with hydrophobic properties via a carbonation route, *Powder Technol.* 200 (2010) 144–148.
26. C. Wang, C. Piao, X. Zhai, F. N. Hickman, J. Li, Synthesis and characterization of hydrophobic calcium carbonate particles via a dodecanoic acid inducing process, *Powder Technol.* 198 (2010) 131–134.
27. Y. Sheng, B. Zhou, J. Zhao, N. Tao, K. Yu, Y. Tian, Z. Chen Wang, Influence of octadecyl dihydrogen phosphate on the formation of active super-fine calcium carbonate, *J. Colloid Interface Sci.* 272 (2004) 326–329
28. C. Wang, P. Xiao, J. Zhao, X. Zhao, Y. Liu, Z. Wang, Biomimetic synthesis of hydrophobic calcium carbonate nanoparticles via a carbonation route, *Powder Technol.* 170 (2006) 31–35.
29. H.V Tran, L. D. Tran, H. D. Vu, H. Thai, Facile surface modification of nanoprecipitated calcium carbonate by adsorption of sodium stearate in aqueous solution, *Colloids and Surfaces A: Physicochem. Eng. Aspects* 366 (2010) 95–103
30. Y. Sheng, B. Zhou, C. Wang, X. Zhao, Y. Deng, Z. Wang, In situ preparation of hydrophobic CaCO_3 in the presence of sodium oleate, *Appl. Surf. Sci.* 253 (2006) 1983–1987
31. L. Hu, P. Dong, G. Zhen, Preparation of active CaCO_3 nanoparticles and mechanical properties of the composite materials, *Mater. Lett.* 63 (2009) 373–375.
32. C. Zhang, J. Zhang, X. Feng, W. Li, Y. Zhao, B. Han, Influence of surfactants on the morphologies of CaCO_3 by carbonation route with compressed CO_2 , *Colloids and Surf. A: Physicochem. Eng. Aspects* 324 (2008) 167–170.

33. Z. LiNa, F. J. Dong, W. Z. Chen, In situsynthesis and modification of calcium carbonate nanoparticles via a bobbling method, *Sci. China Ser B-Chem.* 52 (2009) 924-929.
34. Bernotat, Schonert, *Mechanochemistry in Nanoscience and Minerals Engineering* (2008) 103-132
35. A. Devarajan, M. A. Khadar, K. Chattopadhyay, Effect of ball milling on chemically synthesized nanoparticles of CaCO_3 , *Mater. Sci. Eng. A* 452–453 (2007) 395–400.
36. T. Tsuzuki, K. Pethick, P.G. McCormick, Synthesis of CaCO_3 nanoparticles by mechanochemical processing, *J. Nanoparticle Res.* 2 (2000) 375–380.
37. D. Hao, L. Shou-Ci, D. Yan-Xi, D. Cao-Xiang, Mechano-activated surface modification of calcium carbonate in wet stirred mill and its properties, *Trans. Nonferrous Met. SOC China* 17(2007) 1100-1 104
38. W. Wu, S. Lu, Mechano-chemical surface modification of calcium carbonate particles by polymer grafting, *Powder Technol.* 137 (2003) 41– 48
39. E. Yogurtcuoglu, M. Uçurum , Surface modification of calcite by wet-stirred ball milling and its properties, *Powder Technol.* 214 (2011) 47–53.
40. M. Uçurum, E. Yogurtcuoglu, T. Depci, Mechano-chemical surface modification of calcium carbonate with n-decane +stearic acid +water system, *Proceedings of XIIIth international mineral processing symposium*, 625 (2012) Bodrum ,Turkey.
41. G. Caixiang, L. Qingzhu, G. Zhuoming, Z. Guangyao, Study on application of CeO_2 and CaCO_3 nanoparticles in lubricating oils, *Journal of rare earths* 26(2008), 163.
42. L.K. Hudson, J. Eastoe, P.J. Dowding, Nanotechnology in action: Overbased nanodetergents as lubricant oil additives, *Adv. Colloid Interface Sci.* 123–126 (2006) 425–431.
43. A Shankara, P. L Menezes, K R Y Simha , S. V Kailas, Study of solid lubrication with MoS_2 coating in the presence of additives using reciprocating ball-on-flat scratch tester. *Sadhana* 33 (2008) 207–220
44. A.F. Wells. *Structural Inorganic Chemistry*, Oxford University Press 2012.
45. O. P. Parenago, G. N. Kuzmina, Formation and properties of the triboactive nanoparticles of molybdenum sulfides, *Petroleum chemistry* 50(2010) 319–324.
46. <http://www.tribology-abc.com/abc/solidlub.htm>

47. D. Duphil, S. Bastide, C.L.Clement, Chemical synthesis of molybdenum disulfide nanoparticles in an organic solution, *J. Mater. Chem.* 12 (2002) 2430–2432.
48. A. Yu. Suslov, V.N. Bakunin, G. N. Kuzmina, Surface-capped molybdenumsulfide nanoparticles- A novel type of lubricant additives, National tribology conference (2003) 254-257.
49. K. Du, W. Fu, R. Wei, H. Yang, S. Liu, S. Yu, G. Zou, Synthesis of inorganic fullerene-like MoS₂ nanoparticles by a facile method, *Mater.Lett.* 61(2007) 4887–4889.
50. Y. Feldman, E. Wasserman, D.J. Srolovitz, R. Tenne, High-Rate, gas-phase growth of MoS₂ nested inorganic fullerenes and nanotubes, *Science* 267 (1995) 222-225.
51. H.B. Yang, S.K. Liu, J.X. Li, M.H. Li, G. Peng, G.T. Zou, Synthesis of inorganic fullerene-like WS₂ nanoparticles and their lubricating performance, *Nanotechnology* 17(2006) 1512-1519.
52. M. Chhowalla, G.A.J. Amaratunga, Thin films of fullerene-like MoS₂ nanoparticles with ultra-low friction and wear, *Nature* 407 (2000) 164-167.
53. R. Sen, A. Govindaraj, K. Suennaga, S. Suzuki, H. Kataura, S. Iijima, Y. Achiba, Encapsulated and hollow closed-cage structure of WS₂ and MoS₂ prepared by laser ablation at 450-1050°C, *Chem. Phys. Lett.* 340 (2000) 242-248.
54. M. Nath, A. Govindaraj, C.N.R. Rao, Simple synthesis of MoS₂ and WS₂ nanotubes, *Adv. Mater.* 13 (2001) 283-286.
55. X.Y. Chen, X. Wang, Z.H. Wang, W.C. Yu, Y.T. Qian, Direct sulfidation of high-quality binary sulphides (WS₂, MoS₂ and V₅S₈) from the respective oxides, *Mater. Chem. Phys.* 87 (2004) 327-331.
56. Y. Xiong, Y. Xie, Z.Q. Li, X.X. Li, R. Zhang, Micelle-assisted fabrication of necklace-shaped assembly of inorganic fullerene-like molybdenum disulfide nanospheres, *Chem. Phys. Lett.* 382 (2003) 180-185.
57. X.L. Li, Y.D. Li, MoS₂ nanostructures: synthesis and electrochemical Mg²⁺ intercalation, *J. Phys. Chem., B* 108 (2004) 13893-13900.
58. C. Altavilla, M. Sarno, and P. Ciambelli, A Novel Wet Chemistry Approach for the Synthesis of Hybrid 2D Free-Floating Single or Multilayer Nanosheets of MS₂@oleylamine (M=Mo, W), *Chem. Mater.* 23(2011) 3879–3885.

59. X. Feng, Q. Tang, J. Zhou, J. Fang, P. Ding, L. Sun, and L. Shi, Novel mixed-solvothermal synthesis of MoS₂ nanosheets with controllable morphologies, *Cryst. Res. Technol.* 48 (2013), 363–368.
60. A. O'Neill, U. Khan, J. N Coleman, Preparation of High Concentration Dispersions of Exfoliated MoS₂ with Increased Flake Size, *Chem. Mater.* 24 (2012), 2414–2421.
61. Z. Wu, D. Wang, A. Sun, Preparation of MoS₂ by a novel mechanochemical method, *J. Alloys Compd.* 492 (2010) L5–L7.
62. C. Jun, L. Suolong, G. Feng, X. Qiang, K. Tanaka, Low-temperature catalytic preparation of multi-wall MoS₂ nanotubes, *Sci. China, Ser. B* 46 (2003), 191–195.
63. A. Verma, W. Jiang, H. H. A. Safe, W. D. Brown, A. P. Malshe, Tribological behavior of deagglomerated active inorganic nanoparticles for advanced lubrication, *Tribology Transactions* 51(2008) 673–678.
64. Z. Wu, D. Wang, Y. Wang and A. Sun, Preparation and tribological properties of MoS₂ nanosheets, *Adv. Eng. Mater.* 12(2010), 534–538.
65. P. Kalita, K. Carlson, B. Shen, A. Shih, A. P. Malshe, Exploring performance of novel MoS₂ nanoparticles for MQL grinding through tribological measurements, *Transactions of NAMRI/SME*, 36 (2008) 357–364.
66. R. Rosentsveig, A. Gorodnev, N. Feuerstein, H. Friedman, A. Zak , N. Fleischer, J. Tannous, F. Dassenoy, R. Tenne, Fullerene-like MoS₂ nanoparticles and their tribological behavior, *Tribol Lett* 36 (2009), 175–182.
67. J. Tannous, F. Dassenoy, I. Lahouij, T. L. Mogne, B. Vacher, A. Bruhacs, W. Tremel, Understanding the tribochemical mechanisms of IF-MoS₂ nanoparticles under boundary lubrication, *Tribol Lett* 41 (2011), 55–64
68. Z. Xiaodong, F. Xun, S. Huaqiang, H. Zhengshui, Lubricating properties of Cyanex 302-modified MoS₂ microspheres in base oil 500SN, *Lubr. Sci.* 19(2007), 71–79.
69. X. Zhou, H. Shi, X. Fu, D. Wu , Z. Hu, Tribological properties of Cyanex 301-modified MoS₂ nano-sized hollow spheres in liquid paraffin, *Industrial lubrication and tribology* 60 (2008) 147–152.
70. K.H. Hu, X. G. Hu, Y.F. Xu, F. Huang, J. S. Liu, The effect of morphology on the tribological properties of MoS₂ in liquid paraffin, *Tribol Lett* 40 (2010), 155–165.
71. H. Sliney, Solid Lubricants, NASA Technical Memorandum 102803, April 1991.

72. D.A. Lelonis, Boron Nitride-A Review, Ceramic Technology International, 1994, A Sterling Publication.
73. C. Sun, C. Guo, X. Maa, L. Xu , Y. Qian , A facile route to prepare boron nitride hollow particles at 450°C, J. Cryst. Growth, 311 (2009) 3682–3686.
74. H. E. Camurlu, Effect of Na₂CO₃ on hexagonal boron nitride prepared from urea and boric acid, Ceram. Int. 37 (2011) 1993–1999.
75. J. E. Nocua, F. Piazza, B. R. Weiner, G. Morell , High-yield synthesis of stoichiometric boron nitride nanostructures, Journal of nanomaterials, 2009 (2009) 1-6.
76. A. Nag, K. Raidongia, K. P. S. S. Hembram, R. Datta, U. V. Waghmare, C. N. R. Rao, Graphene Analogues of BN: novel synthesis and properties, ACS Nano, 4 (2010) 1539–1544.
77. X. Shi, S. Wang, H. Yang, X. Duan, X. Dong, Fabrication and characterization of hexagonal boron nitride powder by spray drying and calcining– nitriding technology, J. Solid State Chem. 181 (2008) 2274– 2278.
78. L. Lin , Y. Zheng, Y. Zheng, K. Wei, Facile synthesis of hexagonal boron nitride fibers and flowers, Mater. Lett.61 (2007) 1735–1737.
79. Z. Zhao, Z. Yang, Y. Wen, Y. Wang, Facile synthesis and characterization of hexagonal boron nitride nanoplates by two-step route, J. Am. Ceram. Soc. 94 (2011) 4496–4501.
80. Y. Gu, M. Zheng, Y. Liu, Z. Xu, Low-temperature synthesis and growth of hexagonal boron-nitride in a lithium bromide melt, J. Am. Ceram. Soc. 90 (2007) 1589–1591.
81. J. Duan, R. Xue, Y. Xu, C. Sun, Low temperature synthesis of h-BN nanoflakes, Mater. Lett.62 (2008) 3355–3357.
82. B. Matovic, B. Babic, A. Devecerski, M. Radovic, A. Minovic , M. Miljkovic , S. Boskovic, New synthetic route for nanocrystalline boron nitride powder, Mater. Lett.65 (2011) 307–309.
83. W. S. Zhang, J. G. Zheng, W. F. Li, D. Y. Geng, Z. D. Zhang, Synthesize and characterization of hollow boron-nitride nanocages, Journal of Nanomaterials 2009 (2009) 1- 4.
84. L. Shi, Y. Gu, L. Chen, Y. Qian, Z. Yang, J. Ma, Synthesis and morphology control of nanocrystalline boron nitride, J. Solid State Chem. 177 (2004) 721–724.

85. Z. M. Tao, L. Y. Liang, G. Y. Le, X. ZiLin, Synthesis and characterization of boron nitride sponges as a novel support for metal nanoparticles, *Sci China Ser B-Chem* 51 (2008) 205-210.
86. Jun-Qing Hu, Qing-Yi Lu, Kai-Bin Tang, Shu-Hong Yu, Yi-Tai Qian, Gui-En Zhou, Xian-Ming Liu, Jian-Xin Wu, Synthesis and characterization of nanocrystalline boron nitride, *J. Solid State Chem.* 148(1999) 325-328.
87. Li Hou, F. Gao, G. Sun, H. Gou, M. Tian, Synthesis of high-purity boron nitride nanocrystal at low temperatures, *Crystal Growth & Design*, 7(2007) 535-540.
88. T. I Taniguchi, K. Kimoto, M. Tansho, S. Horiuchi, S. Yamaoka, Phase transformation of amorphous boron nitride under high pressure, *Chem. Mater.* 15(2003)2744-2751.
89. J. Yu, L. Qin, Y. Hao, S. Kuang, X. Bai, Yat-ming Chong, W. Zhang, E. Wang, Vertically aligned boron nitride nanosheets: chemical vapour synthesis, ultraviolet light emission, and superhydrophobicity, *ACS nano*. 4(2010) 414-422.
90. Y. Lin, T.V. Williams, J.W. Connell, Soluble, exfoliated hexagonal boron nitride nanosheets, *J. Phys. Chem. Lett.* 1(2010) 277-283.
91. Y. Wang, Z. Shi, J. Yin, Boron nitride nanosheets large scale exfoliation in methanesulfonic acid and their composites with polybenzimidazole, *J. Mater. Chem.* 21 (2011) 11371-11377.
92. M. Du, Y. Wu, X. Hao, A facile chemical exfoliation method to obtain large size boron nitride nanosheets, *Cryst Eng Comm.* 15(2013) 1782-1786.
93. X. Li, X. Hao, M. Zhao, Y. Wu, J. Yang, Y. Tian, G. Qian, Exfoliation of hexagonal boron nitride by molten hydroxides, *Adv. Mater.* 25(2013) 2200-2204.
94. K.S. Novoselov, A.K. Geim, S.V. Morozov, D. Jiang, Y. Zhang, S.V. Dubonos, I.V. Grigorieva, A.A. Firsov, Electric field effect in atomically thin carbon films, *Science* 306 (2004) 666-669.
95. Y. M. Chang, H. Kim, J. H. Lee, Yong-Won Song, Multilayered graphene efficiently formed by mechanical exfoliation, *Appl. Phys. Lett.* 97 (2010) 2111021-2111023.
96. C. Lee, Q. Li, W. Kalb, X.Z. Liu, H. Berger, R. W. Carpick, J. Hone, Frictional characteristics of atomically thin sheets, *Science* 328 (2010) 76-80.
97. B. Radisavljevic, A. Radenovic, J. Brivio, V. Giacometti, A. Kis, Single layer MoS₂ transistors, *Nature nanotechnology* 6 (2011) 147-150.

98. K. S. Novoselov, D. Jiang, F. Schedin, T. J. Booth, V. V. Khotkevich, S. V. Morozov, A. K. Geim, Two-dimensional atomic crystals, *PNAS* 102 (2005) 10451-10453.
99. D. Pacile, J. C. Meyer, C. O. Girit, A. Zettl, The two-dimensional phase of boron nitride : few-atomic-layer sheets and suspended membranes, *Appl. Phys. Lett.* 92 (2008), 1331071-1331073.
100. Y. Chen, J. F. Gerald, L. T. Chadderton, L. Chaffron, Nanoporous carbon produced by ball milling, *Appl. Phys. Lett.* 74(1999) 2782-2784.
101. T. Makarova, M. Riccò, D. Pontiroli, M. Mazzani, M. Belli, A. Goffredi, Ageing effects in nanographite monitored by raman spectroscopy, *Physica status solidi (b)* 245 (2008) 2082-2085.
102. L. H. Li, Y. Chen, G. Behan, H. Zhang, M. Petracic, A. M. Glushenkov, Large-scale mechanical peeling of boron nitride nanosheets by low-energy ball milling, *J. Mater. Chem.* 21(2011) 11862-11866.
103. Y. Yao, Z. Lin, Z. Li, X. Song, K-S Moon, C-P Wong, Large-scale production of two-dimensional nanosheets, *J. Mater. Chem.* 22(2012) 13494.
104. Y. Cao, L. Du, C. Huang, W. Liu, W. Zhang, Wear behavior of sintered hexagonal boron nitride under atmosphere and water vapor ambiances, *Appl. Surf. Sci.* 257 (2011) 10195– 10200.
105. Z. Pawlak, T. Kaldonski, R. Pai, E. Bayraktar, A. Oloyede, A comparative study on the tribological behaviour of hexagonal boron nitride (h-BN) as lubricating micro-particles—An additive in porous sliding bearings for a car clutch, *Wear* 267 (2009) 1198–1202.
106. Z. Pawlak, T. Kaldonski, M. Lisewski, W. Urbaniak, A. Oloyede, The effect of hexagonal boron nitride additive on the effectiveness of grease-based lubrication of a steel surface, *Industrial lubrication and tribology* 64 (2012) 84-89.
107. Y. Kimura, T. Wakabayashi, K. Okada, T. Wada, H. Nishikawa, Boron nitride as a lubricant additive, *Wear* 232 (1999) 199-206.
108. J. T. Tijerina, T. N. Narayanan, G. Gao, M. Rohde, D. A. Tsentalovich, M. Pasquali, P. M. Ajayan, Electrically insulating thermal nano-oils using 2D fillers, *ACS nano* 6 (2012) 1214-1220.

109. J.Taha-Tijerina, L.Pena-Paras, T.N. Narayanan, L.Garza, C.Lapray, J.Gonzalez, E.Palacios, D. Molina, A. Garcia, D.Maldonado, P.M. Ajayan, Multifunctional nanofluids with 2D nanosheets for thermal and Tribological management, *Wear* 302(2013) 1241-1248.
110. O.N Celik, N.Ay, Y.Goncu, Effect of nano hexagonal boron nitride lubricant additives on the friction and wear properties of Aisi 4140 steel, *Particulate Science and Technology: An International Journal* 31(2013) 501-506.
111. Chapter 2 High-Energy Milling P. Bal'az, *Mechanochemistry in Nanoscience and Minerals Engineering*, Springer-Verlag Berlin Heidelberg 2008.
112. C. Suryanarayana, *Mechanical alloying and milling*, Marcel Dekker, New York, 2004.
113. M. Sopicka-Lizer, *High-energy Ball Milling: Mechanochemical Processing of Nanopowders*, Woodhead Publishing Limited, 2010.
114. L.G. Austin, R.R. Klimpel, P. T. Luckie, *Process Engineering of Size Reduction: Ball Milling*, Society of Mining Engineers of the American Institute of Mining, Metallurgical, and Petroleum Engineers, 1984.
115. R. Pecora, *Dynamic Light Scattering: Applications of Photon Correlation Spectroscopy*, Springer, 31-May-1985
116. B. D. Cullity, S. R. Stock, *Elements of X-ray Diffraction*, Prentice Hall, Upper Saddle River, NJ 07458, 3rd ed. 2001.
117. N. F. M. Henry, J. Lipsons, W. A. Wooster, *The interpretation of X-ray diffraction photographs*, Macmillan and Co. Ltd. London, 1951.
118. T. G. Rochow, P. A. Tucker, *Introduction to microscopy by means of light, electrons, X-rays or Acoustics*, Plenum Publishing Corporation, New York, 1994.
119. D. B. Williams, *Transmission Electron Microscopy*, A textbook for Material Science, Plenum Press. New York and London. 1996.
120. (a) T. E. Everheart, T. L. Hayes, The scanning electron microscope, *Sci. Am.* 1972, 226, 55. (b) Reimschuessel, Scanning Electron Microscope, *J. Chem. Educ.* 1972, 49, A 413.
121. C. W. Oatley, *Scanning Electron Microscope: The Instrument*, Cambridge, 1972.
122. H. M. Joshi, P. Shirude, V. Bansal, K. N. Ganesh, M. Sastry, Isothermal titration calorimetric studies on the binding of amino acids to gold nanoparticle. *J. Phys.Chem.B*2004, 108, 11535.

123. O. Glatter, O. Kratky, Small angle scattering, Academic Press, 1982.
124. Chapter-1 contact angle and wetting properties, Surface science techniques, Springer Series in Surface Sciences 51, 2013.
125. C.N Banwell, E.M McCash, Fundamentals of Molecular & Spectroscopy, McGraw-Hill International (UK) Limited, 4th ed. 1994.
126. B. C. Lippens, J. H. de Boer, J. Catal. 4 (1965) 319.
127. E. P. Barret, L. G. Joyner, P. H. Halenda, J. Amer. Chem. Soc. 73 (1951) 373.
128. J.M. Martin, N. Ohmae, Nanolubricants, John Wiley & Sons, Ltd. 2008.
129. Y.Wang, W. Eli, Y. Liu, L. Long, Synthesis of Environmentally Friendly Calcium Oleate Detergent, Ind. Eng. Chem. Res. 47(2008) 8561–8565.
130. M.Hea, E.Forssberga, Y.Wangab, Y. Han, Ultrasonication-assisted synthesis of calcium carbonate nanoparticles, Chem. Eng. Comm.192 (2005) 1468–1481.
131. T. Ahsan, D. A. Taylor, The Influence of Surface Energetics of Calcium Carbonate Minerals on Mineral-Polymer Interaction in Polyolefin Composites, J. Adhesion.67 (1998) 69-79.
132. S.K. Hait, B.G. Polke, S. Venugopalan, B.R. Gandhe, A.S. Rao, Environmental Scanning Electron Microscopic Study Of Electron Impacted High Explosive, Microsc Microanal 11(Suppl 2), (2005) 2054-2055.
133. Deepika, S.K. Hait, J. Christopher, Y. Chen, P. Hodgson, D.K. Tuli, Preparation and evaluation of hydrophobically modified core shell calcium carbonate structure by different capping agents, Powder Technology 235 (2013) 581–589.
134. Y. S. Zheng, Y. Heb, Y. Qing, C. Hu, Q. Mo, Preparation of superhydrophobic coating using modified CaCO₃, Applied Surface Science 265 (2013) 532– 536.
135. Z. Yang, Y. Tang, J. Zhang, Surface Modification Of CaCO₃ Nanoparticles with silane coupling agent for improvement of the interfacial compatibility with styrene-butadiene rubber (SBR) latex, Chalcogenide Letters 10 (2013) 131 – 141.
136. R. G. Larson, The structure and rheology of complex fluids, Oxford University Press, USA (1999).
137. T.M. Shea, A.J. Stipanovic, Solution phase reactions of organomolybdenum friction modifier additives for energy conserving engine oils, Tribo. Lett. 12 (2202), 13-22.

138. M. Pykal, K. Safarova, K. M. Siskova, P. Jurecka, A. B. Bourlinos, R. Zboril, and M. Otyepka, Lipid Enhanced Exfoliation for Production of Graphene Nanosheets, *J. Phys. Chem. C*, 117(2013)11800–11803.
139. B.D. Mittal, E. Sayanna, K.P. Naithani, M.M. Rai, and A.K. Bhatnagar, Effect of Metallic Thiophosphates on Dropping Point and Penetration Properties of Some Greases, *Lubrication Science*, 10(1998) 171-176.
140. V. Stengl, J. Henych, Strongly luminescent monolayered MoS₂ prepared by effective ultrasound exfoliation, *Nanoscale*, 5(2013) 3387-3394.
141. M. Lotya, A. Rakovich, J. F Donegan, J. N Coleman, Measuring the lateral size of liquid-exfoliated nanosheets with dynamic light scattering, *Nanotechnology* 24 (2013) 265703.
142. Y. Feldman, E. Wasserman, D.J. Srolovitz, R. Tenne, High-Rate, gas-phase growth of MoS₂ nested inorganic fullerenes and nanotubes, *Science* 267 (1995) 222.
143. V. N. Bakunin, M. Kasrai, G. N Kuzmina, G. M. Bancroft, O.P. Parenago, Influence of temperature and ZDDP concentration on tribochemistry of surface-capped molybdenum sulphide nanoparticles studied by XANES spectroscopy, *Tribol. Lett.* 26(2007) 33-44.
144. G. L. Frey, R. Tenne, Raman and resonance Raman investigation of MoS₂ nanoparticles, *Physical Review B* 60(1999) 2883-2892.
145. Y. Zhan, Z. Liu, S. Najmaei, P.M. Ajayan, J. Lou Large-Area Vapor-Phase Growth and Characterization of MoS₂ Atomic Layers on a SiO₂ Substrate, *Small* (2012)1-6.
146. J.M. Chen, C.S. Wang, Second Order Raman Spectrum of MoS₂, *Solid State Communications*, 14(1974)857-860.
147. Y. Shi, C. Hamsen, X. Jia, K. K. Kim, A. Reina, M. Hofmann, A. L. Hsu, K. Zhang, H. Li, Z-Y. Juang, Synthesis of Few-Layer Hexagonal Boron Nitride Thin Film by Chemical Vapor Deposition, *nano letters* 10 (2010), 4134-4139.
148. M. Turkoglu, I. Sahin, T. San, Evaluation of Hexagonal Boron Nitride as a New Tablet Lubricant. *Pharm Dev Technol.* 10 (2005), 381-8.
149. L. Song, L. Ci, H. Lu, P. B. Sorokin, C. Jin, J. Ni, A. G. Kvashnin, D. G. Kvashnin, J. Lou, B. I. Yakobson, Large Scale Growth and Characterization of Atomic Hexagonal Boron Nitride Layers, *nano letters* 10 (2010) 3209-3215.

150. J.Yu, L. Qin, Y. Hao, S. Kuang, X. Bai, Y-M. Chong, W. Zhang, E. Wang, Vertically Aligned Boron Nitride Nanosheets: Chemical Vapor Synthesis, Ultraviolet Light Emission, and Superhydrophobicity, *ACS Nano* 4(2010) 414-422.
151. W. Auwärter, H.U. Suter, H. Sachdev, T. Greber, Synthesis of One Monolayer of Hexagonal Boron Nitride on Ni(111) from B-Trichloroborazine (ClBNH)₃, *Chemistry of Materials* 16(2003) 343-345.
152. M. Xu, D. Fujita, H. Chen, N. Hanagata, Formation of monolayer and few-layer hexagonal boron nitride nanosheets via surface segregation, *Nanoscale* 3(2011) 2854-2858.
153. D. Pacilé, J. C. Meyer, Ç. Ö. Girit, A. Zettl, The two-dimensional phase of boron nitride: Few-atomic-layer sheets and suspended membranes. *Applied Physics Letters* 92 (2008) 1331071-1331073.
154. A. S. Nazarov, V. N. Demin, E. D. Grayfer, A. I. Bulavchenko, A. T. Arymbaeva, H-J. Shin, J-Y Choi, V. E. Fedorov, Functionalization and Dispersion of Hexagonal Boron Nitride (h-BN) Nanosheets Treated with Inorganic Reagents, *Chem. Asian J.* 7 (2012) 554-560.
155. T. Xing, L. H. Li, L. Hou, X. Hu, S. Zhou, R. Peter, M. Petracic, Y. Chen, Disorder in ball-milled graphite revealed by Raman spectroscopy, *Carbon* 57 (2013) 515-519.
156. K. Lee, Y. Hwang, S. Cheong, Y. Choi, L. Kwon, J. Lee, S. H. Kim, Understanding the Role of Nanoparticles in Nano-oil Lubrication, *Tribol. Lett.* 35 (2009), 127-131.